THE UNIVERSITY OF CHICAGO

DRY ATMOSPHERIC CIRCULATIONS OF ROCKY EXOPLANETS

A DISSERTATION SUBMITTED TO
THE FACULTY OF THE DIVISION OF THE PHYSICAL SCIENCES
IN CANDIDACY FOR THE DEGREE OF
DOCTOR OF PHILOSOPHY

DEPARTMENT OF THE GEOPHYSICAL SCIENCES

BY
DANIEL DRAGOMIR BENEDIKT KOLL

CHICAGO, ILLINOIS
DECEMBER 2016

You can grow ideas

in the garden of your mind.

— Mister Rogers

TABLE OF CONTENTS

LIST OF FIGURES

LIST OF TABLES

ACKNOWLEDGMENTS

Above all, thank you to my adviser, mentor, and friend Dorian Abbot, whose enthusiasm is a constant source of inspiration. You taught me how to be a scientist.

Further thanks to my committee members and teachers Ray Pierrehumbert, Malte Jansen, Liz Moyer, Fred Ciesla, Wendy Zhang, Jacob Bean, and Dan Fabrycky.

Another thanks to my co-students from whom I learned so much, especially Jonah Bloch-Johnson and Feng Ding.

Final thanks to my family and everybody in Haymarket for all their support and for making these years fun.

ABSTRACT

Rocky planets orbiting nearby cool stars are extremely common, and next-generation space telescopes will allow us to begin studying them within the next few years. The extent to which we can make sense of these planets, let alone deduce whether any of them might host life, depends crucially on how well we can understand their atmospheres. This thesis develops a series of theoretical models for the atmospheric circulations of dry and tidally locked planets in particular, and of dry planets in general.

First, we motivate the detailed study of atmospheric dynamics for rocky exoplanets. We demonstrate that a tidally locked planet's thermal phase curve, which is set by the atmospheric redistribution of heat between the day- and the nightside, can be used to measure a planet's surface pressure and thus distinguish between planets with thick and thin atmospheres. Second, we develop a theory for the temperature structure and circulation strength of tidally locked planets. We show that the atmospheres of tidally locked planets act as large-scale heat engines, which allows us to predict their wind speeds and day-night temperature gradients. Our theory shows that rocky planets can exhibit large day-night temperature gradients at far bigger distances from their host star than can be explained by theories developed for hot Jupiters. Third, we extend our heat engine theory to atmospheres that are not tidally locked. We show that dry atmospheres primarily act to maintain a vertical, not a horizontal, temperature structure. We quantify this balance using entropy budgets and constrain the entropy production necessary for maintaining an atmosphere's vertical temperature structure, which in turn allows us to predict the strength of frictional dissipation and surface winds across a wide range of dry atmospheres.

CHAPTER 1

INTRODUCTION

Thanks to the exoplanet discoveries of the past decades we now know that the Milky Way is full of planets (Burke et al., 2015; Dressing & Charbonneau, 2015). Much information about these worlds can be gleaned from their mere existence, their sizes and masses, and their orbital configurations. To learn what these worlds are like, however, requires us to address their atmospheres.

Atmospheres are dynamical entities. They evolve, they produce winds and weather, they transport heat and drive chemistry, and they can be overcast or cloud-free. Observational astronomers have taken on the challenge of studying these entities and, over the past decade, have begun characterizing the wind speeds, three-dimensional temperature structure, and atmospheric compositions of hot and large gaseous planets (Knutson et al., 2007; Snellen et al., 2010; Stevenson et al., 2014; Kreidberg et al., 2015). The same researchers are now preparing the next generation of instruments that will allow them to perform similar measurements for nearby cool and small rocky exoplanets, in the hope of ultimately detecting bio-signatures on another world (Tinetti et al., 2012; Beichman et al., 2014; Dalcanton et al., 2015). A comparable endeavor is required from theoretical scientists to ensure that we will be able to make sense of these discoveries.

The goal of this thesis is to develop a theoretical foundation for understanding the atmospheric circulations that we will encounter on rocky extrasolar planets. Although such theories have been developed for Earth's atmosphere (Held & Hou, 1980; Schneider & Walker, 2006; Jansen & Ferrari, 2013), Earth is likely a misleading template for thinking about extrasolar planets. First, the rocky exoplanets most accessible to near-future observations lie on orbits of a few tens of days or less around a host star that is smaller than the Sun. The tidal interaction between these planets and their host star is substantially stronger than between Earth and the Sun, and acts to damp the planets' rotation (Kasting et al., 1993). This means many exoplanets that have recently been discovered, such as GJ 1132b and Proxima

Centauri b, are likely tidally locked and possess one permanent dayside and one permanent nightside. Second, water vapor and its effects play a major role in Earth's atmosphere, but many rocky exoplanets might be devoid of water due to the stochastic nature of volatile delivery during planet formation (Raymond et al., 2004) as well as the photodissociation of water and its loss to space, similar to how Venus is thought to have lost its water (Ingersoll, 1969; Wordsworth & Pierrehumbert, 2013; Barnes et al., 2016; Ribas et al., 2016). Moreover, theories developed for Earth's atmosphere first had to address the dynamics of dry atmosphere to provide a starting point for understanding the additional effects of moisture (e.g., O'Gorman, 2010). In this thesis we pursue a similar logic and focus on dry atmospheres.

In Chapter 2 we motivate the detailed study of atmospheric dynamics for tidally locked planets. We present a method for inferring a planet's surface pressure by considering how its observable thermal phase curve signature reflects its underlying atmospheric dynamics. This is important because the main observational technique to date, transit spectroscopy, probes only the upper-most layers of a planet's atmosphere and cannot distinguish between a planet with a moderately thin atmosphere, like Earth, and a planet with a thick atmosphere, like Venus.

In Chapter 3 we present a theory for the temperature structure and wind speeds of tidally locked planets. We show that the atmospheres of tidally locked planets resemble heat engines, which are driven by the temperature difference between the hot dayside and the cold upper atmosphere and which act to balance friction on the turbulent dayside. We derive a thermodynamic speed limit for the circulations of these planets, and use it to constrain their day-night temperature gradient as well as vertical temperature structure. Our theory explains why the atmospheres of rocky planets develop large day-night temperature gradients at a substantially smaller threshold than that predicted by theories developed for hot Jupiters. Our results are important because atmospheres of tidally locked planets had previously been studied with a range of complex numerical models, but without understanding the behavior of these models it is impossible to distinguish between physically robust behavior and potential model particularities. We capture the large-scale features of tidally locked atmospheres using relatively simple expressions, lending confidence to our ability to interpret actual observations of rocky exoplanets. Moreover, numerical models used in isolation produce numbers, not understanding. An interplay between complex models and simple theory is necessary to ensure that we can draw meaningful insight from future observations, and in the process also gain a richer understanding of Earth. Finally, analytical theories allow us to consider a much wider range of scenarios than numerical models and to make comparisons that cannot be obtained otherwise. In particular, the observed day-night temperature gradients of hot Jupiters tend to be small for planetary equilibrium temperatures below about 2000 K, which translates into orbital periods of a few days or less. In contrast, our theory makes the testable prediction that rocky planets can exhibit large and observable day-night temperature gradients at much lower equilibrium temperatures and even inside their host star's habitable zone.

In Chapter 4 we use entropy budgets to extend our heat engine theory from Chapter 3 to other dry atmospheres, such as present-day Mars or Earth's atmosphere during Snowball Earth episodes. In doing so, we show that dry atmospheres primarily produce entropy to maintain their vertical temperature structure. We then constrain the entropy production necessary for doing so, which allows us to predict the frictional dissipation and mean surface winds in dry atmospheres. This is important because entropy budgets have mainly been considered in the context of predicting the behavior of moist convection in Earth's tropics, whereas our result provides a proof-of-principle that entropy budgets can be used to gain predictive insight into large-scale circulations. Furthermore, in bridging the gap between tidally locked and rapidly rotating atmospheres, our results demonstrate how the study of exoplanet atmospheres can help us better contextualize our own planet.

Finally, we present a summary of our results and an outlook for future observations in Chapter 5.

CHAPTER 2

DECIPHERING THERMAL PHASE CURVES OF TIDALLY LOCKED EXOPLANETS

Next-generation space telescopes will allow us to characterize terrestrial exoplanets. To do so effectively it will be crucial to make use of all available data. We investigate which atmospheric properties can, and cannot, be inferred from the broadband thermal phase curve of a dry and tidally locked terrestrial planet. First, we use dimensional analysis to show that phase curves are controlled by six nondimensional parameters. Second, we use an idealized general circulation model (GCM) to explore the relative sensitivity of phase curves to these parameters. We find that the feature of phase curves most sensitive to atmospheric parameters is the peak-to-trough amplitude. Moreover, except for hot and rapidly rotating planets, the phase amplitude is primarily sensitive to only two nondimensional parameters: 1) the ratio of dynamical to radiative timescales, and 2) the longwave optical depth at the surface. As an application of this technique, we show how phase curve measurements can be combined with transit or emission spectroscopy to yield a new constraint for the surface pressure and atmospheric mass of terrestrial planets. We estimate that a single broadband phase curve, measured over half an orbit with the *James Webb Space Telescope*, could meaningfully constrain the atmospheric mass of a nearby super-Earth. Such constraints will be important for studying the atmospheric evolution of terrestrial exoplanets as well as characterizing the surface conditions on potentially habitable planets.

2.1 Introduction

Data from the Kepler telescope indicate that $\sim$ 50-100% of nearby cool stars host a rocky planet (Dressing & Charbonneau, 2013; Morton & Swift, 2014). If we were able to characterize even a fraction of these planets we could vastly expand our understanding of processes fundamental for terrestrial planets, including planet formation, atmospheric escape, photochemistry, and atmospheric dynamics. The observational best-case scenario is a transiting planet, whose orbit we happen to view edge-on, so that the planet periodically passes in front of and behind its star. Broadly speaking, to characterize such a planet we would want to determine its atmospheric composition, temperature structure, and atmospheric mass[1]. The composition reflects how the planet formed, how its atmosphere subsequently evolved (e.g., via degassing from the interior or atmospheric escape), and the chemical state of its atmosphere. The temperature structure indicates the dynamical regime of the atmosphere and, if retrievable down to the surface, whether the planet could be habitable. The atmospheric mass reflects the planet's atmospheric evolution and also determines its habitability (by controlling whether water can exist as a liquid).

The most mature techniques for characterizing transiting planets are transit spectroscopy, in which starlight is measured as it filters through a planet's atmosphere, and emission spectroscopy, in which a planet's thermal emission is measured just before the planet is occulted by its star. In theory, high-resolution transit and emission spectra both contain enough information to uniquely constrain atmospheric composition, temperature structure, atmospheric mass, and planetary mass (Madhusudhan & Seager, 2009; Benneke & Seager, 2012; Line et al., 2012; Lee et al., 2012; de Wit & Seager, 2013). In practice, it is difficult to comprehensively characterize even hot Jupiters with any single spectroscopic technique due to measurement error and observational degeneracies (e.g., Burrows, 2014; Hansen et al., 2014; Griffith, 2014).

It is therefore desirable to seek additional methods for characterizing terrestrial planets that complement high-resolution spectroscopy. One simple approach is to observe a planet's broadband thermal phase curve, which is the net infrared flux the planet emits as it orbits its star. Before the planet passes in front of its star we observe flux emitted from the planet's nightside, and just before the planet passes behind its star we observe flux from the planet's

---

[1] The mass of an atmospheric column with unit surface area is p_s/g, where p_s is the surface pressure and g is the surface gravity.

dayside. The resulting phase curve can then be used to infer five pieces of information: the planet's average thermal emission, the location of hot and cold spots and the flux emitted at the hot and cold spots (Cowan & Agol, 2008). This technique has already been applied to hot Jupiters. For example, Knutson et al. (2007) were able to infer equatorial superrotation on HD 189733b from the fact that its hot spot is shifted eastward of the substellar point, consistent with the theoretical prediction of Showman & Guillot (2002). It will be more challenging to measure thermal phase curves of smaller and cooler planets, but it should be possible to perform such measurements using next-generation instruments like the *James Webb Space Telescope* (*JWST*; Deming & Seager, 2009).

Although thermal phase curve measurements of terrestrial planets will soon be technically feasible, more work is needed to determine how they can be fully exploited. A natural starting point is to assume that planets accessible to near-future observations will be tidally locked (even though planets could also be trapped in higher-order spin resonances, see Section 2.5). For a tidally locked planet the phase curve depends largely on the atmospheric redistribution of energy between dayside and nightside. Many researchers have therefore proposed using phase curves to characterize tidally locked planets (Seager & Deming, 2009; Cowan & Agol, 2011; Selsis et al., 2011; Menou, 2012a; Yang et al., 2013; Mills & Abbot, 2013; Perez-Becker & Showman, 2013; Yang & Abbot, 2014; Kataria et al., 2014). At the same time, these results have also shown that phase curves are sensitive to multiple atmospheric parameters, which makes them difficult to interpret. For example, a small phase curve amplitude is compatible with: 1) a massive atmosphere because thicker atmospheres transport heat more effectively (Selsis et al., 2011), 2) an atmosphere containing large amounts of H_2, which has a higher heat capacity than high mean-molecular-weight gases and therefore loses heat more slowly as air is advected to the nightside (Menou, 2012a), 3) relatively weaker absorption of shortwave radiation, so that stellar energy is deposited at higher pressures before being reemitted to space (Burrows et al., 2010; Heng et al., 2011a), and 4) a low magnetic drag in ionized atmospheres, which allows higher wind speeds and thus more efficient heat transport

(Rauscher & Menou, 2012).

In this paper we disentangle how different atmospheric parameters affect phase curves and show how the phase curve amplitude can be used to constrain atmospheric mass. We focus on the phase curve amplitude because we find that, for many terrestrial planets, hot/cold spot offsets will be small (see Section 2.3). We focus on atmospheric mass because it will be difficult to infer from either transit or emission spectroscopy, as can be seen from the following argument. Following Lecavelier des Etangs et al. (2008), the maximum pressure that can be probed in transit is $p_{max} = 0.56 \times g/\kappa_{min} \times \sqrt{H/(2\pi a)}$, where g is the acceleration of gravity, κ_{min} is the opacity per unit mass in the most transparent part of the spectrum, H is the scale height, and a is the planetary radius[2]. If we assume that Rayleigh scattering dominates the transit spectrum up to 0.75 μm and that this is the most transparent part of the spectrum, then, for an N_2 atmosphere, $\kappa_{min} \sim 2.59 \times 10^{-6}$ m^2 kg^{-1} (Table 5.2, Pierrehumbert, 2011b). For an Earth analog with $a = a_{\oplus}$, $g = 10$ m s^{-2} and $H = 8$ km, we find that $p_{max} = 0.3$ bar. In reality it would be even harder to probe an atmosphere this deeply in transit due to clouds and hazes (Fortney, 2005) or atmospheric refraction (Bétrémieux & Kaltenegger, 2014; Misra et al., 2014). Emission spectroscopy generally probes deeper into an atmosphere than transit spectroscopy. Atmospheric mass can then be constrained using the fact that pressure-broadening widens molecular absorption features at higher pressures. Nevertheless, pressure and molecular abundances are largely degenerate in their effect on emission spectra, which complicates the interpretation of emission spectra. For example, von Paris et al. (2013) estimate that emission spectroscopy of a cool Earth analog with a 1 bar atmosphere could place an upper bound on the surface pressure of about 5.6 bar. Obtaining the upper bound would require a low-resolution spectrum ($\lambda/\Delta\lambda = 20$) with a signal-to-noise ratio (SNR) of 10 (their Table 3). To estimate how much observation time this would require on *JWST*, we use the SNR maps in Belu et al. (2011) as a guideline. We estimate that, for a cool M-

---

[2] Compared to Section 4.1 in Lecavelier des Etangs et al. (2008), we additionally define $\kappa \equiv \sigma_0/\mu$, $R \equiv k/\mu$ and $H \equiv RT/g$.

dwarf at 5 pc, $SNR = 10$ at this spectral resolution would require $\sim$ 14 days of continuous monitoring[3]. This amounts to observing roughly every eclipse the planet makes during *JWST*'s five-year mission lifetime. The pressure-dependent formation of O_2 dimers offers another method for measuring atmospheric mass (Misra & Meadows, 2014). However, being able to detect the dimer spectral signature requires an atmosphere with O_2 concentrations similar to Earth's. The observation time necessary would again amount to $\sim$ 12 days of continuous observation, or almost all available transits over *JWST*'s mission lifetime. Such long-term and detailed observations could be feasible for high-priority observation targets, but even in those cases it would be desirable to have an independent and less time-consuming way of estimating the atmospheric mass.

In the following sections we first analyze the dynamical and radiative equations relevant for terrestrial planet atmospheres. We specifically consider atmospheres that are "dry" (i.e., condensation is negligible) and tidally locked. For such atmospheres we identify six nondimensional parameters that *could* influence phase curves (Section 2.2). Next, we use an idealized GCM to numerically test which of the six parameters phase curves actually are sensitive to (Section 2.3). Except for hot and rapidly rotating planets with optically thick atmospheres, we do not find significant hot/cold spot offsets. We therefore focus on how the phase curve amplitude can be used to constrain an atmosphere's properties. We find that, except for hot and rapidly rotating planets, the phase curve amplitude is mainly sensitive to two nondimensional parameters. We then show how the phase amplitude can be combined with information from transit or emission spectroscopy to constrain the atmospheric mass of a terrestrial planet (Section 2.4). We estimate that one measurement of a nearby super-Earth's phase amplitude with *JWST*, taken over half the planet's orbit, could constrain the atmospheric mass to within a factor of two.

---

[3] We assume $SNR = 10$ for the detection of CO_2 at 15 μm (Fig. 16b in Belu et al., 2011) is representative for the entire thermal range, which is optimistic (compare to their Fig. 15b). To allow comparison with Section 2.3, we additionally assume a 0.2 solar mass host star and rescale the required observation time for a target at 10 pc, which is $\sim 3\%$ of the *JWST* main mission or $\sim$ 1.8 months, to a target at 5 pc.

2.2 Methods

We adopt a basic, yet comprehensive, model for the phase curve of a terrestrial planet. We assume the planet is tidally locked and in a circular orbit. This regime is particularly relevant for planets orbiting smaller main-sequence stars, that is, K- and M-dwarfs. At minimum, the phase curve of such a planet is set by atmospheric fluid dynamics, radiative transfer, and surface-atmosphere exchange of energy and momentum. As is standard for planetary atmospheres, we model the atmospheric fluid dynamics using the primitive equations (Vallis, 2006). The primitive equations assume hydrostatic equilibrium and that horizontal length scales are much larger than vertical ones, both of which tend to be excellent approximations for large-scale motions. We focus on atmospheres cooler than 1000 K, for which magnetic effects should be negligible (Menou, 2012b). We use bulk aerodynamic formulae for the surface exchanges of energy and momentum. We model the radiative transfer as two-band (shortwave and longwave) gray radiation. We neglect scattering and assume that longwave and shortwave opacities increase linearly with pressure. The linear dependency approximates the effects of pressure broadening and continuum absorption in a well-mixed atmosphere (Robinson & Catling, 2014).

We assume that the thermodynamics are dry. This is a natural starting point for a theoretical investigation, but our results should apply to a wide range of actual atmospheres. First, we expect that many terrestrial planets will be dry because post-formation delivery of volatiles via planetesimals and comets is a stochastic process (Morbidelli et al., 2000). In addition, for planets hotter than Earth, volatiles can be lost via atmospheric escape (the so-called moist greenhouse; Kasting, 1988). On tidally locked planets, volatiles can also become cold-trapped on the nightside (Leconte et al., 2013; Menou, 2013). Moreover, the dry regime is a useful approximation even for atmospheres like Earth's with moderate amounts of a condensing substance (Schneider et al., 2006). We therefore expect that insight gained in the dry regime will carry over to the moist case. For example, if the atmospheric dynamics were insensitive to one parameter in the dry regime (e.g., surface friction), this suggests that moist atmospheres could be similarly insensitive. Finally, observations will be able to control for cases in which our analysis no longer applies. For example, condensation and cloud formation would lead to anomalously high bond albedos and could also reverse the expected day-night phase curve pattern (Yang et al., 2013).

The equations of our assumed model, shown in Appendix A, contain twelve dimensional parameters. The parameters are: stellar constant, L_*, planetary albedo, α, rotation rate, Ω, planetary radius, a, surface gravity, g, specific heat capacity, c_p, specific gas constant, R, shortwave and longwave opacities at some reference pressure, κ_{SW} and κ_{LW}, the Stefan-Boltzmann constant, σ_{SB}, surface pressure, p_s, and surface drag coefficient, C_D. For a single gas species the specific gas constant is $R \equiv k_B/(m_p M)$, where k_B is the Boltzmann constant, m_p is the mass of a proton, and M is the molecular weight of a gas molecule. For multiple species in a well-mixed dry atmosphere one can similarly assign bulk values of R and c_p (Caballero, 2014). The opacities κ_{SW} and κ_{LW} are defined at a reference pressure, p_0. The choice of p_0 is arbitrary and one could set it equal to p_s, so it does not provide an additional dimensional parameter. To better compare our choices of κ_{SW} and κ_{LW} with previous work, we keep p_0 and p_s distinct. We also note that L_*, α, and σ_{SB} are not independent. The product $L_*(1-\alpha)$ only appears in the stellar forcing term of the radiative equations, and σ_{SB} only appears in the radiative equations (Appendix A). We account for the degeneracy between L_*, α, and σ_{SB} by defining a characteristic temperature, $T_{eq} = [L_*(1-\alpha)/(4\sigma_{SB})]^{1/4}$, which is the equilibrium emission temperature of a spatially homogeneous planet. This reduces the number of dimensional parameters to ten.

Following Frierson (2005), we use the Buckingham-Pi theorem to express ten dimensional parameters measured in four different units (mass, length, time, and temperature) as only six nondimensional parameters (Buckingham, 1914). There is no unique choice for these nondimensional parameters; we form them using characteristic scales that we consider most appropriate for relatively slowly rotating tidally locked atmospheres. Our choice of scales nevertheless leads to nondimensional parameters that are well-known in the literature. As a characteristic velocity scale we choose the speed of gravity waves, $c \sim NH$, where N is the Brunt-Väisälä frequency and $H \equiv RT_{eq}/g$ is the scale height. Adjustment via gravity waves is key in setting the day-night temperature gradients, and hence phase curves, of relatively slowly rotating planets (Perez-Becker & Showman, 2013; Showman et al., 2013). The Brunt-Väisälä frequency is given by $N^2 = g/T(g/c_p + \mathrm{d}T/\mathrm{d}z)$. The lapse rate, $\mathrm{d}T/\mathrm{d}z$, is a priori unknown for any atmosphere. To place an upper bound on the velocity scale we assume an isothermal atmosphere, $\mathrm{d}T/\mathrm{d}z \sim 0$, so $c_{wave} = \sqrt{R/c_p} \times \sqrt{gH}$. This amounts to assuming that gravity waves are very fast (on the order of the speed of sound, $c_{sound} = \sqrt{\gamma_a RT_{eq}} = \sqrt{\gamma_a gH}$, where γ_a is the adiabatic index; cf. Heng & Kopparla, 2012). As a characteristic length scale we choose the planetary radius a. We note that another potential length scale is given by the equatorial Rossby deformation radius, $L_{Ro} = \sqrt{ac_{wave}/(2\Omega)}$, which is the maximum distance that equatorial waves can travel poleward under the influence of rotation. For slowly rotating planets the Rossby radius exceeds the planetary radius, $L_{Ro} > a$, and equatorial waves can propagate planet-wide. We estimate that our choice of a as the length scale is valid for planets with orbital period $\gtrsim \mathcal{O}(6)$ days[4]. From conservation of mass, we choose a vertical velocity scale $c_{wave} \times p_s/a$. The remaining scales and nondimensionalized equations are shown in Appendix A.

We arrive at the following six nondimensional parameters:

$$\left(\frac{R}{c_p}, \frac{2\Omega a}{c_{wave}}, \frac{a}{c_{wave}} \frac{g\sigma_{SB}T_{eq}^3}{c_p p_s}, \frac{\tau_{SW}}{\tau_{LW}}, \frac{\kappa_{LW} p_0}{g}\left[\frac{p_s}{p_0}\right]^2, \frac{C_D a g}{RT_{eq}}\right) \equiv$$
$$\left(\frac{R}{c_p}, \frac{a^2}{L_{Ro}^2}, \frac{t_{wave}}{t_{rad}}, \gamma, \tau_{LW}, C_D \frac{a}{H}\right).$$

The six parameters are related to physical processes as follows: the adiabatic coefficient R/c_p controls the lapse rate and is also identical to the ratio $2/(2+n)$, where n is the degrees of freedom of a gas (Pierrehumbert, 2011b). The nondimensional Rossby radius

---

[4] Assuming $R = R_{N_2}$, $c_p = c_{p,N_2}$, $T_{eq} = 300$K, and $a = a_\oplus$, $L_{Ro} > a$ for a planet beyond a 5.8-day orbital period.

a^2/L_{Ro}^2 governs the latitudinal extent over which equatorial waves can transport energy and momentum (Matsuno, 1966; Showman & Polvani, 2011; Leconte et al., 2013). We emphasize that instead of a^2/L_{Ro}^2 one could choose different scales and arrive at, for example, a Rossby number or a nondimensionalized Rhines scale (Showman et al., 2010, 2013). Which scale to choose depends on the processes under consideration, and our anticipation of wave adjustment processes naturally leads to a^2/L_{Ro}^2. Our results support our analysis, and we find that phase curves are largely insensitive to planetary rotation when $a^2/L_{Ro}^2 \lesssim 1$, that is, as long as waves propagate planet-wide (Section 2.3). The ratio t_{wave}/t_{rad} compares the time it takes for waves to redistribute energy across the planet, $t_{wave} \equiv a/c_{wave}$, to the atmosphere's radiative cooling time, $t_{rad} \equiv c_p p_s/(g\sigma_{SB}T_{eq}^3)$ (Showman et al., 2013; Perez-Becker & Showman, 2013). The atmospheric shortwave and longwave optical thicknesses at the surface are $\tau_{SW} \equiv \kappa_{SW} p_0/g \times (p_s/p_0)^2$ and $\tau_{LW} \equiv \kappa_{LW} p_0/g \times (p_s/p_0)^2$, and their ratio is γ. We note that the precise forms of τ_{SW} and τ_{LW} depend on details such as pressure broadening and scattering (e.g., Pierrehumbert, 2011b; Heng et al., 2014). Our definition of γ is equal to the more commonly used ratio of shortwave to longwave opacities (e.g., Guillot, 2010) when shortwave and longwave opacities have the same pressure dependency. The influence of surface friction and surface heating on the atmosphere is governed by $C_D a/H$.

Two atmospheres governed by the equations that we assume are guaranteed to be dynamically similar (identical dynamics in statistical equilibrium) if their six nondimensional parameters are identical (also see Section 2.5). We note that only the nondimensionalized dynamics will be similar; the physical values of, for example, temperature gradients or wind speeds could be quite different. We also note that dynamical similarity does not depend on how we nondimensionalize the equations, that is, our particular choice of characteristic scales and nondimensional parameters. Nondimensionalization therefore allows us to identify atmospheres that one might consider distinct based on their dimensional parameters, but that turn out to be dynamically similar.

We test this idea in an idealized GCM. The model is based on the GFDL Flexible Model

System (FMS; Held & Suarez, 1994) and was subsequently modified by Frierson et al. (2006) and Merlis & Schneider (2010). This model has already been used to simulate the atmospheres of Earth (Frierson et al., 2006), Jupiter (Liu & Schneider, 2011), hot Jupiters (Heng et al., 2011a), tidally locked terrestrial planets (Merlis & Schneider, 2010; Mills & Abbot, 2013), and non-synchronously rotating terrestrial planets (Kaspi & Showman, 2015). For our simulations, we remove moisture and replace the model's convective parametrization with an instantaneous dry convection scheme (Manabe et al., 1965). We run all simulations for at least 1000 days with a spatial resolution of either $64 \times 128 \times 30$ or $48 \times 96 \times 20$ grid points (latitude×longitude×vertical, corresponding to T42 or T31 spectral resolution). We use model time-steps between 30 and 1200 seconds. We vary the time-step because hot atmospheres require smaller time-steps for numerical stability, whereas colder atmospheres can be integrated using longer time-steps but also take longer to reach equilibrium. We expect this behavior, given that $c_{wave} \propto \sqrt{T}$, so that hotter atmospheres are more likely to violate the Courant-Friedrichs-Lewy criterion. We consider a simulation equilibrated once the global-averaged radiative imbalance between incoming stellar and outgoing longwave radiation has fallen below at least 1% of the incoming stellar radiation. We note that the GCM simulates additional higher-order physics, and therefore contains additional parameters, which we did not include in the derivation of the six nondimensional parameters. In particular, the model contains a full Monin-Obukhov surface boundary layer scheme which self-consistently computes the depth of the boundary layer, diffusion of surface fluxes, and surface drag. This means the drag coefficient, C_D, is computed by the model instead of being a fixed parameter[5]. For example, for a neutrally stratified boundary layer $C_D = (k_{vk}/\log[z/z_0])^2$, where k_{vk} is the von Karman constant, z is the height of the lowest model layer and z_0 is the roughness length. Because z and z_0 only enter into this equation logarithmically we modify C_D by adjusting k_{vk}. Similarly, the GCM requires additional parameters for its numerical

---

[5] For the same reason the values for $C_D a/H$ shown in our results are only approximate. We estimate $C_D a/H$ assuming neutral stratification and $z = 10$m.

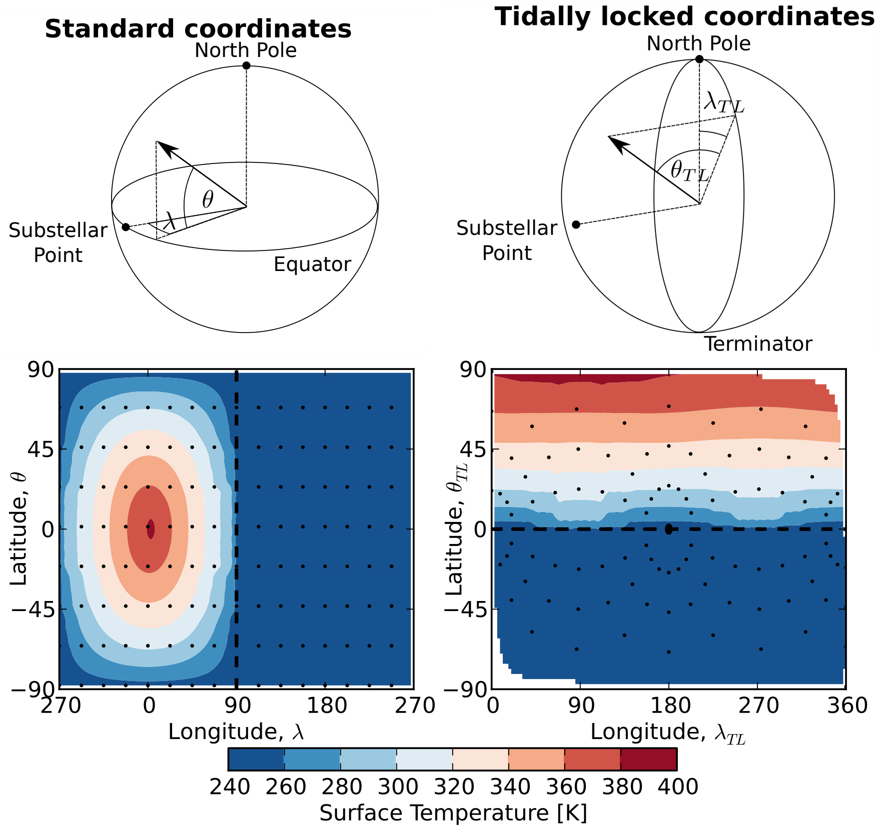

Figure 2.1: Slowly rotating tidally locked planets are approximately symmetric about the substellar point. Surface temperature from the reference simulation in Table 2.1 is shown in two different coordinate systems. The black dashed line is the terminator. Left: In standard coordinates, longitude $\lambda > 90^\circ$ corresponds to the nightside and the substellar point is located at latitude/longitude $(\theta, \lambda) = (0^\circ, 0^\circ)$. Right: In tidally locked coordinates, tidally locked latitude $\theta_{TL} < 0^\circ$ corresponds to the nightside and the substellar point is located at tidally locked latitude $\theta_{TL} = 90^\circ$ (see Appendix B). For illustration, black dots mark every 64th GCM grid point.

algorithms. For example, the momentum equations are implemented using numerical dissipation via horizontal ∇^8 hyperdiffusion. The hyperdiffusivity is chosen to damp the smallest resolved scale on a time scale of 12 hours, which sets a dissipative timescale. The dynamical core also uses a Robert-Asselin time filter, which is controlled by another nondimensional parameter. Our assumption, which we test in Section 2.3, is that the equations described in Appendix A capture the most important physics simulated by the GCM.

Although the GCM uses standard latitude-longitude coordinates, we adopt a tidally locked coordinate system to present our numerical results. Tidally locked planets in relatively long-period orbits tend to exhibit a strong symmetry about the axis connecting the substellar and antistellar points. Figure 2.1 shows the surface temperature in our first reference simulation, which is a cool, slowly rotating, Earth-sized planet with $(a, \Omega, T_{eq}) = (a_{\oplus}, 2\pi/[50\text{days}], 283K)$ (see Table 2.1). The surface temperature is symmetric because the reference simulation is in a slowly rotating dynamical regime, $a^2/L_{Ro}^2 \ll 1$. The symmetry is not perfect, but it captures the dominant spatial variability. We therefore define a tidally locked coordinate system with a tidally locked latitude θ_{TL} and longitude λ_{TL}, where θ_{TL} is the angle away from the terminator and λ_{TL} is the angle about the substellar point (see Fig. 2.1b, Appendix B).

To compute phase curves we follow Cowan & Agol (2008) and assume an edge-on viewing geometry (see Appendix C). We normalize the disk-integrated fluxes by $F_{rock} \equiv 2/3 \times L_*(1-\alpha)$, which is the dayside-averaged observer-projected flux emitted by a planet without an atmosphere. A bare rock will therefore have a nondimensional phase curve, F/F_{rock}, that varies between zero and one. On the other hand, a planet with efficient heat transport will have a constant phase curve equal to[6] $F/F_{rock} = \sigma_{SB}T_{eq}^4/F_{rock} = 3/8$. We also define the phase curve peak-to-trough amplitude as the normalized difference between the phase curve maximum and minimum, $(F_{max} - F_{min})/F_{rock}$.

2.3 Sensitivity of phase curves to nondimensional parameters

First, we test whether our model (with six nondimensional parameters) captures the main physics of dry, tidally locked atmospheres. We consider our model adequate if different GCM simulations produce identical climates when their nondimensional parameters are identical. Our reference case is a cool, slowly rotating, Earth-sized planet (Table 2.1). Figure 2.2 compares the reference case to simulations in which we change dimensional parameters, but keep the six nondimensional parameters fixed (parameter choices are shown in Table 2.1a).

---

[6] We note that the ratio is not 1/2. It would be 1/2 if we were comparing only dayside-averaged fluxes. The ratio is less here because we have to additionally account for the observer-projected viewing geometry, i.e., hotter regions closer to the substellar point appear more prominent to the observer.

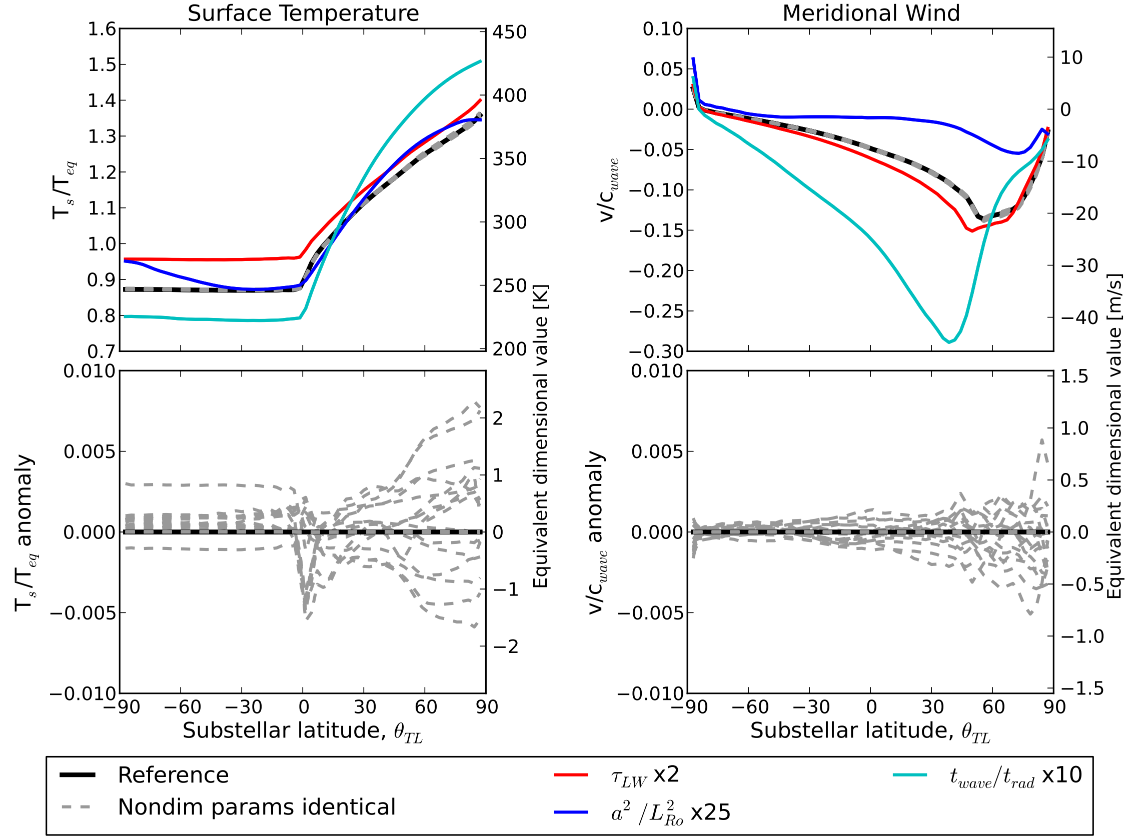

Figure 2.2: Atmospheres have identical dynamics if their nondimensional parameters are identical. Top row: Colored curves show simulations in which we vary the nondimensional parameters. In contrast, gray dashed curves are simulations in which dimensional parameters are varied, but nondimensional parameters stay fixed (see Table 2.1a). Bottom row: the deviation from the reference when nondimensional parameters stay fixed is $\leqslant 1\%$ for surface temperature (left) and generally $\lesssim 3\%$ for wind velocities (right). Notice the difference in y-range between the top and bottom row. In addition, plots are shown in tidally locked coordinates and all quantities are averaged over tidally locked longitude (see Fig. 2.1). The meridional wind is given by the mass-weighted vertical average of meridional wind between $0.15 \leqslant p/p_s \leqslant 0.5$. Wind velocities are negative because the flow is away from the substellar point.

We find that the nondimensional surface temperature, T_s/T_{eq}, differs less than 1% between the reference simulation and the simulations with fixed nondimensional parameters. The nondimensional meridional wind velocity, v/c_{wave}, in the upper troposphere is more variable, and differs by $\lesssim 3\%$ over most of the model domain. The largest deviation in meridional wind is $\sim 30\%$ near the antistellar point. The deviation partly arises because we project simulated wind speeds into a tidally locked coordinate system, which mixes the wind vector components. If we instead consider the total wind speed, $\sqrt{u^2 + v^2}/c_{wave}$, the deviation is $< 10\%$. Moreover, $v \rightarrow 0$ at the antistellar point, requiring longer averaging periods, and wave breaking occurs on the nightside, creating small-scale structure and numerical dissipation. Both effects can lead to deviations from dynamical similarity. For comparison we show some simulations in which we vary the nondimensional parameters (colored curves in Figure 2.2). In these simulations surface temperature and wind velocities change up to 300% compared with the reference, which demonstrates that the dynamical similarity predicted by the nondimensionalization is not trivial. We conclude that the above six nondimensional parameters are sufficient to capture the most important dynamics of the idealized GCM simulations.

Next, we explore how sensitive phase curves are to each of the nondimensional parameters. We consider different reference simulations and vary their nondimensional parameters one at a time to see how this affects the resulting phase curves. For the reference simulations we consider different scenarios where a, Ω, and T_{eq} are fixed. We do so because a, Ω, and T_{eq} are relatively easily constrained for a transiting planet. To vary one nondimensional parameter at a time we first find all possible transformations of the dimensional parameters that only modify a given nondimensional parameter (see Appendix D). For example, to decrease t_{wave}/t_{rad} we could increase p_s but adjust κ_{SW} and κ_{LW} such that γ and τ_{LW} remain constant. We then use these transformations to vary each nondimensional parameter over its largest range compatible with fixed (a, Ω, T_{eq}) and the constraints in Table 2.2.

We find that, for most planets, only the phase curve peak-to-trough amplitude is robustly sensitive to changes in the nondimensional parameters. We start with the above reference scenario of a cool, slowly rotating planet. The dashed curve in Figure 2.3 shows the phase curve of the reference simulation. The planet's thermal flux is phase-locked with the incoming stellar radiation, that is, there is no hot spot phase offset. The phase-locking arises because all stellar radiation is absorbed at the ground ($\gamma = 0$), while a significant part of this energy

Dimensional and Nondimensional parameters	
Reference:	
$a = a_\oplus$, $\Omega = 2\pi/(50 \text{ days})$, $T_{eq} = 283\text{K}$, $R = R_{N_2}$, $c_p = c_{p,N_2}$, p_s=1 bar, $g = 10$ m s^{-2}, $\kappa_{LW} = 10^{-4}$ m^2 kg^{-1}, κ_{SW}=0	$\left(\frac{R}{c_p}, a^2/L_{Ro}^2, \frac{t_{wave}}{t_{rad}}, \gamma, \tau_{LW}, C_D\frac{a}{H}\right)$ $= \left(0.29, 0.12, 5.1 \times 10^{-3}, 0, 1, 1.4\right)$
(a) In 16 simulations we vary the dimensional parameters while keeping all nondimensional parameters fixed. For comparison, in the bottom three simulations we allow the nondimensional parameters to change. Below: relative to reference.	
$(R, c_p, C_D) \times 2, \Omega \times 2^{1/2}, p_s \times 2^{-3/2}, \kappa_{LW} \times 2^3$	same as reference
$(R, c_p, C_D) \times 2^{-1}, \Omega \times 2^{-1/2}, p_s \times 2^{3/2}, \kappa_{LW} \times 2^{-3}$	...
$(R, c_p, g) \times 2, \Omega \times 2^{1/2}, p_s \times 2^{-1/2}, \kappa_{LW} \times 2^2$	...
$(R, c_p, g) \times 2^{-1}, \Omega \times 2^{-1/2}, p_s \times 2^{1/2}, \kappa_{LW} \times 2^{-2}$	...
$(R, c_p, g) \times 5, \Omega \times 5^{1/2}, p_s \times 5^{-1/2}, \kappa_{LW} \times 5^2$	...
$(R, c_p, g) \times 5^{-1}, \Omega \times 5^{-1/2}, p_s \times 5^{1/2}, \kappa_{LW} \times 5^{-2}$	...
$(\Omega, g, \kappa_{LW}) \times 2, a \times 2^{-1}$	...
$(\Omega, g, \kappa_{LW}) \times 2^{-1}, a \times 2^1$	...
$\Omega \times (\frac{5}{4})^{1/2}, (T_{eq}, g) \times \frac{5}{4}, p_s \times (\frac{5}{4})^{7/2}, \kappa_{LW} \times (\frac{5}{4})^6$	...
$\Omega \times (\frac{4}{5})^{1/2}, (T_{eq}, g) \times \frac{4}{5}, p_s \times (\frac{4}{5})^{7/2}, \kappa_{LW} \times (\frac{4}{5})^6$	...
$(a, R, c_p) \times \frac{3}{2}, (\Omega, p_s) \times (\frac{3}{2})^{-1/2}, \kappa_{LW} \times \frac{3}{2}$	...
$(a, R, c_p) \times 2, (\Omega, p_s) \times 2^{-1/2}, \kappa_{LW} \times 2$	...
$(a, R, c_p) \times \frac{2}{3}, (\Omega, p_s) \times (\frac{2}{3})^{-1/2}, \kappa_{LW} \times \frac{2}{3}$	...
$(a, R, c_p) \times \frac{1}{2}, (\Omega, p_s) \times (\frac{1}{2})^{-1/2}, \kappa_{LW} \times \frac{1}{2}$	...
$(R, c_p, C_D) \times 5, \Omega \times 5^{1/2}, p_s \times 5^{-3/2}, \kappa_{LW} \times 5^3$	...
$(R, c_p, C_D) \times \frac{1}{5}, \Omega \times (\frac{1}{5})^{1/2}, p_s \times (\frac{1}{5})^{-3/2}, \kappa_{LW} \times (\frac{1}{5})^3$	...
$\kappa_{LW} \times 2$	$\tau_{LW} \times 2$
$\Omega = 2\pi/(2 \text{ days})$	$a^2/L_{Ro}^2 \times 25$
$p_s/10$, $\kappa_{LW} \times 10^2$	$t_{wave}/t_{rad} \times 10$
(b) This illustrates how we vary one nondimensional parameter at a time, while keeping other nondimensional parameters fixed (also see Appendix D). The dimensional parameters remain within the constraints shown in Table 2.2. Below: relative to reference.	
$c_p \times 1.5, (R, g) \times 1.5^{1/2}, p_s \times 1.5^{-1/2}, \kappa_{LW} \times 1.5^{3/2}$	$R/c_p \times 0.82$
$(R, c_p, C_D) \times 0.75, p_s \times 0.75^{-3/2}, \kappa_{LW} \times 0.75^3$	$a^2/L_{Ro}^2 \times 1.15$
$(R, c_p, C_D) \times 4.64, p_s \times 4.64^{-3/2}, \kappa_{LW} \times 100$	$a^2/L_{Ro}^2 \times 0.46$
$p_s \times 6.32^{-1}, g \times 2.5, C_D \times 2.5^{-1}, \kappa_{LW} \times 100$	$t_{wave}/t_{rad} \times 15.8$
$p_s \times 0.1, \kappa_{LW} \times 100$	$t_{wave}/t_{rad} \times 10$
$p_s \times 0.5, \kappa_{LW} \times 4$	$t_{wave}/t_{rad} \times 2$
$p_s \times 2^{1/2}, \kappa_{LW} \times 0.5$	$t_{wave}/t_{rad} \times 0.71$
$p_s \times 3.162, \kappa_{LW} \times 0.1$	$t_{wave}/t_{rad} \times 0.32$
$p_s \times 2, g \times 2.5^{-1}, C_D \times 2.5, \kappa_{LW} \times 0.1$	$t_{wave}/t_{rad} \times 0.2$
$\kappa_{SW} = 5 \times 10^{-5}$	$\gamma = 0.5$
$\kappa_{SW} = 10^{-4}$	$\gamma = 1$
$\kappa_{LW} \times 100$	$\tau_{LW} \times 100$
$\kappa_{LW} \times 0.1$	$\tau_{LW} \times 0.1$
$C_D \times 10, (g, p_s) \times 2.5, \kappa_{LW} \times 0.4$	$C_D a/H \times 25$
$C_D \times 10$	$C_D a/H \times 10$
$C_D \times 0.1$	$C_D a/H \times 0.1$
$C_D \times 0.1, (g, p_s) \times 2.5^{-1}, \kappa_{LW} \times 2.5$	$C_D a/H \times 0.04$

Table 2.1: (a) Parameters for the simulations in Figure 2.2. (b) Parameter bounds for the simulations in Figures 2.3 and 2.4a. The drag coefficient C_D is not a fixed parameter in the model, so the values shown for $C_D\frac{a}{H}$ is only approximate. Symbols for dimensional parameters are defined in Table 2, nondimensional parameters are defined in Section 2.2.

Dimensional Parameter	Symbol	Unit	Min. value	Max. value
Planetary radius	a	$a_\oplus$	1	2
Rotation rate	Ω	days^{-1}	$2\pi/50$	$2\pi/2$
Equilibrium temperature	T_{eq}	K	100	600
Surface gravity	g	10 m s^{-2}	$\frac{2}{5} \times (a/a_\oplus)$	$\frac{5}{2} \times (a/a_\oplus)$
Specific heat capacity	c_p	J kg^{-1} K^{-1}	820	14230
Specific gas constant	R	J kg^{-1} K^{-1}	190	4157
Surface pressure	p_s	bar	10^{-2}	10
Longwave opacity[a]	κ_{LW}	m^2/kg	10^{-5}	10^{-2}
Shortwave opacity[a]	κ_{SW}	m^2/kg	0	10^{-2}
Surface drag coefficient	C_D, via k_{vk}	-	$\times 0.1$	$\times 10$

[a] Opacities are defined at a reference pressure of $p_0 = 1$ bar.

Table 2.2: Maximal range of dimensional values we consider. For a given reference simulation we fix (a, Ω, T_{eq}), and change the remaining dimensional parameters such that only one nondimensional parameter varies at a time. C_D is not a fixed parameter, so we vary the von-Karman constant k_{vk} to increase and decrease C_D by an order of magnitude. We vary R and c_p, but require that R/c_p stays within the range of diatomic and triatomic gases ($0.22 \lesssim R/c_p \leqslant 0.29$; section 2.3.3, Pierrehumbert, 2011b). The maximum value of R and c_p corresponds to H_2, the minimum value to CO_2. In addition we require that shortwave optical depth does not exceed longwave optical depth ($\gamma \leqslant 1$).

can also escape directly from the ground to space without being advected ($\tau_{LW} = 1$). We note that the cold spot offset is larger than the hot spot offset; however, it would be difficult to detect the cold spot offset because the phase curve is approximately constant near the antistellar point (dashed curve in Fig. 2.3). Next, we vary each nondimensional parameter while keeping the other nondimensional parameters fixed (Table 2.1b). The grey lines in Figure 2.3 show how the phase curve varies in response to changes in the nondimensional parameters. We find that the phase curve generally stays phase-locked with the stellar radiation. This only changes once the atmosphere becomes optically thick ($\tau_{LW} \gg 1$), but in those cases the offset would again be hard to detect because the planet's thermal emission essentially does not vary (approximately constant curves in Fig. 2.3). In contrast to the negligible hot/cold spot offsets, the phase curve amplitude is much more sensitive to changes in the nondimensional parameters (Fig. 2.3).

We explore other reference simulations to see when hot/cold spot offsets become significant. We find that significant hot/cold spot offsets only occur when the the atmosphere is

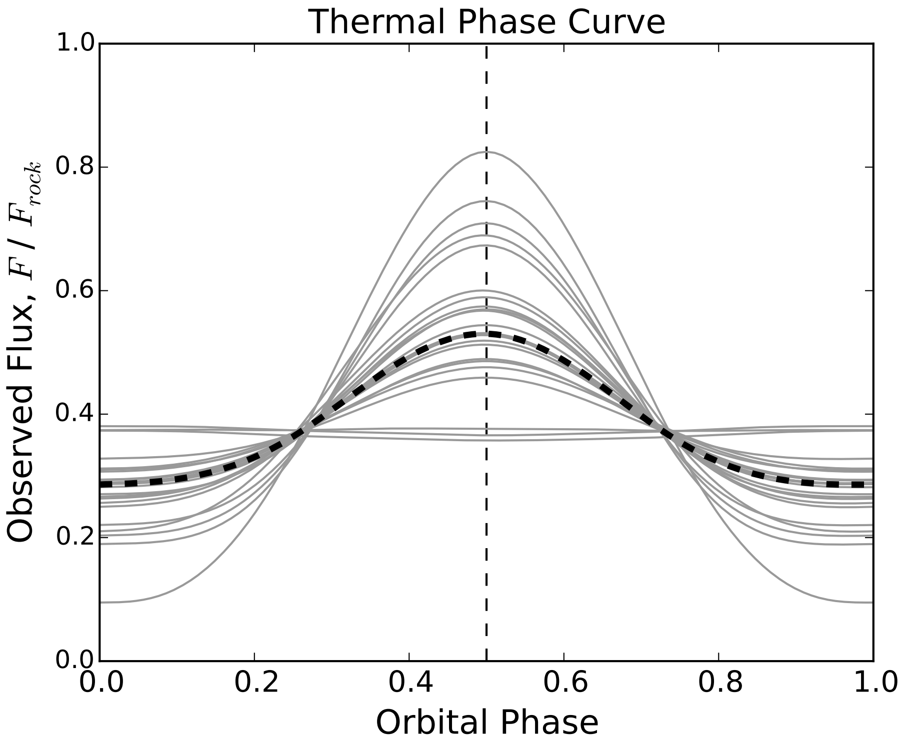

Figure 2.3: For many terrestrial planets, the phase curve's peak-to-trough amplitude is sensitive to changes in the atmospheric parameters whereas hot/cold spot offsets are small. The dashed black line shows the phase curve for the reference simulation in Table 2.1, and the vertical line indicates secondary eclipse. We explore different atmospheric scenarios by varying each nondimensional parameter that influences the atmospheric dynamics while keeping the other nondimensional parameters fixed (Table 2.1b). The approximately constant curves correspond to optically thick atmospheres ($\tau_{LW} \geqslant 10$). The simulations shown here all assume $(a, \Omega, T_{eq}) = (a_{\oplus}, 2\pi/[50 \text{ days}], 283 \text{ K})$; for symbol definitions see Table 2.2.

optically thick, $\tau_{LW} \gg 1$, the planet has a high rotation rate, $a^2/L_{Ro}^2 \gtrsim 1$, and is relatively hot, $t_{wave}/t_{rad} \gtrsim 0.01$. Table 2.3 summarizes our results. While a cool and slowly rotating planet with $\tau_{LW} = 10$ shows a hot spot offset of up to 82°, the phase curve in that case is almost constant and the offset therefore not detectable (second-to-bottom row in Table 2.3). Only in the hottest and most rapidly rotating scenario with $\tau_{LW} \gg 1$ that we consider do we find a large hot spot offset of 26° which would also be detectable (bottom row in Table 2.3). If future observations found a large hot spot offset, this would therefore not only imply that the planet has an atmosphere, but also that the atmosphere would have to be optically thick. Many terrestrial planets, however, should have small hot spot offsets (Table 2.3). For

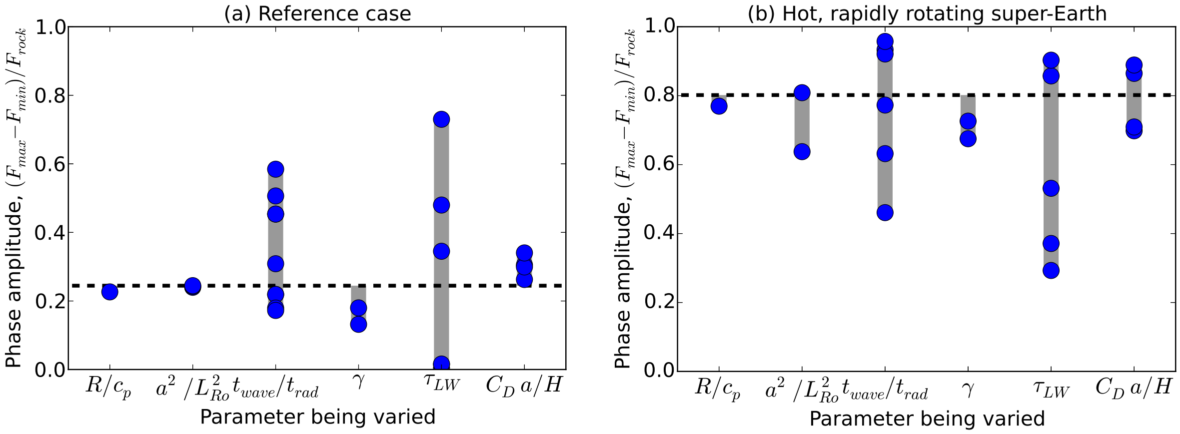

Figure 2.4: Except for hot and rapidly rotating planets, the phase curve peak-to-trough amplitude is primarily sensitive to t_{wave}/t_{rad} and τ_{LW}. As in Figure 2.3, we vary each nondimensional parameter while keeping the other nondimensional parameters fixed. The nondimensional parameters are defined in Section 2.2. Dashed black lines show the phase amplitude of the reference simulations, blue dots show the phase amplitude as nondimensional parameters are varied, and vertical bars indicate the maximal variation of amplitude, i.e., sensitivity, for each nondimensional parameter. Left: reference simulation assumes $(a, \Omega, T_{eq}) = (a_\oplus, 2\pi/[50 \text{ days}], 283 \text{ K})$. Right: reference simulation assumes $(a, \Omega, T_{eq}) = (2a_\oplus, 2\pi/[2 \text{ days}], 600 \text{ K})$.

the rest of this paper we therefore focus on the phase amplitude, and how it could be used to characterize the atmosphere of a planet.

We find that, except for hot and rapidly rotating planets, the phase amplitude is primarily sensitive to the ratio of dynamical to radiative timescales, t_{wave}/t_{rad}, and the optical depth, τ_{LW}. We again start with the reference scenario of a cool, slowly rotating planet. The dashed line in Figure 2.4a shows the reference phase amplitude, $(F_{max} - F_{min})/F_{rock}$, and the vertical lines show how sensitive the phase amplitude is to changes in each nondimensional parameter. The phase amplitude is far more sensitive to t_{wave}/t_{rad} and τ_{LW} than to any of the other nondimensional parameters. For example, when we vary t_{wave}/t_{rad} (primarily by changing g and p_s, while adjusting other parameters; see Table 2.1b), the phase amplitude varies between 0.2 and 0.6. In contrast, when we vary the nondimensional Rossby radius, a^2/L_{Ro}^2 (by changing R, and thus c_{wave}, while adjusting other parameters), the phase amplitude varies by less than 0.01. We emphasize this does not mean that the

Reference parameters						Reference	Ref. hot	Amplitude sensitivity to					
$\frac{R}{c_p}$	$\frac{a^2}{L_{Ro}^2}$	$\frac{t_{wave}}{t_{rad}}$	γ	τ_{LW}	$C_D\frac{a}{H}$	amplitude	spot offset	$\frac{R}{c_p}$	$\frac{a^2}{L_{Ro}^2}$	$\frac{t_{wave}}{t_{rad}}$	γ	τ_{LW}	$C_D\frac{a}{H}$
0.29	0.12	5.1×10^{-3}	0	1	1.4	0.24*	0°	+0 -0.02	+0 -0	+0.31 -0.08	+0 -0.11	+0.49 -0.24	+0.1 -0
0.29	0.3	5.1×10^{-3}	0	1	1.4	0.26	3°	+0 -0.02	+0 -0.01	+0.32 -0.07	+0 -0.11	+0.48 -0.25	+0.09 -0
0.29	0.6	1×10^{-2}	0	1	2.8	0.36	3°	+0 -0.03	+0.02 -0.05	+0.34 -0.11	+0 -0.16	+0.42 -0.32	+0.06 -0.02
0.29	4.1	6.6×10^{-2}	0	1	1.3	0.8**	7°	+0 -0.03	+0.01 -0.16	+0.16 -0.34	+0 -0.13	+0.1 -0.51	+0.09 -0.1
0.29	10	7.6×10^{-4}	0	1	8.1	0.19	0°	+0 -0.03	+0 -0.03	+0.32 -0	+0 -0.07	+0.48 -0.14	+0.04 -0.03
0.29	0.12	5.1×10^{-3}	0.5	10	1.4	0.01	82°	+0 -0	+0 -0	+0 -0.01	+0 -0.01	+0.71 -0.01	+0 -0
0.29	4.1	6.6×10^{-2}	0.5	10	1.4	0.5	26°	+0 -0.05	+0.04 -0.17	+0.13 -0.31	+0.03 -0	+0.37 -0.01	+0.06 -0.08

Table 2.3: We explore a broad range of atmospheric scenarios. The six columns on the left show the nondimensional parameters for the reference simulations, the center two columns show the phase curve amplitude and the hot spot offset in the reference simulation, and the six columns on the right show the maximum/minimum change in phase curve amplitude in response to each nondimensional parameter. The large font emphasizes entries with phase amplitude sensitivity bigger than 0.1. The top row, $*$, corresponds to the cool slowly rotating scenario in Figures 2.3 and 2.4a, and the fourth row from the top, $**$, corresponds to the hot and rapidly rotating scenario in Figure 2.4b.

atmospheric dynamics or phase curve are insensitive to a^2/L_{Ro}^2 in general. As we show in the next paragraph, a^2/L_{Ro}^2 can affect phase curves when $a^2/L_{Ro}^2 \gtrsim 1$. However, for this particular scenario, once (a, Ω, T_{eq}) are known then a^2/L_{Ro}^2 is already constrained to be much smaller than one. The remaining observational uncertainty in a^2/L_{Ro}^2 barely affects our interpretation of the planet's phase curve amplitude. Figure 2.4a therefore shows that, for cool, slowly rotating planets with known (a, Ω, T_{eq}), a phase curve measurement contains essentially no information about the parameters R/c_p, a^2/L_{Ro}^2, γ, and $C_D a/H$. On the other hand, a measurement of the phase amplitude would constrain the combination of t_{wave}/t_{rad} and τ_{LW}.

We explore other reference simulations to determine whether there are regimes in which the phase amplitude is sensitive to other parameters. Similar to our result for hot spot offsets, we find that phase amplitude only becomes sensitive to a^2/L_{Ro}^2, γ, and $C_D a/H$ for large, hot, and rapidly rotating planets. Specifically, a planet has to have both $a^2/L_{Ro}^2 \gtrsim 1$ and $t_{wave}/t_{rad} \gtrsim 0.01$ for additional nondimensional parameters to affect the phase amplitude. Our results are summarized on the right-hand side of Table 2.3. We find that, in all scenarios, the phase amplitude is most sensitive to t_{wave}/t_{rad} and τ_{LW}. We also find that a^2/L_{Ro}^2 and t_{wave}/t_{rad} both have to be large for the phase amplitude to become sensitive to additional parameters; a large value of a^2/L_{Ro}^2 by itself is not sufficient (third-to-bottom row in Table 2.3). Together with our above result that hot spot offsets also require $a^2/L_{Ro}^2 \gtrsim 1$ and $t_{wave}/t_{rad} \gtrsim 0.01$, this suggests that a regime shift occurs in the atmospheric dynamics near this threshold. Figure 2.4b shows the scenario in which phase amplitude is most sensitive to additional parameters (** in Table 2.3). This scenario corresponds to a super-Earth with $(a, \Omega, T_{eq}) = (2a_{\oplus}, 2\pi/[2\text{days}], 600K)$. In this scenario the phase amplitude is additionally sensitive to variations in a^2/L_{Ro}^2, γ, and $C_D a/H$ (Fig. 2.4b). For such a planet, a measurement of the phase amplitude would be degenerate with multiple atmospheric parameters, although the hot/cold spot offsets could provide additional information (Table 2.3). Many terrestrial planets, however, will have phase amplitudes that are, to good approximation, only sensitive to t_{wave}/t_{rad} and τ_{LW} (Table 2.3).

2.4 Application to *JWST* observations

For planets whose phase curves primarily depend on the ratio of dynamical to radiative timescales, t_{wave}/t_{rad}, and the optical depth, τ_{LW}, we consider how a phase curve could constrain an atmosphere's properties. Expanded in terms of dimensional quantities, the two nondimensional parameters are $ag\sigma_{SB}T_{eq}^{5/2}/(p_s R c_p^{1/2})$ and $\kappa_{LW}p_s^2/(gp_0)$. The most important unknowns are the longwave opacity at a reference pressure, κ_{LW}, and the surface pressure, p_s, because the other dimensional parameters are relatively easy to constrain. For a transiting planet, the planetary radius, a, would be known. One can constrain the equilibrium temperature, T_{eq}, because a planet's broadband thermal emission averaged over one orbit is equal to $\sigma_{SB}T_{eq}^4$. The specific gas constant and heat capacity, R and c_p, vary most significantly between H_2-dominated atmospheres and high mean-molecular-weight atmospheres. Because R also sets the atmospheric scale height, a transit spectrum could be sufficient to distinguish between an H_2 and a high mean-molecular-weight atmosphere. If one can determine whether an atmosphere is H_2-dominated or not, the detailed value of R and c_p is secondary; for example, t_{wave}/t_{rad} only varies by a factor of 2 between a pure N_2 atmosphere and a pure CO_2 atmosphere. The surface gravity, g, can be constrained via radial-velocity or transit-timing measurements. Moreover, interior models indicate that bulk compositions ranging from water ice to iron would only change the bulk density, and thus g, by a factor of ~ 2 (Seager et al., 2007). In contrast, κ_{LW} and p_s can change the values of t_{wave}/t_{rad} and τ_{LW} by several orders of magnitude.

This means a planet's phase amplitude can be used to characterize longwave opacity, κ_{LW}, and surface pressure, p_s. To evaluate the feasibility of doing so, we estimate the observable phase amplitude signal and the precision possible with *JWST*. For the signal we assume an optimistic scenario similar to that assumed by Yang et al. (2013). Specifically, we assume a cool super-Earth with $(a, T_{eq}, \Omega, g, R, c_p) = (2a_\oplus, 300K, 2\pi/[10\text{days}], 20\text{m s}^{-2}, R_{N_2}, c_{p,N_2})$, orbiting a GJ1214-like star with $(a_*, T_*) = (0.2a_\odot, 3000K)$. We assume the star is 5 pc away, and the phase curve is observed between transit and secondary eclipse, for 5 days total. This planet would have $a^2/L_{Ro}^2 \sim 1$. That is roughly the regime for which our findings start to apply, i.e., the planet's phase amplitude largely depends on only two nondimensional parameters. Cooler and/or smaller planets would be even more solidly in the slowly rotating and cool regime, but more difficult to observe. We performed simulations that explore the phase amplitude as a function of κ_{LW} and p_s. For a given simulation we compute the normalized phase amplitude $(F_{max} - F_{min})/F_{rock}$. We multiply this amplitude by the planet-star contrast of a bare rock, F_{rock}/F_*, to get the phase amplitude relative to the stellar flux, $(F_{max} - F_{min})/F_*$. To compute F_{rock}/F_* we approximate the planetary and stellar emission as blackbody radiation. Following Yang et al. (2013), the planet-star contrast in some band $[\lambda_1, \lambda_2]$ is then

$$\frac{F_{rock}}{F_*} = \left(\frac{a}{a_*}\right)^2 \frac{\int_{\lambda_1}^{\lambda_2} B(T_{rock}, \lambda) d\lambda}{\int_{\lambda_1}^{\lambda_2} B(T_*, \lambda) d\lambda}.$$

Here B is the Planck function, and T_{rock} is the dayside-averaged observer-projected temperature of a bare rock (Appendix C). We assume $16.5 \leqslant \lambda \leqslant 19.5$ μm, which corresponds to the F1800W filter on *JWST*'s Mid-Infrared Instrument (MIRI). We choose this band because it avoids the 15 μm CO_2 absorption feature, but other spectral window regions would be similarly suitable. For a bare rock the phase amplitude would be $(F_{max} - F_{min})/F_* = (F_{rock} - 0)/F_* = 358$ ppm, while an atmosphere with perfect day-night heat transport would have a phase amplitude of 0 ppm.

To estimate the precision possible with *JWST*, we assume that the observational error is dominated by stellar photon noise. In the photon noise limit the precision is $\sigma/F_* = 1/\sqrt{N}$, where the number of stellar photons N is

$$N = \pi \left(\frac{D}{2}\right)^2 \Delta t \left(\frac{a_*}{d}\right)^2 \int_{\lambda_1}^{\lambda_2} \frac{B(T_*, \lambda)}{E(\lambda)} d\lambda.$$

Here D is the diameter of *JWST*'s mirror (=6.5m), Δt is the length of observation, d is the

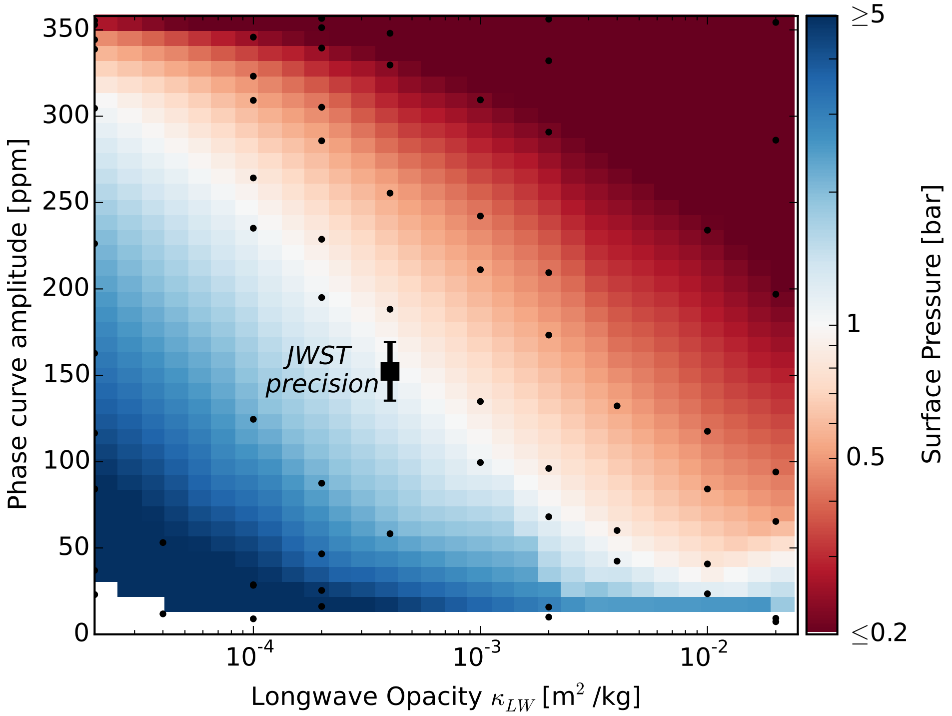

Figure 2.5: This figure illustrates how the observed phase curve amplitude, $[F_{max} - F_{min}]/F_*$, (y-axis) can be used to infer the surface pressure of a planet (colors). Black dots indicate simulations, and the color scale is interpolated between simulations. A given amplitude is compatible with both a thin atmosphere that is opaque to longwave radiation (large κ_{LW}) and a thick atmosphere that is transparent to longwave radiation (small κ_{LW}). If κ_{LW} is known, for example from transit spectroscopy, then the phase curve constrains surface pressure and atmospheric mass. We assume a super-Earth around a GJ1214b-like star, such that a bare rock would exhibit a phase curve amplitude near 18 μm of 358 ppm. The black square shows a representative 1 bar atmosphere, and the error bars show our optimistic estimate for *JWST*'s $\pm 1\sigma$ precision on the phase amplitude (see Section 2.4). For reference, opacities in Solar System atmospheres tend to fall within an order of magnitude of $\kappa_{LW} \sim 10^{-3}$ m^2 kg^{-1} (Robinson & Catling, 2014).

distance between observer and star, and $E(\lambda) = hc/\lambda$ is the energy per photon. We first make an optimistic estimate for the precision. Recent measurements with the *Hubble Space Telescope* almost reached the photon noise limit (Kreidberg et al., 2014; Knutson et al., 2014), and we assume *JWST* will do similarly well. To account for imperfect instrument throughput and detector efficiency we degrade the photon-limited precision by a factor of 1/3 (Fig. 3, Glasse et al., 2010). We find that, over a 12 hour integration, *JWST* should be able to measure the planet-star flux ratio with a precision of 12 ppm[7]. Because the phase amplitude is the difference between two fluxes, the 3σ uncertainty interval for the phase amplitude is[8] $\sqrt{2} \times 3 \times 12$ ppm $= 51$ ppm. For a pessimistic estimate we repeat the previous calculation, but additionally impose a noise floor of 40 ppm. This floor represents unexpected instrumental systematics, zodiacal light or other noise sources. With this noise floor, a 12 hour integration would only reach 10% of the photon noise limit. Given that *Spitzer* measurements were able to reach $\sim$ 30% of the photon noise limit (Fig.3, Cowan et al., 2012), we consider this estimate very pessimistic. In this case a 2σ (3σ) measurement of the phase amplitude would have a precision of $\sqrt{2} \times 2 \times 40 = 113$ (170) ppm.

Figure 2.5 shows our simulation results and optimistic 1σ precision estimate. We find that thin atmospheres ($p_s \leqslant 0.2$ bar) have phase amplitudes close to 358 ppm for small and moderate values of κ_{LW} ($\leqslant 10^{-3}$ m^2 kg^{-1}). Taking into account measurement uncertainties of $\sim$ 50 ppm, these atmospheres would be difficult to distinguish from bare rocks. Similarly, thick atmospheres ($p_s > 5$ bar) tend to have phase amplitudes close to zero. A phase curve would constrain atmospheric mass most effectively between those two limits. Figure 2.5 also shows that, between those limits, the phase amplitude is sensitive to both κ_{LW} and p_s. We find that any observed phase amplitude would be compatible with both a thin atmosphere that is opaque to longwave radiation (large κ_{LW}) and a thick atmosphere that is transparent to longwave radiation (small κ_{LW}). Nevertheless, if transit or emission spectroscopy could determine the concentration of greenhouse gases in an atmosphere, and therefore κ_{LW}, the phase amplitude would yield the value of p_s. As an example we highlight a simulation with a 1 bar atmosphere and $\kappa_{LW} = 4 \times 10^{-4}$ m^2 kg^{-1} (black square in Fig. 2.5). The exact value of this atmosphere's phase amplitude is 152 ppm. The observed phase amplitude would

---

[7] We note that Yang et al. (2013) similarly estimate *JWST* precisions assuming the photon noise limit. However, those calculations contained an error and the resulting estimates are too small by a factor of a few (N. Cowan, personal communication).

[8] The factor of $\sqrt{2}$ assumes that uncertainties between different observation periods are uncorrelated. The uncertainty on the phase amplitude is then related to the uncertainty of a single observation period as $\sigma_{amplitude} = \sqrt{\sigma_{single}^2 + \sigma_{single}^2} = \sqrt{2}\sigma_{single}$.

therefore be 152 ± 51 ppm with 3σ confidence, which constrains the surface pressure to $0.7 \leqslant p_s \leqslant 1.3$ bar. Even using our pessimistic precision estimate, we find that *JWST* would be able to constrain surface pressure to $0.5 \leqslant p_s \leqslant 2.3$ bar, albeit only with 2σ confidence (152 ± 113 ppm). We further note that our pessimistic precision estimate would only place a lower bound on the surface pressure, $p_s \geqslant 0.2$ bar, with 3σ confidence (152 ± 170 ppm). These values are the most precise constraints that the phase curve amplitude can place on surface pressure, because we assumed the other dimensional parameters (κ_{LW},R,c_p, etc.) are already well characterized via transit or emission spectroscopy. Observational uncertainties in the other dimensional parameters would increase the uncertainty in the inferred surface pressure. Nevertheless, our results show that a phase amplitude measurement can place meaningful bounds on a planet's atmospheric mass, while the necessary observation time is competitive with the time required to constrain atmospheric mass via transit or emission spectroscopy (cf. Section 2.1).

2.5 Discussion

Dimensional analysis is a crucial tool in comparative planetology and the study of exoplanets (Golitsyn, 1970; Mitchell & Vallis, 2010; Showman et al., 2010; Read, 2011; Potter et al., 2013; Del Genio, 2013; Mitchell et al., 2014). Our approach highlights the utility of the Buckingham-Pi theorem for the study of planetary atmospheres (cf. Frierson, 2005). We show that the primitive equations coupled to the two-stream equations are governed by a fairly small set of nondimensional parameters. These nondimensional parameters also encapsulate the atmospheric dynamics of an idealized GCM. Our analysis reveals basic dimensional degeneracies, which could allow modelers to sample large parameter spaces more efficiently (Fig. 2.2, Appendix D). It is straightforward to expand our analysis to include additional physics, for example, moist thermodynamics, multi-band radiation, non-hydrostatic atmospheres, chemical disequilibrium or magnetohydrodynamics. It follows from the Buckingham-Pi theorem that each additional independent physical parameter will introduce another nondimensional parameter.

Our analysis suggests that the dynamics of gaseous planets could be even easier to understand than the dynamics of terrestrial planets. Gaseous planets do not have a distinct surface, so we suppose that their atmospheric dynamics are to first order independent of the bottom boundary. A range of modeling studies tend to support this assumption (Heng et al., 2011a; Menou, 2012a; Kataria et al., 2013). This means the dynamics are insensitive to the surface friction/heating parameter, $C_D a/H$. We furthermore need to replace the surface pressure, p_s, with a new characteristic pressure. We note that for terrestrial planets p_s denotes the depth of the dynamically active part of the atmosphere, where winds are driven by gradients in the stellar forcing. For a gaseous planet we analogously use the photon deposition depth, that is, the pressure where stellar radiation is absorbed, $p_D \sim \sqrt{g p_0/\kappa_{SW}}$ (see eqn. 117, Heng et al., 2014). The longwave optical depth τ_{LW}, which was previously defined at the surface, now becomes the optical depth at the level of photon deposition, $\tau_{LW} = \kappa_{LW} p_0/g \times (p_D/p_0)^2 = \kappa_{LW}/\kappa_{SW} = \gamma^{-1}$. The last step shows that τ_{LW} and γ cease to be independent degrees of freedom. This is also consistent with the Buckingham-Pi theorem, because we should lose one nondimensional parameter in the limit $p_s \rightarrow \infty$. The dynamics of gaseous planets then depend on only four nondimensional parameters (where p_s is now replaced by p_D):

$$\left(\frac{R}{c_p}, \frac{a^2}{L_{Ro}^2}, \frac{t_{wave}}{t_{rad}}, \gamma\right).$$

This set is sufficiently small for easy numerical exploration. Moreover, observations that cannot be explained by a model with the above four parameters would strongly point to the importance of additional physics, for example, breakdown of well-mixed gaseous opacities (via chemical disequilibrium), non-grey radiative effects, condensation or clouds.

Next, we discuss the observational effort necessary for phase curve observations. While there were initial attempts to monitor phase curves discontinuously with *Spitzer* (Harrington et al., 2006), more recent *Spitzer* observations tend to cover the whole course of an orbit to account for long-term instrumental drift (Knutson et al., 2012). Similar continuous observations with *JWST* would become very time-consuming for planets with period $\gtrsim$10 days. Although we assumed in Section 2.4 that the planet is observed for half an orbit, our results indicate that full phase curve coverage is not necessary as long as hot spot offsets are small or negligible (Fig. 2.3). In theory this means that one only needs to observe a planet's thermal emission near primary and secondary eclipse, which would greatly reduce the required observation time. In practice, it will be challenging to relate the observed thermal fluxes from distinct observation periods, but precise characterization of *JWST*'s instrumental drift might still permit discontinuous observation strategies.

Finally, we discuss further physics that might influence our conclusions. Any model necessarily only approximates the dynamics of real atmospheres. The dynamical similarities predicted by our analysis will break down if processes neglected in our model become significant or if the neglected processes are singular perturbations. We do not expect condensation to be a singular perturbation, given that dry models are able to reproduce many aspects of Earth's atmospheric dynamics (Schneider et al., 2006). For a planet with a condensing substance, our method should provide an upper bound on the atmospheric mass. That is because latent heat transport, and for true Earth analogs ocean heat transport, would increase the day-night energy transport. Clouds would similarly reduce the phase curve amplitude, by reducing the dayside brightness temperature while not strongly affecting the nightside brightness temperature (Yang et al., 2013). If this effect is strong enough it can even reverse the expected day-night phase curve pattern. Detection of a inverted phase curve pattern would therefore be a tell-tale sign of a condensing atmosphere. In all other cases, a planet with a condensing substance should have a reduced phase curve amplitude and thus resemble a dry planet with larger atmospheric mass.

For the radiative transfer, we assume that shortwave and longwave opacities both increase linearly with pressure due to pressure broadening and collision-induced absorption. This assumption breaks down if atmospheric opacities are set by different mechanisms, for example, if shortwave radiation was absorbed by dust (which is insensitive to pressure broadening). We therefore explored simulations in which the shortwave opacity is independent of pressure. We find that reducing the pressure dependency has an effect qualitatively similar to increasing the ratio of shortwave to longwave optical depths, γ, in our standard simulations. Specifically, the resulting increase in shortwave absorption at higher altitudes creates stratospheric inversions, but only has a limited impact on thermal phase curves ($\sim 10-15\%$ decrease in phase amplitude compared to our standard simulations with $\gamma = 1$; see Fig. 2.4).

We also assume that planets are tidally locked, but the effect of atmospheric thermal tides (Cunha et al., 2014) and trapping in higher-order resonances (Makarov et al., 2012) could result in non-synchronous orbital states. Non-synchronous rotation would introduce an additional nondimensional parameter into our model that compares the length of the day-night cycle with the planet's cooling timescale. We do not expect that a small deviation from synchronous rotation would be a singular perturbation of this parameter. Yang et al. (2014) show that non-synchronously rotating planets with sufficiently slow rotation and/or short cooling timescale smoothly approach the tidally locked regime (their Fig. 1a). Such planets rotate non-synchronously but in an instantaneous sense still appear tidally locked. Cunha et al. (2014) show that thermal tides are generally not compatible with synchronous rotation. Nevertheless, the deviation from synchronous rotation is small for planets in close orbits with zero eccentricity around small stars, such as M-dwarfs (Table 2 in Cunha et al., 2014). Unless synchronous rotation represented a singular limit (see above), the potential effect of thermal tides should then not greatly affect the types of planets we consider here. Many terrestrial planets might never reach synchronous rotation and instead get trapped in a higher-order orbital resonance, like Mercury did in our Solar system (Makarov et al., 2012). The probability of being trapped decreases for planets with lower eccentricity (Fig. 6 in Makarov et al., 2012), which means that our assumption of synchronous rotation is at least consistent with the fact that also we do not consider non-zero eccentricities. It is beyond the scope of this article to investigate higher-order spin states, but phase curves at visible wavelengths could provide a consistency check for applying our method to planets with optically thin atmospheres (Fujii et al., 2014).

2.6 Conclusions

We use dimensional analysis to find a set of six nondimensional parameters that captures the main atmospheric dynamics of dry, tidally locked terrestrial planets in an idealized GCM. We use the GCM to investigate the sensitivity of thermal phase curves to each of the nondimensional parameters. Except for hot and rapidly rotating atmospheres that are optically thick in the longwave, we do not find significant hot spot offsets. On the other hand, the phase curve amplitude remains sensitive to changes in the atmospheric parameters across a large range of atmospheric scenarios. Focusing on the phase amplitude, we find that the phase amplitude of many terrestrial planets is sensitive to only two nondimensional parameters. The main unknowns in the two nondimensional parameters are the surface pressure and the longwave opacity. The longwave opacity can be constrained by transit or emission spectroscopy, in which case the phase amplitude would constrain the surface pressure and atmospheric mass. As an example, we estimate that a broadband phase curve near 18 μm with *JWST*, taken over a single half-orbit, could be sufficient to constrain the surface pressure of a cool super-Earth to within a factor of two. Constraints like the one we propose will be crucial for understanding atmospheric evolution, in particular atmospheric escape. Moreover, constraining atmospheric mass is important for characterizing the surface conditions of potentially habitable planets.

CHAPTER 3

TEMPERATURE STRUCTURE AND ATMOSPHERIC CIRCULATION OF TIDALLY LOCKED EXOPLANETS

Next-generation space telescopes will observe the atmospheres of rocky planets orbiting nearby M-dwarfs. Understanding these observations will require well-developed theory in addition to numerical simulations. Here we present theoretical models for the temperature structure and atmospheric circulation of dry, tidally locked rocky exoplanets with grey radiative transfer and test them using a general circulation model (GCM). First, we develop a radiative-convective model that captures surface temperatures of slowly rotating and cool atmospheres. Second, we show that the atmospheric circulation acts as a global heat engine, which places strong constraints on large-scale wind speeds. Third, we develop a radiative-convective-subsiding model which extends our radiative-convective model to hot and thin atmospheres. We find that rocky planets develop large day-night temperature gradients at a ratio of wave-to-radiative timescales up to two orders of magnitude smaller than the value suggested by work on hot Jupiters. The small ratio is due to the heat engine inefficiency and asymmetry between updrafts and subsidence in convecting atmospheres. Fourth, we show using GCM simulations that rotation only has a strong effect on temperature structure if the atmosphere is hot or thin. Our models let us map out atmospheric scenarios for planets such as GJ 1132b and show how thermal phase curves could constrain them. Measuring phase curves of short-period planets will require similar amounts of time on the *James Webb Space Telescope* as detecting molecules via transit spectroscopy, so future observations should pursue both techniques.

3.1 Introduction

3.1.1 Importance of atmospheric dynamics

Terrestrial exoplanets orbiting M-dwarfs are extremely common. Results from the *Kepler* space telescope show that there are at least ~ 0.5 rocky planets per M-dwarf, half of which could even be habitable (Dressing & Charbonneau, 2015). Just as important, near-future telescopes like the *James Webb Space Telescope* (*JWST*) will be able to characterize the atmospheres of these planets (Deming et al., 2009; Beichman et al., 2014; Cowan et al., 2015), making them one of the most promising observational targets of the coming decade.

New theories are needed to understand the potential atmospheres of these exoplanets, particularly their temperature structures and large-scale circulations. An atmosphere's temperature structure and circulation critically influence a planet's surface and atmospheric evolution as well as its potential habitability (Kasting, 1988; Abe et al., 2011; Yang et al., 2013). An atmosphere's temperature structure and circulation are also important for interpreting observations. For example, a planet's emission spectrum is determined by the vertical temperature distribution of its atmosphere, while the planet's thermal and optical phase curves are set by its day-night temperature gradient and cloud patterns (Seager & Deming, 2009; Yang et al., 2013; Hu et al., 2015). Even transit measurements can be strongly influenced by chemical mixing and clouds, which in turn depend on the atmosphere's large-scale circulation (Fortney, 2005; Parmentier et al., 2013; Charnay et al., 2015; Line & Parmentier, 2016).

Unfortunately there is a large gap between current theories of terrestrial atmospheres and the wide range of potential exoplanets. Planets accessible to follow-up observations will generally be in short-period orbits, experience strong tidal forces, and thus tend to be either tidally locked or captured in higher spin-orbit resonances (Kasting et al., 1993; Makarov et al., 2012). The solar system offers no direct analogs of such atmospheres, and their dynamics are still poorly understood. In this work we focus on tidally locked (synchronously rotating) atmospheres because their dynamics would differ most drastically from rapidly rotating atmospheres, whereas planets in higher spin-orbit resonances should resemble hybrids between tidally locked and rapidly rotating planets (also see Section 3.9).

3.1.2 Previous work and open questions

Many groups have already used general circulation models (GCMs) to study the thermal structure and atmospheric circulation of tidally locked terrestrial planets (e.g., Joshi et al., 1997; Merlis & Schneider, 2010; Heng et al., 2011b; Pierrehumbert, 2011a; Selsis et al., 2011; Leconte et al., 2013; Yang et al., 2013; Zalucha et al., 2013; Wordsworth, 2015; Kopparapu et al., 2016). These studies investigated a range of processes that shape the atmospheres of tidally locked planets, including the large-scale day-night circulation, equatorial superrotation, heat transport by atmospheric waves, and the potential for atmospheric collapse if the nightside becomes too cold. The development of theory to understand these processes, however, has not kept up with the rapid proliferation of simulations.

Recent theories of rocky planets focused on planets for which the horizontal heat redistribution is extremely efficient (Pierrehumbert, 2011a; Mills & Abbot, 2013; Yang & Abbot, 2014; Wordsworth, 2015). Among the latter, Pierrehumbert (2011b) developed a scaling relation for the surface temperature of a planet that is horizontally completely uniform and whose atmosphere is optically thick,

$$T_s \quad = T_{eq} \times \frac{\tau_{LW}^{\beta}}{\Gamma\left(1+4\beta\right)^{1/4}}. \tag{3.1}$$

Here T_{eq} is the planet's equilibrium temperature defined as $T_{eq} \equiv [L_*(1-\alpha)/(4\sigma)]^{1/4}$, τ_{LW} is the longwave optical thickness, Γ is the Gamma function defined as $\Gamma(a) \equiv \int_0^\infty t^{a-1}\exp(-t)dt$, and $\beta \equiv R/(c_p n)$. L_* is the stellar constant, α is the planetary bond albedo, σ is the Stefan-Boltzmann constant, R is the specific gas constant, c_p is the specific heat capacity, and n governs how optical thickness depends on pressure (Section 3.2). Similarly, Wordsworth (2015) developed a theory for the temperature structure of tidally locked atmospheres in the optically thin limit, in which atmospheres become particularly vulnerable to atmospheric collapse. Wordsworth (2015) found a lower bound for the nightside temperature of a tidally locked planet[1],

$$T_n \quad = T_{eq} \left(\frac{\tau_{LW}}{2} \right)^{1/4}. \tag{3.2}$$

Common to both scalings is that they are not valid in the physically important regime of optical depth unity, and indeed contradict each other when extrapolated to this limit. Neither do they explicitly account for horizontal atmospheric dynamics[2]. Nevertheless, we expect that the dynamics of tidally locked planets should be sensitive to a range of additional processes, including the atmosphere's radiative timescale, surface drag, and planetary rotation, all of which have not yet been addressed for rocky exoplanets.

On a different front, recent work has begun to understand the atmospheric circulation of hot Jupiters (Perez-Becker & Showman, 2013; Showman et al., 2015; Komacek & Showman, 2016). Perez-Becker & Showman (2013) developed a weak-temperature-gradient (WTG) theory that explains why the hottest hot Jupiters also tend to have the highest day-night brightness temperature contrasts. WTG describes atmospheres that are slowly rotating and are relatively cool, which allows atmospheric waves to efficiently eliminate horizontal temperature gradients (Showman et al., 2013). In equilibrium the wave adjustment leads to subsidence, that is, sinking motions, in regions of radiative cooling (see Section 3.5). Perez-Becker & Showman (2013) showed that day-night temperature gradients become large once the radiative timescale becomes shorter than the timescale for subsidence, $t_{rad} \lesssim t_{sub}$. On

---

[1] We use Equation 3.2 instead of Equation (29) in Wordsworth (2015), because it does not assume a specific value for n.

[2] Wordsworth (2015) also developed a model that incorporates dynamics, which we revisit in Section 3.4.

hot Jupiters with sufficiently strong drag, temperature gradients are large when

$$t_{rad} \lesssim \frac{t_{wave}}{t_{drag}} \times t_{wave}, \tag{3.3}$$

where t_{wave} is the timescale for a gravity wave to horizontally propagate across the planet and t_{drag} is a characteristic drag timescale.

It would be tempting to assume Equation 3.3 applies equally well to rocky exoplanets. That is not the case, and published GCM results of rocky planets are already at odds with it. We show in Appendix E that for most tidally locked terrestrial planets drag and wave timescales are comparable, $t_{drag} \approx t_{wave}$. If Equation 3.3 applied to rocky planets, they should develop large day-night temperature gradients when

$$1 \lesssim \frac{t_{wave}}{t_{rad}}. \tag{3.4}$$

In contrast, the GCM simulations in Selsis et al. (2011) indicate that tidally locked rocky planets can develop atmospheric temperature gradients at a surface pressure of about 1 bar (their Fig. 5), which translates to a much lower value of $t_{wave}/t_{rad} \sim 0.05$. Similarly, we found in Koll & Abbot (2015) that rocky exoplanets develop large day-night brightness temperature contrasts when $t_{wave}/t_{rad} \gtrsim 10^{-2}$. The disagreement between hot Jupiter theory and rocky planets has not been explored yet. Here we will show that the qualitative threshold for a WTG atmosphere to develop large temperature gradients, $t_{rad} \lesssim t_{sub}$, also applies to rocky planets. However, rocky planets end up behaving quite differently than hot Jupiters because of the processes that determine the large-scale circulation and the subsidence timescale t_{sub}.

3.1.3 Outline

In this paper we develop a series of models to understand the atmospheres of tidally locked rocky exoplanets. To show how our models complement previous theories we adopt our nondimensional analysis from Koll & Abbot (2015). Using the Buckingham-Pi theorem (Buckingham, 1914), we showed that the dynamics of a dry and tidally locked atmosphere with grey radiation are governed by only six nondimensional parameters. This set of nondimensional parameters allows us to cleanly disentangle the atmospheric processes that need to be addressed. One choice for the six parameters is given by

$$\left(\frac{R}{c_p}, \frac{a^2}{L_{Ro}^2}, \frac{t_{wave}}{t_{rad}}, \tau_{SW}, \tau_{LW}, \frac{t_{wave}}{t_{drag}}\right). \tag{3.5}$$

The convective lapse rate is controlled by R/c_p. The nondimensional Rossby radius a^2/L_{Ro}^2 governs the influence of planetary rotation on equatorial waves. Here a is the planetary radius, the equatorial Rossby deformation radius is defined as $L_{Ro} \equiv \sqrt{a c_{wave}/(2\Omega)}$, Ω is the planetary rotation rate, and c_{wave} is the speed of a gravity wave. Although c_{wave} is a priori unknown, because it depends on an atmosphere's vertical temperature structure, we can place a reasonable upper bound on it by assuming an isothermal atmosphere. This assumption leads to $c_{wave} = \sqrt{R/c_p} \times \sqrt{gH} = \sqrt{R/c_p} \times \sqrt{RT_{eq}}$, where g is the acceleration of gravity and $H \equiv RT_{eq}/g$ is the scale height. The wave-to-radiative timescale ratio, t_{wave}/t_{rad}, compares the time it takes for equatorial waves to redistribute energy across the planet, $t_{wave} \equiv a/c_{wave}$, to the atmosphere's radiative cooling time, $t_{rad} \equiv c_p p_s/(g\sigma T_{eq}^3)$. The atmospheric shortwave and longwave optical thicknesses are τ_{SW} and τ_{LW}. The ratio of wave to drag timescales $t_{wave}/t_{drag} = C_D a/H$ governs surface friction and turbulent heat fluxes (Appendix E).

We only consider atmospheres that are transparent to shortwave absorption ($\tau_{SW} = 0$), which ensures that the solid surface substantially affects the atmospheric dynamics. This means we exclude from our consideration potential "rocky" planet scenarios with a bulk silicate composition, but with gaseous envelopes several hundreds of bar thick (Owen & Mohanty, 2016). We expect that the observable atmospheres of such planets would resemble gas giants more than rocky planets, with dynamics that are better captured by theories developed for hot Jupiters (Perez-Becker & Showman, 2013; Showman et al., 2015; Komacek & Showman, 2016).

Of the six nondimensional parameters τ_{SW} and τ_{LW} govern radiative transfer, R/c_p sets the vertical temperature structure, and the remaining three parameters determine the horizontal dynamics. As an important starting point, we formulate an analytical radiative-convective (RC) model for the temperature structure of tidally locked atmospheres that only depends on $\beta \equiv R/(nc_p)$ and τ_{LW} and therefore addresses the first two processes (Section 3.3). In the optically thick regime this model reduces to the asymptotic limit found by Pierrehumbert (2011b). We then turn to horizontal dynamics. We show the day-night circulation acts as a heat engine, in which heating and cooling balance frictional dissipation in the dayside boundary layer (Section 3.4). We use our heat engine theory to develop a radiative-convective-subsiding (RCS) model that includes the effects of t_{wave}/t_{drag} and t_{wave}/t_{rad} on temperature structure (Section 3.5). For cool/thick atmospheres the RCS model reduces to the RC model, whereas for optically thin and hot/thin atmospheres it reduces to the asymptotic limit found by Wordsworth (2015). Our RCS model explains why rocky planets develop large day-night temperature gradients at a significantly lower t_{wave}/t_{rad} threshold than hot Jupiters (Section 3.6). Next, we use GCM simulations to address rapidly rotating planets and a^2/L_{Ro}^2 (Section 3.7). We find that t_{wave}/t_{rad} has to be big for rotation to have a strong effect on temperature structure, that is, cause large eastward hot spot offsets or cold nightside vortices. Our results imply that planets like GJ 1132b or HD 219134b will likely have significant day-night temperature contrasts, unless their atmospheres are dominated by H_2 (Section 3.8). We estimate that detecting these potential contrasts via thermal phase curves will require about as much time with *JWST* as detecting molecular signatures via transit spectroscopy. Finally, we discuss and summarize our results in Sections 3.9 and 3.10.

3.2 Methods

We compare our models with a large number of GCM simulations. We use the FMS GCM with two-band grey gas radiative transfer and dry (non-condensing) thermodynamics. FMS has been used to simulate the atmospheres of Earth (Frierson et al., 2006), Jupiter (Liu & Schneider, 2011), hot Jupiters (Heng et al., 2011b), tidally locked terrestrial planets (Merlis & Schneider, 2010; Mills & Abbot, 2013; Koll & Abbot, 2015), and non-synchronously rotating terrestrial planets (Kaspi & Showman, 2015). We use the same FMS configuration as Koll & Abbot (2015). The model version we use simulates the full atmospheric dynamics and semi-grey (shortwave and longwave) radiation, and we include instantaneous dry convective adjustment. Drag is parametrized using a standard Monin-Obukhov scheme which self-consistently computes the depth of the planetary boundary layer as well as turbulent diffusion of heat and momentum. The surface is represented by an idealized "slab layer", that is a single layer with uniform temperature and fixed depth. The "slab" temperature can be interpreted as a temperature average across the surface's thermal skin depth (Pierrehumbert, 2011b). Our simulations are all tidally locked and orbits are assumed to be circular so that the stellar flux is constant in time.

Because we only consider atmospheres that are transparent to shortwave radiation ($\tau_{SW} = 0$), the incoming stellar flux and the planetary albedo are degenerate in their effect on planetary temperature. For simplicity we set the surface albedo to zero in all our simulations and vary the incoming stellar flux. To specify the relation between longwave optical thickness and pressure, we use a standard power law of the form

$$\frac{\tau}{\tau_{LW}} = \left(\frac{p}{p_s}\right)^n . \tag{3.6}$$

The exponent n specifies how the optical thickness τ increases with pressure. For example, $n = 1$ if the opacity of a gas mixture is independent of pressure, and $n = 2$ if the opacity increases due to pressure broadening (Pierrehumbert, 2011b; Robinson & Catling, 2012).

Parameter	Symbol	Unit	Min. value	Max. value
Planetary radius	a	$a_{\oplus}$	0.5	2
Rotation rate	Ω	days^{-1}	$2\pi/100$	$2\pi/1$
Equilibrium temperature	T_{eq}	K	250	600
Surface gravity	g	10 m s^{-2}	$\frac{2}{5} \times (a/a_{\oplus})$	$\frac{5}{2} \times (a/a_{\oplus})$
Specific heat capacity[a]	c_p	$\text{J kg}^{-1} \text{ K}^{-1}$	820	14518
Specific gas constant[a]	R	$\text{J kg}^{-1} \text{ K}^{-1}$	189	4158
Surface pressure	p_s	bar	10^{-2}	10
Longwave optical thickness[b]	τ_{LW}	-	0.1	100
Surface drag coefficient	C_D, via k_{vk}	-	×0.1	×10

[a] Minimum values correspond to CO_2, maximum values correspond to H_2.

[b] The optical thickness is defined at 1 bar.

Table 3.1: Parameter bounds for our simulations. The shortwave optical thickness is set to zero, $\tau_{SW} = 0$. C_D is not a fixed parameter, so we vary the von Karman constant k_{vk} to increase and decrease C_D by an order of magnitude (Appendix E). We vary R and c_p, but require that R/c_p stays within the range of diatomic and triatomic gases ($0.23 \leqslant R/c_p \leqslant 0.29$).

Our GCM results assume $n = 2$ or $n = 1$. The longwave optical thickness τ_{LW} is set independently of the atmosphere's bulk composition. To constrain τ_{LW} we note that more complex radiative transfer calculations tend to find values of τ_{LW} beween ~1 and ~10 at ~1 bar across a wide range of atmospheres, (Robinson & Catling, 2014; Wordsworth, 2015). We extend these bounds by one order of magnitude in each direction and require that the optical thickness at 1 bar satisfy $0.1 \leqslant \tau_{LW,\text{1bar}} \leqslant 100$. The parameter bounds for our simulations are summarized in Table 3.1.

Figure 3.1a shows the temperature structure of a representative, slowly rotating and relatively cool, GCM simulation. The planet is Earth-sized ($a = a_{\oplus}$), temperate ($T_{eq} = 283$K), has an orbital period and rotation rate of 50 days, has a moderately thick N_2-dominated atmosphere ($p_s = 1$ bar), and a longwave optical depth of unity ($\tau_{LW} = 1$). The GCM does not explicitly model a host star, but the orbital period and equilibrium temperature correspond to an early M-dwarf (M0 or M1; Kaltenegger & Traub, 2009, Table 1). In terms of nondimensional parameters, $(R/c_p, a^2/L_{Ro}^2, t_{wave}/t_{rad}, \tau_{LW}, t_{wave}/t_{drag}) = (2/7, 0.12, 5\times10^{-3}, 1, 1.4)$. Because the temperature structure is approximately symmetric about the substellar point

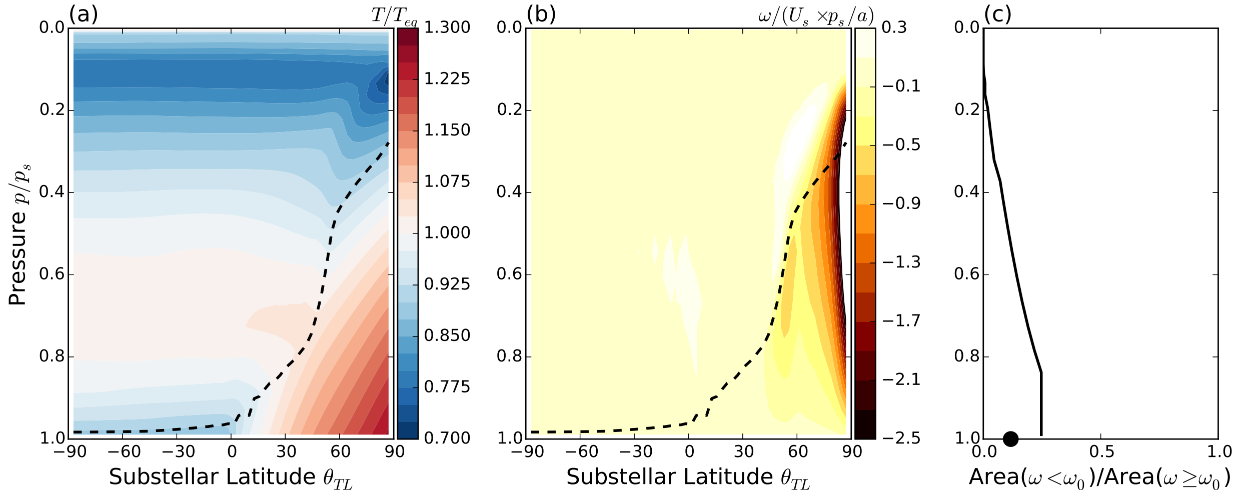

Figure 3.1: Temperature and circulation structure of a representative slowly rotating and weakly forced GCM simulation with $(a^2/L_{Ro}^2, t_{wave}/t_{rad}) = (0.12, 5 \times 10^{-3})$. (a) Temperature as a function of substellar latitude (=0° at the terminator, =90° at the substellar point). (b) Vertical velocity in pressure coordinates as a function of substellar latitude. (c) Area fraction of rising motion, where the dot shows the vertically averaged area fraction. The dashed black line in (a,b) shows the top of the GCM's boundary layer. Inside the boundary layer temperature increases towards the substellar point, and air rises; outside the boundary layer temperature contours are flat and air sinks. The region of rapidly rising motions, $\omega < 0.01 \times min(\omega)$, is narrowly focused on the substellar point while most of the atmosphere experiences weak subsidence, $\omega \gtrsim 0$. We normalize temperature by the equilibrium temperature T_{eq}, and pressure velocity by the characteristic surface speed from the heat engine $U_s \times p_s/a$ (Section 3.4). The planet's physical parameters are $T_{eq} = 283\text{K}, a = a_{\oplus}, \Omega = 2\pi/(50\text{d}), p_s = 1\text{bar}, \tau_{LW} = 1$, and $(R, c_p) = (R, c_p)_{N_2}$.

we present this simulation in terms of a substellar latitude, i.e., the angle between substellar and antistellar point (also see Koll & Abbot, 2015, Appendix B). The temperature structure in Figure 3.1a is comparable to that found by previous studies, and temperature contours are horizontally flat outside the dayside boundary layer (dashed black line). The flat temperature contours are characteristic of the weak-temperature-gradient (WTG) regime. However, WTG does not hold on large parts of the dayside where the absorbed stellar flux creates a region of strong convection and turbulent drag, which damps atmospheric waves and allows the atmosphere to sustain horizontal temperature gradients (Showman et al., 2013). As noted by Wordsworth (2015), this boundary layer will be of critical importance for understanding the atmospheric circulation of rocky planets.

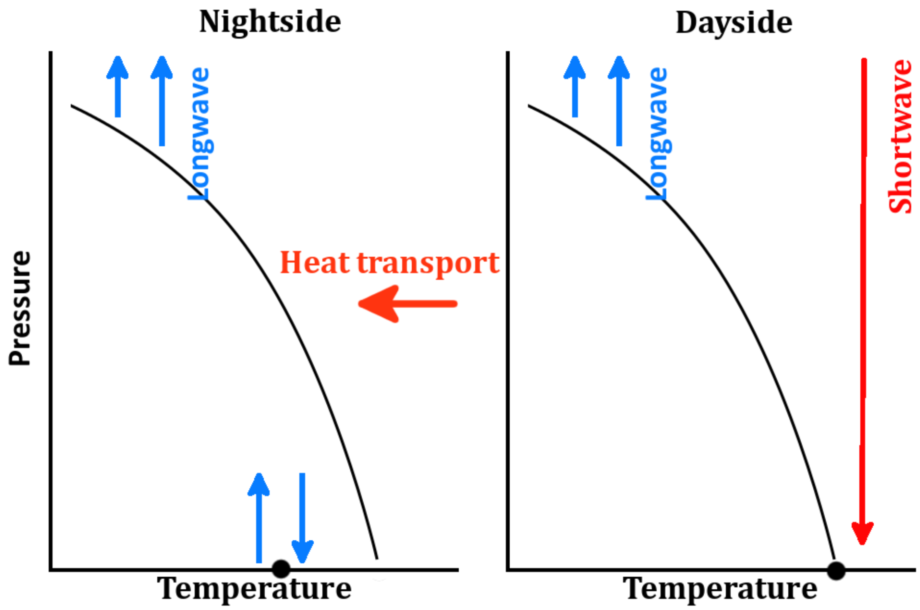

Figure 3.2: The two-column radiative-convective model. We assume convection on the dayside sets up an adiabatic temperature profile. Horizontal heat transport is assumed to be effective so that the atmosphere is horizontally uniform. The black dots indicate surface temperatures. The dayside surface and atmosphere are closely coupled via convection, whereas the nightside surface is in radiative equilibrium with, and generally colder than, the overlying atmosphere.

3.3 A two-column radiative-convective model

In this section we present a two-column model for tidally locked planets. We divide the planet into two (dayside and nightside) vertical columns, as shown in Figure 3.2. The dayside is heated by stellar radiation, which triggers convection and sets an adiabatic vertical temperature profile. We assume the convective heat flux is large so that the temperature jump between dayside surface and lowest atmospheric level is small. We also assume convection is deep and do not include a stratosphere (i.e., a purely radiative layer in the upper atmosphere), so that the dayside column temperature profile in terms of optical thickness τ

can be written as

$$T = T_d \left(\frac{\tau}{\tau_{LW}}\right)^{\beta}, \tag{3.7}$$

where T_d is the dayside surface temperature, τ_{LW} is the total optical thickness in the longwave, and $\beta \equiv R/(c_p n)$ is the adiabatic lapse rate in optical thickness coordinates. Next, we assume the weak-temperature-gradient (WTG) regime holds globally (i.e., also inside the dayside boundary layer). The atmosphere is therefore horizontally homogeneous and the nightside temperature structure is also described by Equation 3.7. Under these assumptions the entire atmosphere is in radiative-convective equilibrium, with convection governed by the dayside surface temperature T_d. The nightside surface will generally be colder than the overlying air, which leads to stable stratification and suppresses turbulent fluxes between the nightside surface and atmosphere. We idealize this situation by assuming that the nightside surface is in radiative equilibrium with the overlying atmosphere (see Fig. 3.2).

For a grey atmosphere on a dry adiabat, the top-of-atmosphere (TOA) upward longwave and surface downward longwave fluxes are (Pierrehumbert, 2011b; Robinson & Catling, 2012)

$$\begin{aligned} F^{\uparrow}(\tau = 0) &= \sigma T_d^4 e^{-\tau_{LW}} + \sigma T_d^4 \int_0^{\tau_{LW}} \left(\frac{\tau'}{\tau_{LW}}\right)^{4\beta} e^{-\tau'} d\tau', & \text{(3.8a)} \\ F^{\downarrow}(\tau = \tau_{LW}) &= \sigma T_d^4 \int_0^{\tau_{LW}} \left(\frac{\tau'}{\tau_{LW}}\right)^{4\beta} e^{-(\tau' - \tau_{LW})} d\tau'. & \text{(3.8b)} \end{aligned}$$

Using these expressions we write the dayside TOA, nightside TOA, and nightside surface energy budgets[3] as

$$\begin{aligned}
\frac{L_*(1-\alpha_p)}{2} &= \sigma T_d^4 e^{-\tau_{LW}} + \sigma T_d^4 \int_0^{\tau_{LW}} \left(\frac{\tau'}{\tau_{LW}}\right)^{4\beta} e^{-\tau'} d\tau' + HT, && \text{(3.9a)}\\
HT &= \sigma T_n^4 e^{-\tau_{LW}} + \sigma T_d^4 \int_0^{\tau_{LW}} \left(\frac{\tau'}{\tau_{LW}}\right)^{4\beta} e^{-\tau'} d\tau', && \text{(3.9b)}\\
0 &= \sigma T_n^4 - \sigma T_d^4 \int_0^{\tau_{LW}} \left(\frac{\tau'}{\tau_{LW}}\right)^{4\beta} e^{-(\tau_{LW}-\tau')} d\tau', && \text{(3.9c)}
\end{aligned}$$

where T_d is the dayside temperature, T_n is the nightside temperature, and HT is the day-night heat transport. We express the stellar flux in terms of the equilibrium temperature, $L_*(1-\alpha_p)/2 = 2\sigma T_{eq}^4$. Next, we combine the TOA equations to eliminate HT and use the nightside surface budget to write T_n in terms of T_d. We find

$$\begin{aligned}
\sigma T_d^4 &= \frac{2\sigma T_{eq}^4}{2\int_0^{\tau_{LW}} \left(\frac{\tau'}{\tau_{LW}}\right)^{4\beta} e^{-\tau'} d\tau' + e^{-\tau_{LW}} \left[1 + \int_0^{\tau_{LW}} \left(\frac{\tau'}{\tau_{LW}}\right)^{4\beta} e^{-(\tau_{LW}-\tau')} d\tau'\right]} && \text{(3.10a)}\\
\sigma T_n^4 &= \frac{2\sigma T_{eq}^4 \times \int_0^{\tau_{LW}} \left(\frac{\tau'}{\tau_{LW}}\right)^{4\beta} e^{-(\tau_{LW}-\tau')} d\tau'}{2\int_0^{\tau_{LW}} \left(\frac{\tau'}{\tau_{LW}}\right)^{4\beta} e^{-\tau'} d\tau' + e^{-\tau_{LW}} \left[1 + \int_0^{\tau_{LW}} \left(\frac{\tau'}{\tau_{LW}}\right)^{4\beta} e^{-(\tau_{LW}-\tau')} d\tau'\right]} && \text{(3.10b)}
\end{aligned}$$

The first term in the denominator is the atmosphere's contribution to the TOA flux, the second term is the TOA flux contribution from the dayside and nightside surfaces. In practice we evaluate the definite integrals in these expressions numerically, but they can also be expressed in terms of gamma functions (Robinson & Catling, 2012).

In the optically thick limit, these expressions reduce to the result of Pierrehumbert (2011b). For $\tau_{LW} \gg 1$ the exponential terms $e^{-\tau_{LW}}$ become negligibly small. The integrand in the upward flux decays exponentially at large τ', which means we can approximate the upper limit as infinity and replace the integral with a gamma function, $\tau_{LW}^{-4\beta} \int_0^{\tau_{LW}} \tau'^{4\beta} e^{-\tau'} d\tau' \approx \tau_{LW}^{-4\beta} \int_0^{\infty} \tau'^{4\beta} e^{-\tau'} d\tau' = \tau_{LW}^{-4\beta} \Gamma(1+4\beta)$. Similarly, in the optically thick limit the downward

---

[3] We implicitly use the dayside surface energy budget by assuming that the surface-air temperature jump is negligible on the dayside.

flux at the surface has to approach unity, $\int_0^{\tau_{LW}} (\tau'/\tau_{LW})^{4\beta} e^{-(\tau_{LW}-\tau')} d\tau' \approx 1$. Combining these approximations we find $T_n \approx T_d \approx T_{eq}\tau_{LW}^{\beta}\Gamma(1+4\beta)^{-1/4}$, which is the same as Pierrehumbert's result (Equation 3.1). The dayside and nightside temperatures become equal in this limit because the atmosphere's downward longwave emission becomes large enough to eliminate the temperature difference between the nightside surface and the air directly above it (which in turn is equal to the dayside surface temperature).

In the optically thin limit, our model differs slightly from the result of Wordsworth (2015). For $\tau_{LW} \ll 1$ we can approximate all exponentials using Taylor series, $e^{-\tau_{LW}} = 1 + \mathcal{O}(\tau_{LW})$. Retaining only the lowest order in τ_{LW}, we write the integrals in the upward and downward fluxes both as $\tau_{LW}^{-4\beta} \int_0^{\tau_{LW}} \tau'^{4\beta} e^{\pm\tau'} d\tau' \approx \tau_{LW}^{-4\beta} \int_0^{\tau_{LW}} \tau'^{4\beta} d\tau' = \tau_{LW}/(1+4\beta)$. The atmosphere's TOA upward and surface downward emission therefore become equal, which is a well-known property of grey radiation in the optically thin limit (Pierrehumbert, 2011b). Again discarding higher-order terms in τ_{LW}, we find $T_d \approx 2^{1/4} T_{eq} \times [1 - 3\tau_{LW}/(4(1+4\beta))]$ and $T_n \approx 2^{1/4} T_{eq} \tau_{LW}^{1/4} \times (1+4\beta)^{-1/4}$. This nightside temperature has the same asymptotic limit but is slightly warmer than Equation 3.2 from Wordsworth (2015). That is because we assume the atmosphere remains fixed to an adiabat, whereas Wordsworth (2015) assumes an atmosphere that is vertically isothermal. We will use our radiative-convective-subsiding model (Sections 3.5-3.6) to show that Wordsworth's result is a limiting expression for atmospheres that are very hot or thin, $t_{wave}/t_{rad} \gtrsim 1$, whereas our results in this Section apply for atmospheres that are cold or thick, $t_{wave}/t_{rad} \lesssim 10^{-4}$. Nevertheless, β is always of order unity so the difference between Equation 3.2 and our result is small in the optically thin regime.

Next, we compare the previous scalings and our radiative-convective (RC) model with our GCM simulations. Figure 3.3 shows dayside (top) and nightside (bottom) average surface temperatures of many simulations. To represent all GCM results in a single figure, we normalize surface temperatures using the equilibrium temperature T_{eq} of each simulation. We only show simulations with $\beta = 1/7$, i.e., $(R, c_p, n) = (R_{N_2}, c_{p,N_2}, 2)$. First, as we showed

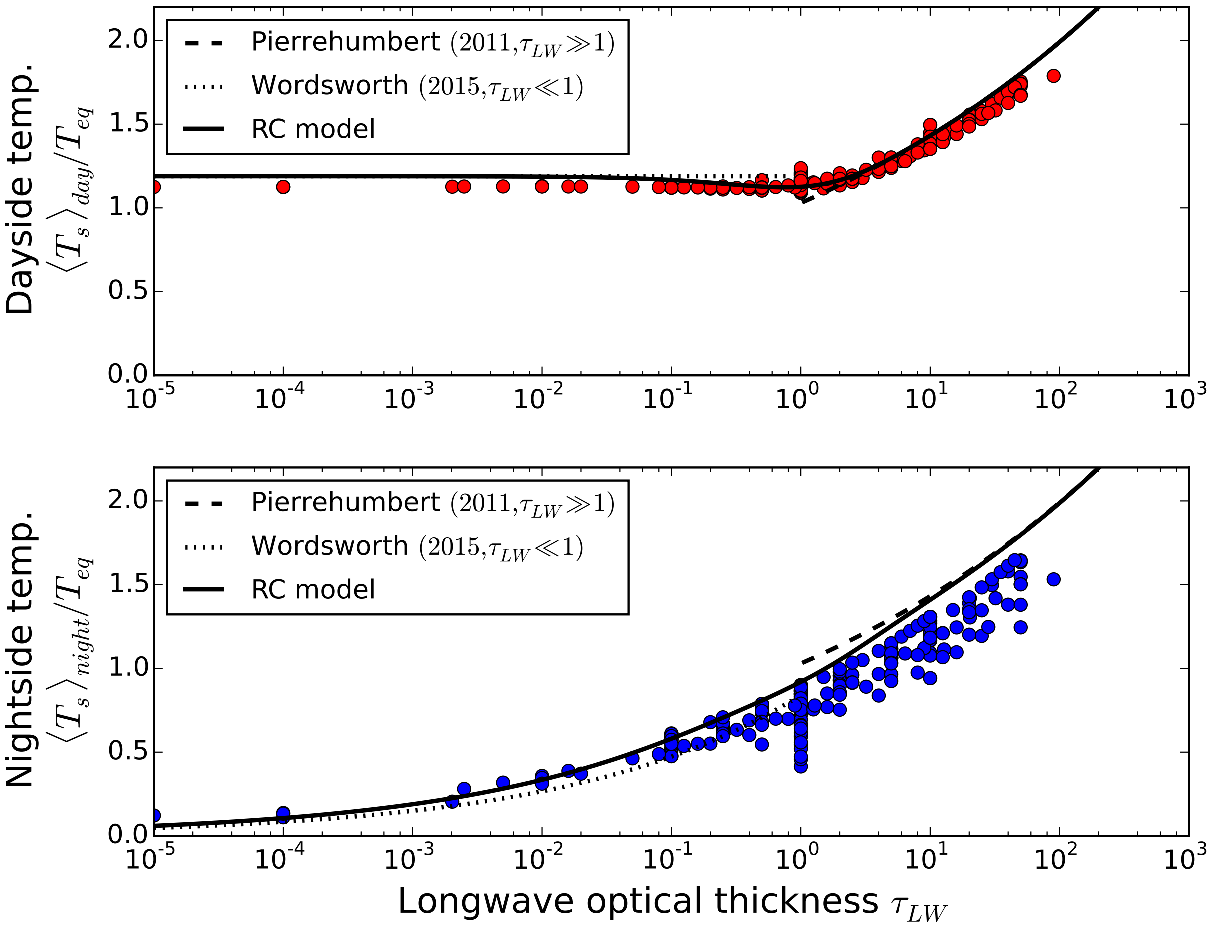

Figure 3.3: Our radiative-convective (RC) model captures the basic dependency of surface temperature on τ_{LW} and joins previous asymptotic limits. Top: Average dayside surface temperatures of many GCM simulations ($N = 251$). Bottom: Average nightside surface temperatures. Dashed and dotted curves show previously-derived asymptotic scalings in the optically thick ($\tau_{LW} \gg 1$, Pierrehumbert, 2011b) and optically thin limits ($\tau_{LW} \ll 1$, Wordsworth, 2015). The solid curve shows the RC model (Section 3.3). While the RC model closely matches the GCM dayside temperatures, it does not account for the wide spread in nightside temperatures. All shown simulations use $n = 2$ and $(R, c_p) = (R, c_p)_{N_2}$.

above, the RC model tends towards the expressions of Pierrehumbert and Wordsworth in the optically thick and thin regimes (compare solid line with dashed and dotted lines). While the two approximate expressions diverge at $\tau_{LW} = 1$, our model provides a smooth fit in this region. Second, the RC model captures dayside surface temperatures very well, with deviations beween the RC model and the GCM simulations smaller than $0.1 \times T_{eq}$. The RC model systematically overpredicts dayside temperatures because of its idealized geometry,

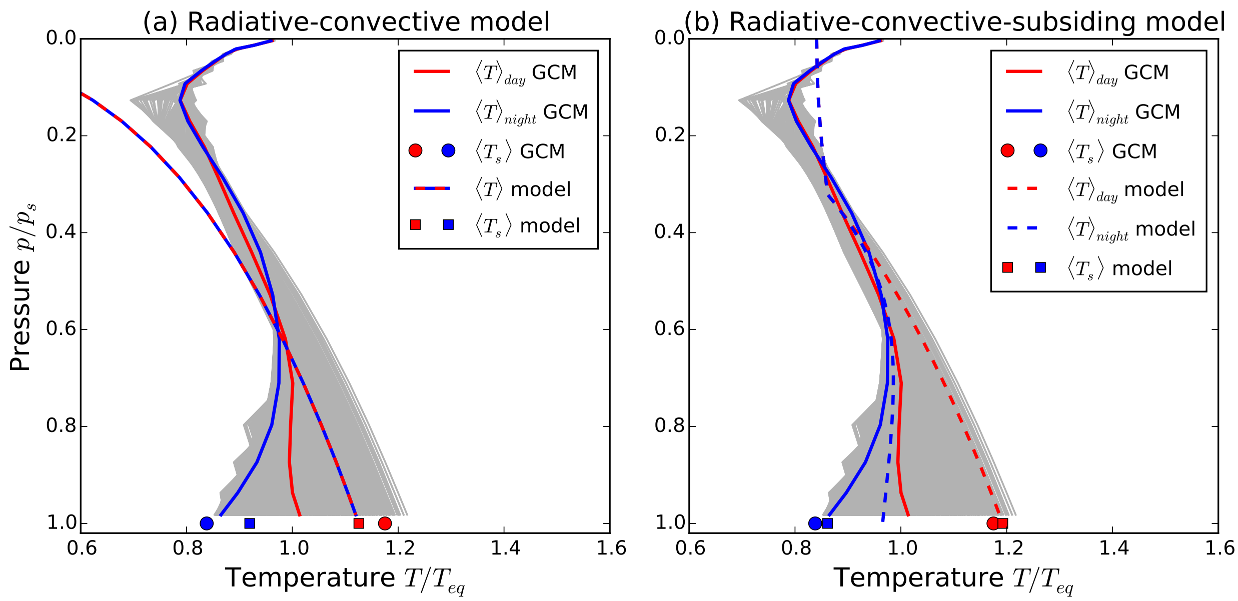

Figure 3.4: Temperature structure of a slowly rotating GCM simulation ($a^2/L_{Ro}^2 = 0.1$), compared with the radiative-convective (RC, left) and the radiative-convective-subsiding model (RCS, right). Solid curves correspond to dayside (red) and nightside-averaged (blue) GCM temperature profiles, and GCM temperature profiles at each latitude and longitude (grey). Left: Although the RC model (mixed red-blue curve) qualitatively captures the temperature structure, it does not capture the nightside inversion and thus overpredicts the nightside surface temperature (compare blue square with blue circle). Right: the RCS model (dashed curves) accounts for imperfect day-night heat transport and qualitatively captures the nightside inversion structure. This leads to a better fit of nightside surface temperature than for the RC model. The planet's physical parameters are $T_{eq} = 400\text{K}, a = a_\oplus, \Omega = 2\pi/(50\text{d}), p_s = 0.5\text{bar}, \tau_{LW} = 1, (R, c_p) = (R, c_p)_{N_2}$, and $g = 5\text{m s}^{-2}$.

which represents the entire dayside as a single column. For example, the dayside-average temperature of an airless planet in pure radiative equilibrium is $4\sqrt{2}/5 \times T_{eq} \approx 1.13T_{eq}$, whereas the RC model predicts $2^{1/4} \times T_{eq} \approx 1.19T_{eq}$. Third, the RC model captures the general trend of nightside surface temperature with τ_{LW}. However, Figure 3.3 also shows that nightside temperatures exhibit a much wider spread than dayside temperatures, which is not captured by the RC model.

There are two reasons for the spread in nightside temperatures: first, rapidly rotating atmospheres develop horizontally inhomogeneous nightsides, and second, tidally locked atmospheres do not have an adiabatic temperature structure on the nightside. We address rotation in Section 3.7, here we consider the effect of temperature structure. Figure 3.4a shows the vertical temperature structure of a slowly rotating simulation. The grey lines show the vertical temperature profiles at each horizontal GCM grid point, which form a wide envelope. The hottest temperatures at the right side of the envelope correspond to the substellar point. These profiles are indeed adiabatic, which can be seen from the fact that they are parallel to the temperature profile of the RC model (dashed red-blue line). However, as the dayside and nightside averaged profiles show, large parts of the atmosphere do not follow an adiabat (solid red and blue lines in Fig. 3.4a). The deviation arises because WTG breaks down inside the dayside boundary layer (Fig. 3.1a). This allows the atmosphere outside the boundary layer to decouple from regions of convection, and develop a strongly non-adiabatic temperature profile. In particular, Figure 3.4 shows that the nightside average (blue line) forms a strong inversion below $p/p_s \sim 0.6$, which means the nightside is stably stratified and far from radiative-convective equilibrium. Nightside inversions are a robust feature of tidally locked atmospheres and have been found in a range of simulations (e.g., Joshi et al., 1997; Merlis & Schneider, 2010; Leconte et al., 2013), but are not captured by the RC model. As a consequence the RC model produces a warmer nightside atmosphere and therefore also a warmer nightside surface than the GCM (compare blue square and blue circle in Fig. 3.4a). We present a model that captures the nightside temperature structure in Section 3.5. However, to do so we have to account for atmospheric dynamics, which show up via the parameters t_{wave}/t_{rad} and t_{wave}/t_{drag}. To address the dynamics we first have to develop a theory of large-scale wind speeds and the atmospheric circulation, which we turn to in the next section.

3.4 A heat engine scaling for wind speeds

Earth's atmosphere acts as a heat engine: it absorbs heat near the surface at a high temperature and emits heat to space at a low temperature, which allows the atmosphere to do work and balance frictional dissipation (Peixoto & Oort, 1984). On Earth the heat engine framework has been used to derive upper bounds on the strength of tropical moist convec-

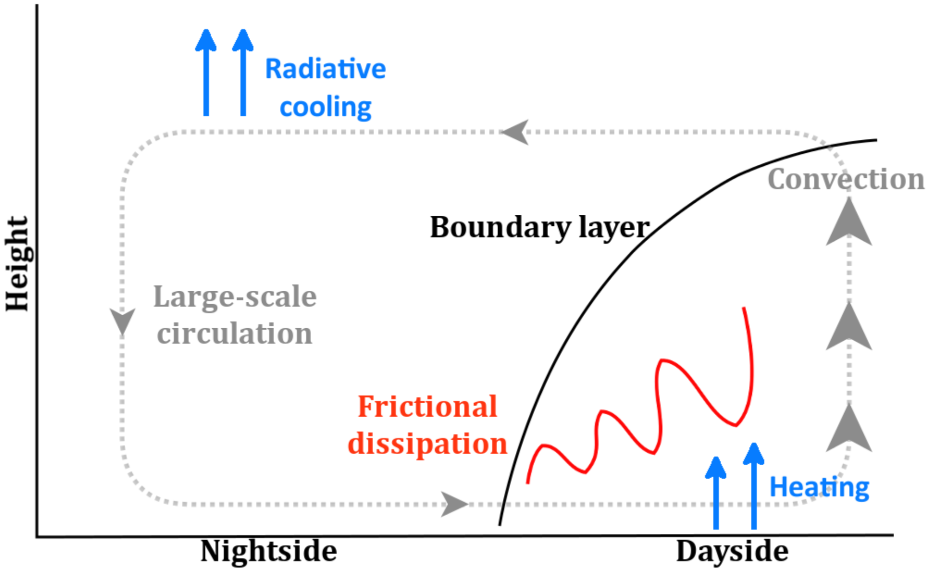

Figure 3.5: A diagram of the atmospheric heat engine. The heat engine is driven by dayside heating and cooling to space. Frictional dissipation in the dayside boundary layer limits the strength of the resulting day-night atmospheric circulation.

tion (Renno & Ingersoll, 1996; Emanuel & Bister, 1996) and small-scale circulations such as hurricanes (Emanuel, 1986).

In this section we idealize the atmospheric circulation of a tidally locked planet as a single overturning cell between the substellar and antistellar point. We model the circulation as an ideal heat engine to place an upper bound on its circulation strength. The ideal heat engine is an upper bound because additional physical processes, such as diffusion, lead to irreversible production of entropy and decrease the efficiency of a heat engine below its ideal limit (Pauluis & Held, 2002). As shown in Figure 3.5, the atmosphere absorbs heat near the dayside surface at a hot temperature and emits it to space at a cold temperature. These temperatures are defined in terms of entropy-weighted averages over which the atmosphere absorbs and gives off heat (Emanuel & Rotunno, 1989; Pauluis & Held, 2002). Here we idealize the dayside as a single column that follows an adiabat. Entropy is therefore vertically constant on the dayside, which means the temperature at which the atmosphere absorbs heat is equal to the dayside surface temperature, T_d. We approximate the cold temperature as the planet's effective emission temperature to space, i.e., its equilibrium temperature T_{eq}. The parcel does work against friction in the boundary layer which is given by $W = C_D \rho_s U_s^3$ (Bister & Emanuel, 1998). Here W is the work, ρ_s is the surface density, and U_s is a surface wind speed, which we take to be the dayside-average surface wind (Fig. 3.5). Using Carnot's theorem,

$$W = \eta Q_{in}, \tag{3.11}$$

where $\eta = (T_d - T_{eq})/T_d$ is the atmosphere's thermodynamic efficiency, and $Q_{in} = 2\sigma T_{eq}^4 \times (1 - e^{-\tau_{LW}})$ is the amount of energy that is available to drive atmospheric motion. We note that the dayside-averaged incoming stellar flux is equal to $2\sigma T_{eq}^4$, but we additionally account for the fact that only a fraction $1 - e^{-\tau_{LW}}$ of stellar energy is available to the atmosphere, while the remainder is immediately re-radiated from the surface to space.

We find the following upper bound on the dayside average surface wind speed,

$$\begin{aligned} U_s &= \left[\frac{T_d - T_{eq}}{T_d} \times (1 - e^{-\tau_{LW}}) \frac{2\sigma T_{eq}^4}{C_D \rho_s} \right]^{1/3} \\ &= \left[\frac{T_d - T_{eq}}{T_d} \times (1 - e^{-\tau_{LW}}) \frac{2RT_d \sigma T_{eq}^4}{C_D p_s} \right]^{1/3} \\ &= \left[(T_d - T_{eq}) \times (1 - e^{-\tau_{LW}}) \frac{2R\sigma T_{eq}^4}{C_D p_s} \right]^{1/3}, \end{aligned} \tag{3.12}$$

where we used the ideal gas law to substitute for ρ_s in the second step. The only unknown in this equation is the dayside surface temperature T_d. As we saw in Section 3.3, T_d was already well constrained by the radiative-convective model (Fig. 3.3). In this section we therefore close the model using T_d from Equation 3.10a (but note that we will self-consistently solve for T_d in Section 3.5).

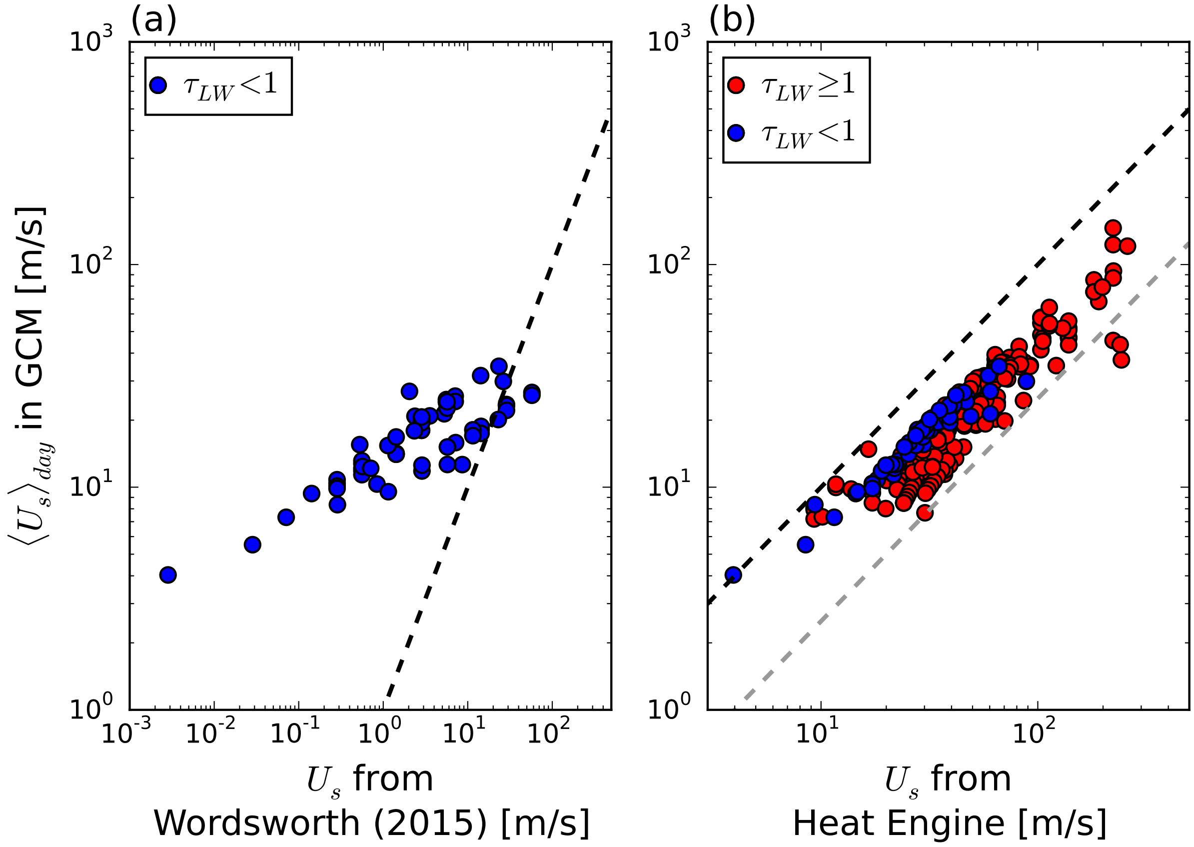

Figure 3.6: Two different surface wind speed scalings compared with many GCM results ($N = 271$). Left: scaling for dayside surface wind speed from Wordsworth (2015), which was derived assuming optically thin atmospheres ($\tau_{LW} < 1$). Right: our scaling for average surface wind speed for an ideal heat engine (Eqns. 3.12 and 3.10a). The GCM simulations are less efficient than ideal heat engines and therefore have smaller surface wind speeds. The grey dashed line corresponds to an inefficiency factor of 1/4.

Figure 3.6 compares dayside averaged surface wind speeds $\langle U_s \rangle$ with a numerical wind speed scaling from Wordsworth (2015, see Appendix F) and our analytical heat engine scaling. We note that Wordsworth considered the optically thin limit, whereas our results are valid for arbitrary τ_{LW}. Wordsworth derived a scaling by assuming weak temperature gradients hold globally. In a weak-temperature-gradient (WTG) atmosphere, radiative cooling leads to subsidence, which Wordsworth assumed in turn drives the large-scale circulation. Figure 3.6 shows that the GCM wind speeds span two orders of magnitude, from 3 m s^{-1} up to about 300 m s^{-1}. The Wordsworth (2015) scaling seems to match these wind speeds at $\mathcal{O}(1)$ m s^{-1}. However, it predicts a strong decrease, down to less than 10^{-2} m s^{-1}, which is several orders of magnitude smaller than the GCM results (Fig. 3.6a). The mismatch arises because Wordsworth's global WTG scaling assumes winds are purely driven by radiative cooling, $U_s \propto \tau_{LW}$ (Appendix F), so U_s should rapidly vanish in the optically thin limit. Instead, Figure 3.1 shows that WTG balance breaks down in regions that are strongly convecting. The convecting regions in turn govern the return flow from the nightside to the dayside, which means that the effect of friction on the large-scale circulation cannot be neglected. Our heat engine scaling includes this effect and predicts very different dynamics. For example, in the optically thin limit the dayside temperature is approximately constant and $1 - e^{\tau_{LW}} \approx \tau_{LW}$, so $U_s \propto \tau_{LW}^{1/3}$ (Equation 3.12). Figure 3.6b supports our theory. The slope predicted by the heat engine provides an excellent fit to the GCM results. Moreover, we expect the heat engine to provide an upper bound on surface wind speeds. Our expectation is confirmed by the GCM simulations, which fall below the dashed black line in Figure 3.6b. In addition, the overestimate of $\langle U_s \rangle$ is small and generally amounts to less than a factor of 4 (grey dashed line in Figure 3.6b), with most simulations falling about a factor of 2 below the ideal limit.

Next, we use the surface wind speed scaling to place an upper bound on the strength of the day-night circulation. Of particular interest to us is the large-scale vertical motion on the nightside, which we will show governs the day-night heat transport and is critically important for the temperature structure on the nightside (Section 3.5). We express all vertical motions using pressure coordinates, that is, using the pressure velocity $\omega \equiv Dp/Dt$ where $\omega > 0$ means sinking motions. We take the surface wind speed U_s to be the characteristic horizontal velocity within the boundary layer. We relate the horizontal velocity in the boundary layer to the pressure velocity near the substellar point using mass conservation[4] (Equation A.1c),

$$\frac{\omega_{up}}{p_s} \sim \frac{U_s}{a}. \tag{3.13}$$

Figure 3.1b supports this scaling, and ω/ω_{up} near the substellar point is of order unity. However, Figure 3.1b also shows that there is a large asymmetry between rising and sinking motions. While air rises rapidly near the region of strongest convection at the substellar point, it sinks slowly over a large area outside the boundary layer. Figure 3.1c quantifies the asymmetry using A_{up}/A_{down}, the fraction of the atmosphere in which air rises versus sinks[5]. In the shown simulation rising air never covers more than 20% of the atmosphere, while its vertically averaged value is about 10% (dot in Fig. 3.1c). The asymmetry in vertical motions arises from the geometric asymmetry of the incoming stellar flux, and is distinct from the asymmetry of rising and sinking motions in Earth's tropics which is caused by the condensation of water during convection. Because upward and downward mass fluxes have to balance across a horizontal slice of atmosphere,

$$\rho A_{up}\omega_{up} = \rho A_{down}\omega_{down}, \tag{3.14}$$

where ρ is the density of an air parcel, we can relate the pressure velocity on the nightside to the dayside surface wind,

$$\omega_{down} = \frac{A_{up}}{A_{down}}\frac{p_s}{a} \times U_s. \tag{3.15}$$

Equation 3.15 explains how tidally locked planets sustain weak downward motions despite very large horizontal wind speeds. The time for a parcel of air to be advected horizontally

---

[4] A more accurate scaling than Equation 3.13 would be $\omega_{up}/p_s \sim U_s/\sqrt{A_{up}}$. However, as long as $A_{up}/A_{down} \sim \mathcal{O}(10^{-1})$, Equation 3.13 leads to essentially the same result.

[5] Because the uppermost layers of the atmosphere show both weakly rising and falling motions we define A_{up} as the area with "significant" upward motion where $\omega \leqslant 0.01 \times \min(\omega)$.

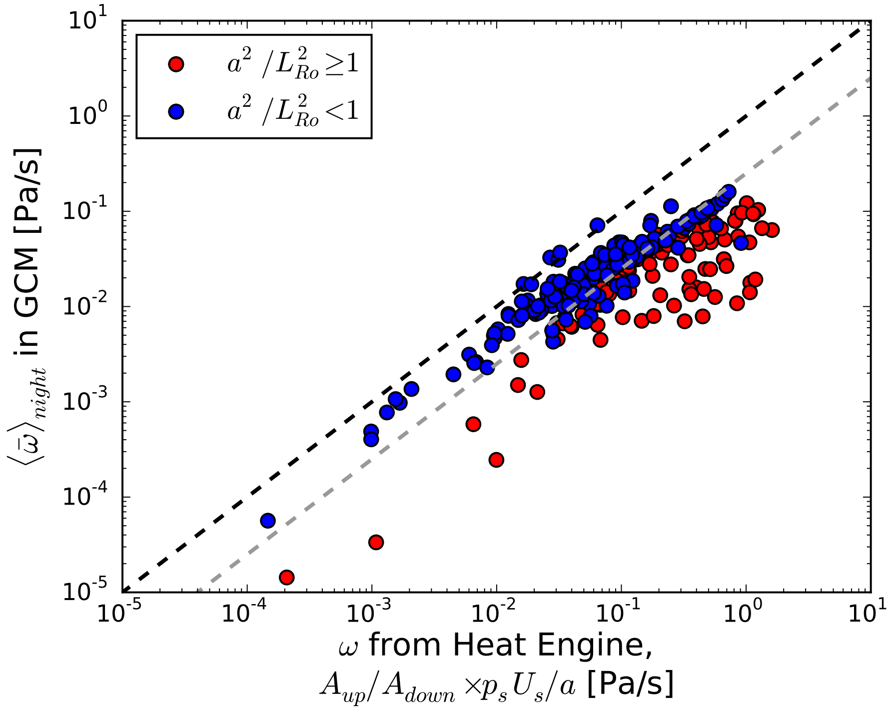

Figure 3.7: The heat engine scaling provides a strong constraint on the day-night atmospheric circulation. Shown is the vertical velocity in pressure coordinates predicted by the heat engine scaling (x-axis), compared with the average nightside pressure velocity in the GCM (y-axis). Rapidly rotating atmospheres, $a^2/L_{Ro}^2 \geqslant 1$, develop inhomogeneous nightsides and can locally sustain smaller pressure velocities (Section 3.7).

is $t_{adv} = a/U_s$ whereas the time for a parcel to subside (that is, be advected vertically) is $t_{sub} = p_s/\omega_{down} = A_{down}/A_{up} \times t_{adv}$. For $A_{down}/A_{up} \sim 10$ it takes a parcel of air ten times longer to sink back to the surface on the nightside than to be advected from the nightside to the dayside. The same comparison also explains why day-night temperature gradients of tidally locked planets are not set by the advective timescale and instead depend on the ratio of subsidence and radiative timescales (Section 3.6).

Next, Figure 3.7 compares the pressure velocity ω_{down} from Equation 3.15 with the mass-weighted vertically and horizontally averaged pressure velocities, $\langle\bar{\omega}\rangle_{night}$, from GCM simulations. In the comparison we use Equation 3.12 to predict U_s but still diagnose A_{up}/A_{down} directly from GCM output. First, because the heat engine provides an upper limit on U_s it also provides an upper limit on ω_{down}. The GCM simulations indeed fall almost entirely below the dashed black line in Figure 3.6b. We note that in deriving Equation 3.12 we neglected some factors that we expect to be small (e.g., geometric factors), but which explain why some GCM simulations slightly exceed the value predicted by the scaling. Second, we find that relatively slowly rotating atmospheres (blue dots) closely follow the heat engine scaling and most of them deviate less than a factor of 4 from it (grey dashed line). Third, rapidly rotating atmospheres (red dots) still follow the scaling qualitatively but $\langle\bar{\omega}\rangle_{night}$ is smaller than in slowly rotating atmospheres. The larger deviation arises because rapidly rotating atmospheres develop inhomogeneous nightsides (Section 3.7). In the extra-tropics the flow then becomes geostrophic which in turn suppresses vertical motions by $\mathcal{O}(Ro) \ll 1$, where Ro is the Rossby number (Showman et al., 2010).

We conclude that atmospheres of dry tidally locked planets are dominated by dayside boundary layer friction. The heat engine framework successfully constrains the amount of dissipation and surface wind speeds within the boundary layer. Combined with the areal asymmetry between rising and sinking motions, we find an upper bound on the nightside vertical velocity. Our result is distinct from previous scalings that have been proposed for exoplanets. We will use our result in the next section to constrain the thermal structure of the nightside.

3.5 A two-column radiative-convective-subsiding model

As we showed in Figures 3.3 and 3.4, to understand nightside surface temperatures of tidally locked planets we need to account for an imperfect day-night heat transport and to better constrain the nightside atmospheric temperature structure. In this section we develop a two-column model that does so. We again divide the atmosphere into two dayside and nightside columns, shown in Figure 3.8. As in Section 3.3 the dayside column is strongly convecting, but we allow the nightside temperature profile to deviate from an adiabat. Both columns are capped by a stratosphere, that is, a layer in pure radiative equilibrium.

As in our radiative-convective model, convection sets an adiabatic temperature profile on

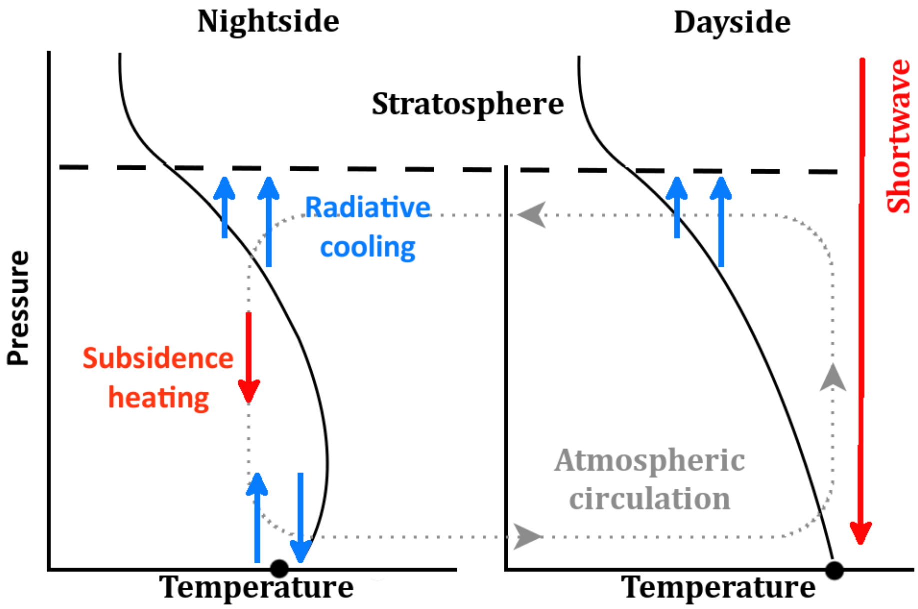

Figure 3.8: A diagram of the two-column radiative-convective-subsiding model. We assume convection sets an adiabatic temperature profile on the dayside, and a balance between radiative cooling and subsidence heating sets the temperature profile on the nightside. In addition, both columns are capped by a horizontally uniform and purely radiative stratosphere. The day-night circulation and the rate of subsidence are governed by the atmospheric heat engine.

the dayside. The dayside temperature profile is therefore

$$T = T_d \left(\frac{\tau}{\tau_{LW}}\right)^{\beta}. \tag{3.16}$$

The nightside is in weak-temperature-gradient (WTG) balance. WTG balance follows from the thermodynamic equation (Equation A.1d),

$$\frac{\partial T}{\partial t} + \mathbf{u}\cdot\nabla T + \omega\frac{\partial T}{\partial p} = \frac{RT\omega}{c_p p} + \frac{g}{c_p}\frac{\partial F}{\partial p} + \frac{g}{c_p}\frac{\partial \mathcal{D}}{\partial p}, \tag{3.17}$$

where **u** is the horizontal velocity, ω is the pressure velocity ($\omega > 0$ for subsiding air), F is the net radiative flux (the sum of upward and downward longwave fluxes, $F = F^{\uparrow} - F^{\downarrow}$), and

D is the energy flux due to diffusion. The left side of the thermodynamic equation represents advection, the first term on the right is heating/cooling due to compression/expansion as air parcels move vertically, the second term on the right is radiative heating/cooling, and the third term represents the effect of small-scale convection inside the boundary layer. In equilibrium $\partial T/\partial t = 0$, and $\mathcal{D}$ is negligible on the nightside because the nightside is stably stratified. As long as horizontal temperature gradients are small on the nightside the thermodynamic equation then reduces to WTG balance

$$\omega\left(\frac{\partial T}{\partial p} - \frac{RT}{c_p p}\right) \approx \frac{g}{c_p}\frac{\partial F}{\partial p}. \tag{3.18}$$

Equation 3.18 entails that radiative cooling is accompanied by subsidence as follows. In a cooling layer the net radiative flux decreases towards the surface, $\partial F/\partial p < 0$. The lapse rate has to be smaller than, or equal to, the adiabatic lapse rate because the atmosphere would otherwise start convecting, $\partial T/\partial p \leqslant RT/(c_p p)$. It follows that $\omega > 0$.

In Earth's tropics the vertical temperature structure, $\partial T/\partial p$, and radiative fluxes, $\partial F/\partial p$, are set by small regions of moist convection, in which case WTG can be used to predict the large-scale ω (Sobel et al., 2001). In this section we pursue the opposite approach: because ω is set by the day-night circulation which, in turn, is limited by friction in the dayside boundary layer (Section 3.4), we will use WTG balance to solve for T and F. For simplicity we replace ω with its vertical average $\bar{\omega}$. Because we assume that horizontal variations are small, we also replace all partial derivatives with normal derivatives. We rewrite WTG balance in optical depth coordinates and combine it with the Schwarzschild equation for the radiative flux F,

$$\frac{c_p\bar{\omega}}{g}\left(\frac{dT}{d\tau} - \frac{\beta T}{\tau}\right) = \frac{dF}{d\tau}, \tag{3.19a}$$

$$\frac{d^2F}{d\tau^2} - F = -2\frac{d(\sigma T^4)}{d\tau}. \tag{3.19b}$$

Given boundary conditions, these equations can be solved for T and F. The left side of Equation 3.19a represents the vertical energy flux due to subsidence (in W m^{-2}). In the WTG regime subsidence is how the atmosphere transports heat between dayside and nightside. Atmospheres with strong subsidence (large $\bar{\omega}$) will tend to have nightsides that are close to an adiabat, while atmospheres with very weak subsidence will tend to approach pure radiative equilibrium on their nightsides (i.e., $dF/d\tau \approx 0$).

To solve for T and F on the nightside we need to specify an upper boundary condition. A natural choice is the tropopause, τ_0, up to which convection rises on the dayside. Above τ_0 the atmosphere is in pure radiative equilibrium, $dF/d\tau = 0$. We assume the stratosphere is horizontally uniform, which means it has the same temperature structure as in Pierrehumbert (2011b),

$$T_{strat} = T_{eq}\left(\frac{1+\tau}{2}\right)^{1/4}. \tag{3.20}$$

We can now specify the boundary conditions for the nightside atmosphere and Equations 3.19. Because WTG balance is a first-order equation and the radiative equation is a second-order equation we require three conditions,

$$T(\tau_0) = T_{strat}(\tau_0), \tag{3.21a}$$

$$dF(\tau_0)/d\tau = 0, \tag{3.21b}$$

$$F(\tau_{LW}) = 0. \tag{3.21c}$$

The first equation is temperature continuity at the tropopause. The second is the stratospheric energy budget, that is, pure radiative equilibrium. The third condition is the nightside surface energy budget. Because the nightside surface is in radiative equilibrium with the overlying atmosphere, $F^{\uparrow}(\tau_{LW}) = F^{\downarrow}(\tau_{LW})$, the net radiative flux $F = F^{\uparrow} - F^{\downarrow}$ has to vanish at the surface. The only unknown in these boundary conditions is the tropopause height τ_0.

The tropopause height τ_0 is in turn governed by convection on the dayside. On the dayside, the convective temperature profile (Equation 3.16) has to match the stratospheric temperature profile (Equation 3.20) at τ_0, so

$$\begin{aligned} T_d \left(\frac{\tau_0}{\tau_{LW}}\right)^{\beta} &= T_{strat}(\tau_0), \\ T_d \left(\frac{\tau_0}{\tau_{LW}}\right)^{\beta} &= T_{eq}\left(\frac{1+\tau_0}{2}\right)^{1/4}. \end{aligned} \qquad (3.22)$$

Finally, we use the top-of-atmosphere (TOA) energy budget to constrain T_d. The global TOA energy budget is

$$2\sigma T_{eq}^4 = F(0)_{day} + F(0)_{night}. \qquad (3.23)$$

The left side is the incoming solar radiation and the right side is the dayside and nightside outgoing longwave radiation (OLR). To specify these fluxes we note that the stratosphere is in radiative equilibrium, $dF/d\tau = 0$, so the OLR has to match the net flux at the tropopause, $F(0) = F(\tau_0)$. The net radiative flux at the dayside tropopause is

$$F(\tau_0)_{day} = \sigma T_d^4 e^{-(\tau_{LW}-\tau_0)} + \sigma T_d^4 \int_{\tau_0}^{\tau_{LW}} \left(\frac{\tau'}{\tau_{LW}}\right)^{4\beta} e^{-(\tau'-\tau_0)} d\tau' - \sigma T_{eq}^4 \frac{\tau_0}{2}. \qquad (3.24)$$

The first two terms are the upwelling flux at the dayside tropopause (from the surface and atmosphere respectively), and the third term is downward flux from the stratosphere (Robinson & Catling, 2012). The global TOA energy budget therefore is,

$$2\sigma T_{eq}^4 = \sigma T_d^4 e^{-(\tau_{LW}-\tau_0)} + \sigma T_d^4 \int_{\tau_0}^{\tau_{LW}} \left(\frac{\tau'}{\tau_{LW}}\right)^{4\beta} e^{-(\tau'-\tau_0)} d\tau' - \sigma T_{eq}^4 \frac{\tau_0}{2} + F(\tau_0)\quad (3.25)$$

Equations 3.21-3.25 determine the tropopause height τ_0, the dayside surface temperature T_d, and the nightside OLR $F(\tau_0)$.

Finally, we constrain the pressure velocity $\bar{\omega}$ on the nightside. We showed in Figure 3.7

that the heat engine scaling allows us to place an upper bound on $\bar{\omega}$ once we account for the fact that atmospheres are imperfect heat engines and once we know the relative fraction of rising versus subsiding motions, A_{up}/A_{down} (we consider rotation in Section 3.7). In this section we incorporate these effects via

$$\omega_{down} = \chi \times \frac{p_s U_s}{a} \tag{3.26}$$

where χ captures the inefficiency of the heat engine as well as the smallness of A_{up}/A_{down}. We again use Equation 3.12 to compute U_s, but now we self-consistently solve for the dayside temperature T_d. To constrain χ we note that the asymmetry between rising and sinking motions is set by the tidally locked geometry and hence should not vary much between different simulations. We use $A_{up}/A_{down} \approx 0.1$ from Figure 3.1c as a representative value. Similarly, for slowly rotating atmospheres we found that $\bar{\omega}$ falls between the value predicted by the heat engine and about a factor of four less (Fig. 3.7), so we choose a representative inefficiency of 1/2. Combining these two, we find $\chi = 1/20$. Because rapidly rotating atmospheres tend to have weaker nightside subsidence (Figure 3.7), our choice of χ is an upper bound for ω_{down} and will overestimate the day-night heat transport on rapidly rotating planets. We emphasize that χ is the only tunable parameter in our model and is fixed to a single value. We do not change χ when we compare the radiative-convective-subsiding model with different GCM simulations.

We numerically solve the model to find the nightside temperature T and radiative flux F, the dayside surface temperature T_d, the nightside surface temperature T_n and the tropopause height τ_0. The boundary conditions for T and F are specified at the tropopause and at the surface, so we use a shooting method (Appendix G). We note that the Schwarzschild equation (Equation 3.19b) becomes difficult to solve accurately in the optically thick limit because the radiative boundary conditions at the tropopause and surface decouple at large τ_{LW} (Equations 3.21b,c). Nevertheless, the underlying physics do not change qualitatively once

$\tau_{LW} \gg 1$. We therefore avoid these issues by limiting our numerical solver to atmospheres with $\tau_{LW} \leqslant 15$.

Figure 3.4b compares the radiative-convective-subsiding (RCS) model with the same slowly rotating GCM simulation as in Figure 3.4a. The RCS model produces an adiabatic temperature profile on the dayside and an inversion on the nightside. Compared to the radiative-convective model (RC, Fig. 3.4a), the RCS model produces a colder nightside and a warmer dayside because it does not assume that the day-night heat transport is necessarily highly effective. The predicted temperatures match the GCM significantly better, particularly on the nightside. The RCS model also places the tropopause at $p/p_s \sim 0.3$, whereas the GCM tropopause is higher up, at $p/p_s \sim 0.1$. The high tropopause in the GCM arises because it is set by the deepest convection and hottest temperatures near the substellar point instead of the average dayside temperature (Fig. 3.4b), which the RCS model does not account for. Finally, the inversion structure in the RCS model is somewhat skewed compared with the GCM, and the inversion occurs higher up in the atmosphere (Fig. 3.4b). The raised inversion is likely due to our assumption of a vertically constant value of ω. Nevertheless, given the simplicity of the RCS model, we consider the fit between the RCS model and the GCM highly encouraging. We emphasize that the RCS model is obtained via a simple numerical solution, and is conceptually much simpler (and computationally much cheaper) than the full GCM.

Next, Figure 3.9 compares the RC and RCS models with many GCM simulations. The top row compares the radiative-convective model (RC) with the GCM, the bottom row does the same for the radiative-convective-subsiding (RCS) model. We note that in rapidly rotating atmospheres ($a^2/L_{Ro}^2 \geqslant 1$) WTG balance does not hold at higher latitudes, and both models should break down. However, WTG balance actually provides a good approximation of the nightside structure even at rapid rotation provided the atmosphere is not too hot or thin ($t_{wave}/t_{rad} \gtrsim 5 \times 10^{-2}$). We explain this threshold in Sections 3.6 and 3.7, here we simply mark simulations for which the RCS model could break down in red and all other simulations

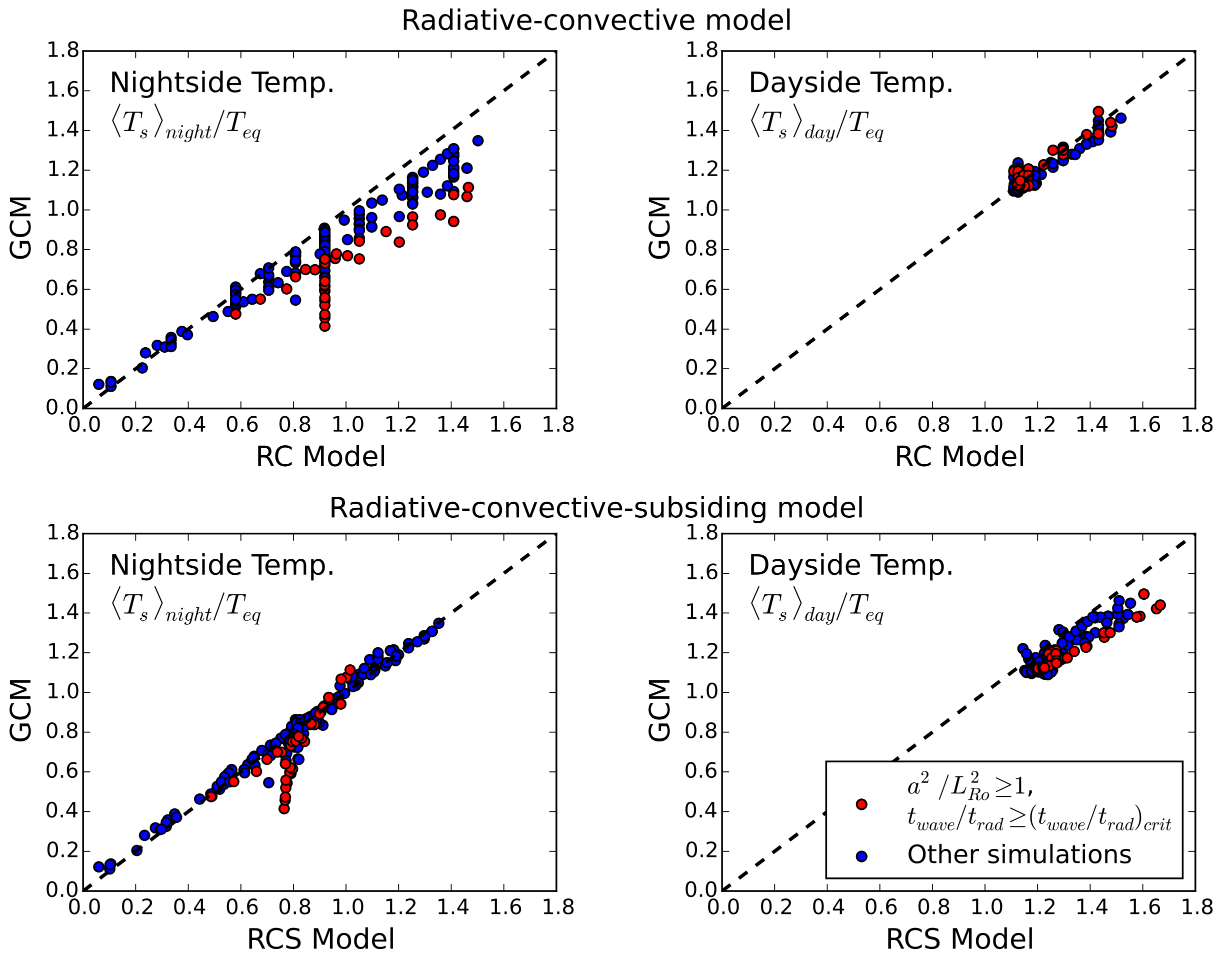

Figure 3.9: Comparison of surface temperatures predicted by the radiative-convective (RC) and radiative-convective-subsiding (RCS) models with many GCM simulations ($N = 241$). Red dots represent simulations that are both rapidly rotating and have hot/thin atmospheres ($a^2/L_{Ro}^2 \geqslant 1$ and t_{wave}/t_{rad} exceeds threshold from Equation 3.34), blue dots show all other simulations. Top left: average nightside temperature, RC model vs. GCM. Top right: average dayside temperature, RC model vs. GCM. Bottom left: average nightside temperature, RCS model vs. GCM. Bottom right: average dayside temperature, RCS model vs. GCM. The RCS model captures nightside temperatures much better than the RC model. The RCS model breaks down only for atmosphere that are both rapidly rotating and hot/thin (red dots; see Section 3.7).

in blue. First, as we already explained for Figure 3.4b, the RCS model generally predicts warmer daysides than the RC model, which already overestimates dayside temperatures slightly (see right panels in Fig. 3.9). To quantify the goodness of fit between the GCM and our models, we compute r^2 values for the simulations marked in blue. For dayside temperatures we find $r^2 = 0.82$ with the RC model, and $r^2 = 0.23$ with the RCS model.

These values underline that the RC model already captures the basic structure of the dayside. Improving the fit even further would require addressing the spatial inhomogeneity on the dayside (Fig. 3.1), whereas the reduced heat transport in the RCS model actually worsens its dayside fit. Second, as in Figure 3.3, Figure 3.9 shows that the RC model overpredicts nightside surface temperatures (top left panel). In contrast, the RCS model fits the GCM values extremely well (bottom left panel). For nightside temperatures we find $r^2 = 0.76$ with the RC model, while the RCS model essentially reproduces the GCM results with a fit of $r^2 = 0.98$.

To conclude, we have formulated a radiative-convective-subsiding model that utilizes WTG balance combined with the heat engine scaling for the large-scale circulation to capture the day-night heat transport and nightside temperature structure. Our model captures the day-night temperature structure of many GCM simulations extremely well. We provide an intuitive understanding of the model results in the next section.

3.6 Transition to large day-night temperature gradients

In this section we explain the threshold at which atmospheres of tidally locked rocky planets develop large day-night temperature gradients. We point out again that hot Jupiter theories suggest this should occur when $t_{wave}/t_{rad} \gtrsim 1$ (Section 3.1). In contrast, we show that on rocky planets the threshold is up to two orders of magnitude smaller and temperature gradients become large when $t_{wave}/t_{rad} \gtrsim \mathcal{O}(10^{-2})$. The small threshold is important because it means rocky exoplanets are relatively more sensitive to the parameter t_{wave}/t_{rad}, so planets that are relatively cool or have thick atmospheres still exhibit large day-night temperature differences. Finally, we relate the RCS model back to previous theories by showing that it reduces to our RC model for $t_{wave}/t_{rad} \lesssim 10^{-4}$ and to Wordsworth (2015)'s result for $t_{wave}/t_{rad} \gtrsim 1$ and $\tau_{LW} \ll 1$.

To start, we consider the thermodynamic equation under WTG balance (Equation 3.19a). WTG balance expresses a balance between subsidence heating and radiative cooling, and we nondimensionalize it using $\hat{T} = T/T_{eq}$ and $\hat{F} = F/(\sigma T_{eq}^4)$. We find that the ratio of subsidence heating to radiative cooling is governed by two parameters,

$$\frac{d\hat{T}}{d\tau} - \beta\frac{\hat{T}}{\tau} = \left(\frac{t_{sub}}{t_{rad}}\right)\frac{d\hat{F}}{d\tau}, \tag{3.27}$$

where $\beta = R/(c_p n)$ sets the adiabatic lapse rate, $t_{sub} \equiv p_s/\bar{\omega}$ is a characteristic subsidence timescale for a parcel of air and $t_{rad} = p_s c_p/(g\sigma T_{eq}^3)$ is the radiative cooling timescale. Equation 3.27 is the three-dimensional equivalent of the WTG scaling developed by Perez-Becker & Showman (2013) using the shallow-water equations. The lapse rate parameter β is always of order unity whereas the subsidence timescale t_{sub} is an emergent timescale set by the large-scale dynamics. When $t_{sub}/t_{rad} \ll 1$ radiative cooling is inefficient compared with subsidence heating, the nightside atmosphere is close to an adiabat, and day-night temperature differences are small. When $t_{sub}/t_{rad} \gtrsim 1$ a parcel of air cools significantly as it descends, the nightside develops inversions, and day-night differences are large. Finally, for $t_{sub}/t_{rad} \gg 1$ the nightside is close to radiative equilibrium.

The transition to large day-night temperature gradients occurs at a wave-to-radiative timescale threshold of $t_{wave}/t_{rad} \sim 10^{-2}$. Figure 3.10 shows temperatures from the RCS model as a function of the timescale ratio t_{wave}/t_{rad} and optical thickness τ_{LW}. We assume a representative rocky planet scenario[6], and plot the dayside surface temperature, $\langle T_s\rangle_{day}$, nightside surface temperature, $\langle T_s\rangle_{night}$, and the atmospheric temperature just above the nightside surface, $\langle T_{atm}\rangle_{night}$. Because the atmospheric temperature on the dayside is strongly coupled to the surface via convection, $\langle T_{atm}\rangle_{day} \approx \langle T_s\rangle_{day}$, the difference between $\langle T_s\rangle_{day}$ and $\langle T_{atm}\rangle_{night}$ also shows the day-night temperature gradient in the lowest part of the atmosphere. First, it is clear from Figure 3.10 that the atmospheric temperature gradient is small when $t_{wave}/t_{rad} \ll 10^{-2}$. The transition to large temperature gradients spans many orders of magnitude, but we take $t_{wave}/t_{rad} \sim 10^{-2}$ as a representative value

---

[6] We assume an Earth-sized planet, $a = a_{\oplus}$, with an N_2-dominated atmosphere, $(R, c_p) = (R, c_p)_{N_2}$.

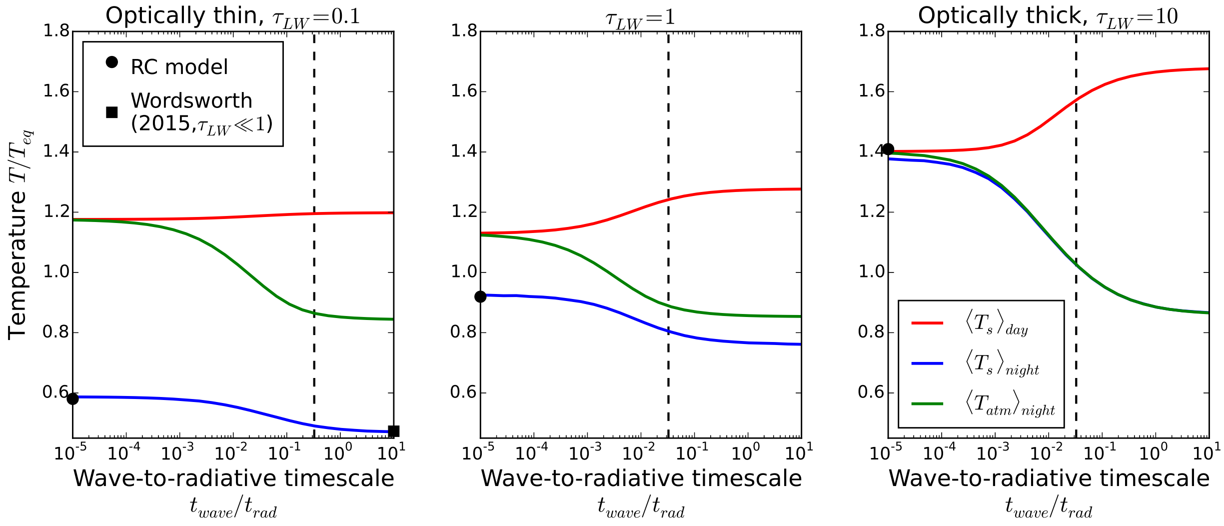

Figure 3.10: Day-night temperature gradients are large once the wave-to-radiative timescale ratio t_{wave}/t_{rad} exceeds the threshold from Equation 3.34 (vertical dashed lines). The panels show dayside surface temperature, $\langle T_s\rangle_{day}$, nightside surface temperature, $\langle T_s\rangle_{night}$, and the bottom-most atmospheric temperature on the nightside, $\langle T_{atm}\rangle_{night}$, from the radiative-convective-subsiding model (RCS, Section 3.5). In all cases, cool/thick atmospheres with $t_{wave}/t_{rad} \lesssim 10^{-4}$ have small temperature gradients between dayside surface and nightside atmosphere. Surface temperature gradients additionally depend on optical thickness, and even cool/thick atmospheres can have large day-night surface temperature gradients if $\tau_{LW} \ll 1$ (left panel). Black symbols show the nightside surface temperatures predicted by the radiative-convective model (RC), and the asymptotic scaling of Wordsworth (2015); the RCS model reduces to either in the limits $t_{wave}/t_{rad} \lesssim 10^{-4}$ and $t_{wave}/t_{rad} \gtrsim 1$.

that ensures temperature gradients are large for larger values of t_{wave}/t_{rad}. Second, once day-night atmospheric gradients are large their magnitude additionally depends on τ_{LW}, with optically thicker atmospheres having larger maximum temperature gradients (compare maximum difference between $\langle T_s\rangle_{day}$ and $\langle T_{atm}\rangle_{night}$). Third, because the nightside surface is in radiative equilibrium with the overlying atmosphere, the gradient in surface temperatures is at least as big as the gradient in atmospheric temperatures. However, it can be much larger in the optically thin limit because the nightside atmosphere becomes ineffective at radiatively heating the nightside surface. At low optical thickness the nightside surface is much colder than the overlying air (Fig. 3.10a), while at high optical thickness the nightside surface is closely tied to the overlying air temperature (Fig. 3.10c).

Next, we explain why atmospheres develop large temperature gradients at $t_{wave}/t_{rad} \sim$

10^{-2}. As we showed above, the nightside temperature structure is controlled by the ratio of subsidence to radiative timescales, t_{sub}/t_{rad}. Here we analyze the processes that control t_{sub}. Using the heat engine and the area ratio between upward and downward motions, we already found the pressure velocity on the nightside ω_{down}. Equation 3.26 allows us to write

$$t_{sub} = \frac{p_s}{\omega_{down}} = \frac{a}{\chi U_s}. \tag{3.28}$$

Next, we scale the surface wind speed U_s from the heat engine (Equation 3.12)

$$\begin{aligned} U_s &= \left[(T_d/T_{eq} - 1) \times (1 - e^{-\tau_{LW}}) \left(\frac{c_p}{R}\right)^2 \frac{t_{drag}}{t_{rad}} \right]^{1/3} \times c_{wave}, \\ U_s &\approx \left(\frac{c_p}{R}\right)^{2/3} \left(\frac{t_{drag}}{t_{rad}}\right)^{1/3} \times c_{wave}, \end{aligned} \tag{3.29}$$

where in the second step we assumed an optically thick atmosphere, $\tau_{LW} \geqslant 1$, so that all incoming stellar flux goes towards driving atmospheric motion, $1 - e^{-\tau_{LW}} \approx 1$. We also drop the dependence on the dayside temperature from $T_d/T_{eq} - 1$. We do so because in the optically thick limit T_d is approximately given by Equation 3.1, so $(T_d/T_{eq} - 1)^{1/3} \approx (\tau_{LW}^{\beta} \Gamma[1+4\beta]^{-1/4} - 1)^{1/3}$ which is always of order unity[7]. We combine Equations 3.28 and 3.29 and find

$$t_{sub} = \frac{1}{\chi} \left(\frac{R}{c_p}\right)^{2/3} \left(\frac{t_{rad}}{t_{drag}}\right)^{1/3} t_{wave} \tag{3.30}$$

Equation 3.30 gives us the subsidence time on the nightside. Day-night temperature gradients will be small if a parcel of air cools slower than it sinks, $t_{rad} > t_{sub}$. Conversely, day-night temperature gradients will be large if a parcel cools faster than it sinks, $t_{rad} < t_{sub}$. The

---

[7] For example, assuming $\tau_{LW} = 2$ and a diatomic gas without pressure broadening ($\beta = 2/7$), $(T_d/T_{eq} - 1)^{1/3} \approx 0.6$. The gamma function $\Gamma[1 + 4\beta]^{-1/4}$ does not vary significantly over the plausible range of atmospheric gases. Similarly, the dependency on $\tau_{LW}^{\beta/3}$ is negligible because the exponent $\beta/3$ is always small.

threshold between these two regimes is

$$\begin{aligned}
t_{rad} &\sim t_{sub} \\
t_{rad} &\sim \frac{1}{\chi}\left(\frac{R}{c_p}\right)^{2/3}\left(\frac{t_{rad}}{t_{drag}}\right)^{1/3} t_{wave} \\
t_{rad}^{2/3} &\sim \frac{1}{\chi}\left(\frac{R}{c_p}\right)^{2/3}\left(\frac{1}{t_{drag}}\right)^{1/3} t_{wave} \\
t_{rad} &\sim \left(\frac{1}{\chi}\right)^{3/2}\left(\frac{R}{c_p}\right)\left(\frac{t_{wave}}{t_{drag}}\right)^{1/2} t_{wave} \text{ (for } \tau_{LW} \geqslant 1). \qquad (3.31)
\end{aligned}$$

We can find a similar threshold for optically thin atmospheres ($\tau_{LW} < 1$). We note that the standard radiative timescale $t_{rad} = c_p p_s/(g\sigma T_{eq}^3)$ is the cooling timescale of an optically thick column of air. In contrast, an optically thin column of air only emits a radiative flux $\sim \tau_{LW} \times \sigma T_{eq}^4$ so its radiative cooling timescale is

$$t_{rad,thin} = \frac{t_{rad}}{\tau_{LW}}. \qquad (3.32)$$

WTG balance (Equation 3.27) in the optically thin regime is still governed by the ratio of subsidence to radiative timescales, but now t_{rad} has to be replaced by $t_{rad,thin}$.

To find the subsidence timescale t_{sub} in the optically thin limit, we note that optically thin atmospheres are also less efficient heat engines. The lower efficiency arises because, for $\tau_{LW} \ll 1$, the surface re-emits most of the incoming stellar flux directly back to space and only a fraction $1 - e^{-\tau_{LW}} = 1 - (1 - \tau_{LW} + ...) \approx \tau_{LW}$ of the stellar flux is available to drive atmospheric motions. The dayside temperature T_d is approximately constant in the optically thin case (Fig. 3.3), so t_{sub} is

$$t_{sub} = \frac{1}{\chi}\left(\frac{R}{c_p}\right)^{2/3}\left(\frac{t_{rad,thin}}{t_{drag}}\right)^{1/3} t_{wave}. \qquad (3.33)$$

Equation 3.33 only differs from Equation 3.30 through the use of $t_{rad,thin}$ instead of t_{rad}.

Our result for large temperature gradients therefore also holds for optically thin atmospheres, once we replace t_{rad} with $t_{rad,thin}$.

To compare our result with the result for hot Jupiters, we express the criterion for an atmosphere to develop large temperature gradients in terms of the wave-to-radiative timescale ratio t_{wave}/t_{rad}. Day-night atmospheric temperature gradients are large once

$$\frac{t_{wave}}{t_{rad}} \gtrsim \begin{cases} \chi^{3/2} \times \frac{c_p}{R} \left(\frac{t_{drag}}{t_{wave}}\right)^{1/2} & \text{if } \tau_{LW} \geqslant 1, \\ \\ \frac{\chi^{3/2}}{\tau_{LW}} \times \frac{c_p}{R} \left(\frac{t_{drag}}{t_{wave}}\right)^{1/2} & \text{if } \tau_{LW} < 1. \end{cases} \tag{3.34}$$

We emphasize that Equation 3.34 only ensures that atmospheric temperature gradients are large, but they remain significant until t_{wave}/t_{rad} becomes extremely small (Fig. 3.10).

We draw three important conclusions from Equation 3.34. First, in the optically thick case the right hand side is dominated by $\chi \approx 1/20$ (Section 3.5) while the other quantities do not vary much in most cases of interest. The small value of χ causes the threshold for large day-night temperature gradients to generally be much smaller than one. As a representative high mean-molecular-weight (MMW) scenario, we consider an N_2 atmosphere with $T_{eq} = 300$ K. In this case $c_p/R = 7/2$ and $t_{drag}/t_{wave} = 1.4$ (Appendix E), so temperature gradients are large when

$$\left(\frac{t_{wave}}{t_{rad}}\right)_{high\ MMW} \gtrsim 5 \times 10^{-2}. \tag{3.35}$$

Our result explains why rocky planets develop large atmospheric temperature gradients at a threshold almost two orders of magnitudes smaller than what one would expect based on the results for hot Jupiters, $t_{wave}/t_{rad} \gtrsim 1$.

Second, hot H_2-dominated atmospheres are a notable exception to the first result and develop day-night temperature gradients at larger values of t_{wave}/t_{rad}. The larger threshold arises because H_2-dominated atmospheres have larger scale heights than high-MMW atmospheres, which increases the drag time t_{drag}. For example, we consider a H_2 atmosphere with $T_{eq} = 600$ K. In this case $t_{drag}/t_{wave} = 40$ (Appendix E) so temperature gradients are large when

$$\left(\frac{t_{wave}}{t_{rad}}\right)_{H_2} \gtrsim 0.2. \tag{3.36}$$

The wave-to-radiative timescale threshold in this case is a factor of four larger than for high-MMW atmospheres, but it is still almost an order of magnitude smaller than the result for hot Jupiters, $t_{wave}/t_{rad} \gtrsim 1$.

Third, optically thin atmospheres are less prone to developing day-night temperature gradients than optically thick atmospheres because optically thin atmospheres cool less effectively. Although optically thin atmospheres are also less efficient heat engines, the radiative effect dominates because $t_{rad,thin} \propto 1/\tau_{LW}$ whereas $t_{sub} \propto t_{rad,thin}^{1/3} \propto 1/\tau_{LW}^{1/3}$. Weak-temperature-gradient (WTG) balance therefore holds even better in optically thin atmospheres than in optically thick ones. It also explains why the stratospheres of our simulations, where the atmosphere becomes optically thin (Robinson & Catling, 2012), are much more horizontally homogeneous than the lower atmosphere (Fig. 3.1).

We can now relate the RCS model to the results in Section 3.3. First, when $t_{sub}/t_{rad} \ll 1$ radiative cooling is inefficient compared to subsidence heating. In this limit sinking parcels of air on the nightside remain close to an adiabat and the RCS model reduces to the RC model[8]. Figure 3.10 shows nightside surface temperatures in both models and demonstrates that the RCS model reduces to the RC model at a representative value of $t_{wave}/t_{rad} \lesssim 10^{-4}$ (compare blue lines to black dots). Second, when $t_{sub}/t_{rad} \gg 1$ radiative cooling is much stronger than subsidence heating. In this limit WTG balance (Eqn. 3.27) becomes $dF/d\tau \approx 0$, so the

---

[8] Because the RCS model additionally includes a stratosphere, it predicts slightly colder nightsides in the limit $t_{wave}/t_{rad} < 10^{-4}$ than the RC model but the effect is small (the black dot is slightly above the blue line in Figure 3.10, right panel).

nightside is in purely radiative equilibrium and F is vertically constant. To still satisfy the nightside surface budget (Equation 3.21c), F has to be zero. The Schwarzschild equation (Eqn. 3.19b) shows that in this case $d(\sigma T^4)/d\tau \approx 0$ which means the nightside becomes vertically isothermal with a temperature that is set by the overlying tropopause temperature $T_{strat}(\tau_0)$. A lower bound for T_{strat} (see Eqn. 3.20) is given by the skin temperature $T_{skin} \equiv 2^{-1/4} T_{eq}$ (Pierrehumbert, 2011b). In the optically thin limit the nightside surface energy budget is then equal to $\sigma T_n^4 = \tau_{LW} \times \sigma T_{skin}^4 = \tau_{LW} \times \sigma T_{eq}^4/2$, and we recover Wordsworth (2015)'s result $T_n = T_{eq}(\tau_{LW}/2)^{1/4}$. Figure 3.10 shows that the nightside temperature in the RCS model reduces to this limit at a representative value of $t_{wave}/t_{rad} \gtrsim 1$ (compare black square and blue line in left panel).

Up to now we have focused on slowly rotating planets $a^2/L_{Ro}^2 < 1$. Next, we consider the effects of rapid rotation, and how they interact with the threshold for large day-night temperature gradients.

3.7 Effects of rapid rotation on temperature structure

In this section we use GCM simulations to address how rapid rotation affects the circulation and temperature structure. Leconte et al. (2013) showed that tidally locked planets develop drastically different circulations when $a^2/L_{Ro}^2 \gtrsim 1$ because equatorial waves are not able to freely propagate into high latitudes once the planetary radius, a, is larger than the equatorial Rossby radius, L_{Ro}. Rapidly rotating planets then develop standing Rossby and Kelvin wave patterns. The standing wave patterns lead to strong equatorial superrotation, an eastward offset of the equatorial hot spot, and off-equatorial cold vortices on the nightside (Matsuno, 1966; Showman & Polvani, 2011). Here we also find that the circulation regime changes at $a^2/L_{Ro}^2 \sim 1$. However, while rapid rotation drastically alters the flow field the effect on temperature structure is small unless the atmosphere is also prone to developing strong temperature gradients, $t_{wave}/t_{rad} \gtrsim \mathcal{O}(10^{-2})$.

We perform a set of GCM simulations in which we vary a^2/L_{Ro}^2 and t_{wave}/t_{rad} while

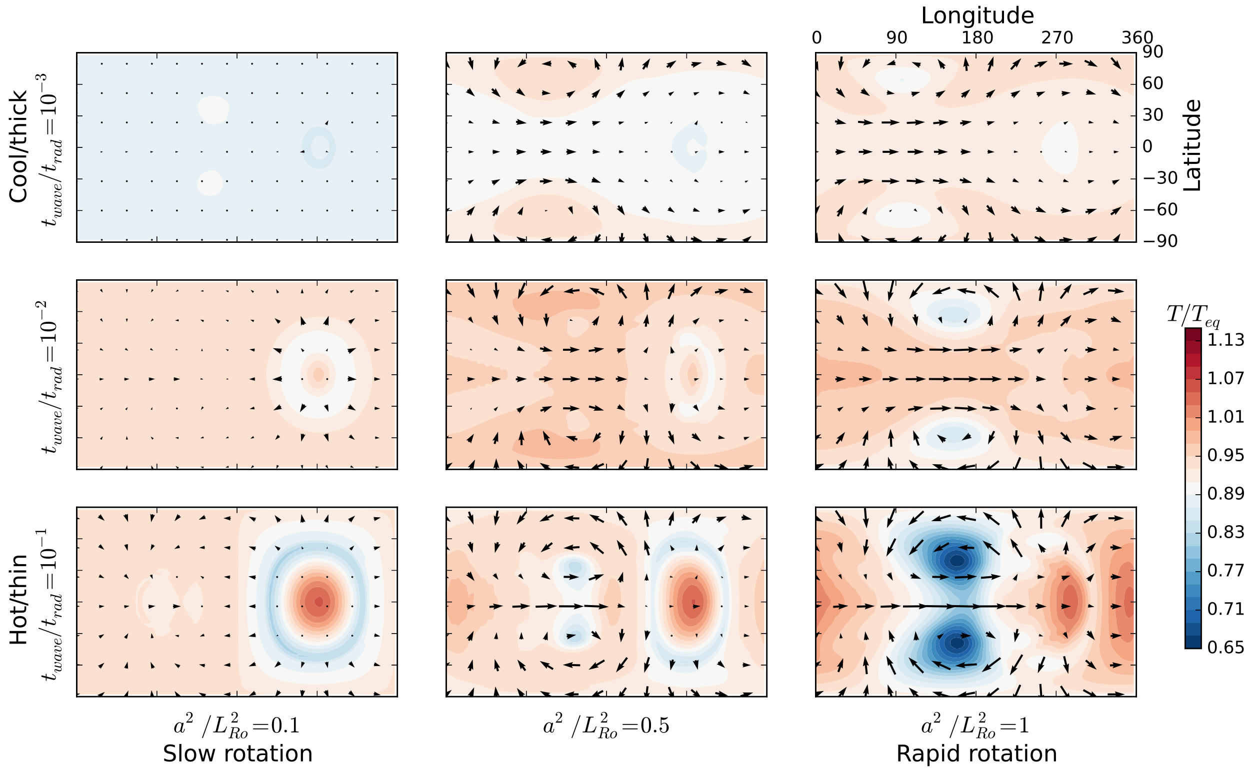

Figure 3.11: Rapid rotation ($a^2/L_{Ro}^2 \gtrsim 1$) does not have a strong effect on temperature structure unless the atmosphere is also hot or thin ($t_{wave}/t_{rad} > 10^{-2}$). Shown are 2D temperature and wind fields, averaged over the upper troposphere ($0.3 \leqslant p/p_s \leqslant 0.4$). Rotation increases from left to right, the wave-to-radiative timescale ratio increases from top to bottom. Increased rotation changes the circulation drastically, from a day-night flow at slow rotation (left) to an equatorially superrotating jet and cold nightside vortices at rapid rotation (right). However, at low t_{wave}/t_{rad} temperature gradients are small, even if rotation is rapid (top right). Large temperature gradients, eastward hot spot offsets, and cold nightside vortices only emerge once an atmosphere is both hot/thin and rotates rapidly (bottom right). The substellar point is located at 270° longitude.

keeping all other parameters fixed. We vary a^2/L_{Ro}^2 by changing the rotation rate Ω, and t_{wave}/t_{rad} by changing the surface pressure p_s. All other parameters are fixed to the same values as the reference simulation in Figure 3.1, that is, $a = a_{\oplus}$, $T_{eq} = 283\text{K}$, $(R, c_p) = (R, c_p)_{N_2}$, and $\tau_{LW} = 1$. We explore $a^2/L_{Ro}^2 = (0.1, 0.5, 1)$ and $t_{wave}/t_{rad} = (10^{-3}, 10^{-2}, 10^{-1})$, which correspond to $2\pi/60$ days $\leqslant \Omega \leqslant 2\pi/6$ days and 5 bar $\leqslant p_s \leqslant 0.05$ bar.

We find that rapid rotation has a large effect on the circulation, but its effect on the temperature structure is small unless t_{wave}/t_{rad} also exceeds the threshold $t_{wave}/t_{rad} \gtrsim 5 \times 10^{-2}$ from the previous section. Figure 3.11 shows 2D maps of the circulation and temperatures in the upper atmosphere. The wind and temperatures are mass-weighted averages taken over $0.3 \leqslant p/p_s \leqslant 0.4$, and the substellar point is located at longitude $\lambda = 270^\circ$. Slowly rotating simulations are shown in the left column of Figure 3.11. As expected, the circulation consists of a substellar-to-antistellar flow. At small values of t_{wave}/t_{rad} the day-night temperature differences are small, but the atmosphere develops large day-night temperature gradients at $t_{wave}/t_{rad} = 10^{-1}$, consistent with our results in Section 3.6. The top row of Figure 3.11 shows simulations with small t_{wave}/t_{rad}. As rotation rate increases, the atmospheric circulation changes drastically. A strong equatorial jet develops and the nightside atmosphere additionally develops standing Rossby waves in the form of off-equatorial vortices (Showman & Polvani, 2011). Nevertheless, as long as $t_{wave}/t_{rad} = 10^{-3}$, the maximum horizontal temperature difference at $a^2/L_{Ro}^2 = 1$ only reaches $0.05T_{eq}$, or ~ 15 K.

Figure 3.11 underlines that day-night atmospheric temperature gradients are primarily controlled by t_{wave}/t_{rad}. However, the effect of rapid rotation can strongly enhance temperature gradients in the form of eastward hot spot offsets and cold nightside vortices. The slowly rotating simulation with a thin atmosphere ($a^2/L_{Ro}^2 = 0.1$, $t_{wave}/t_{rad} = 10^{-1}$; bottom left) has its hottest point located at the substellar point and a maximum horizontal temperature difference of $0.2T_{eq}$, or ~ 65 K. In contrast, the simulation with the same value of t_{wave}/t_{rad} but at rapid rotation shows an eastward hot spot offset and a significantly larger maximal horizontal temperature difference of $0.4T_{eq}$, or ~ 110 K (bottom right). In the following section we consider what our results imply for future observations.

3.8 Implications for Observations

Figure 3.12 summarizes some implications of our results for observations of rocky exoplanets. We showed that atmospheric day-night temperature contrasts strongly depend on the

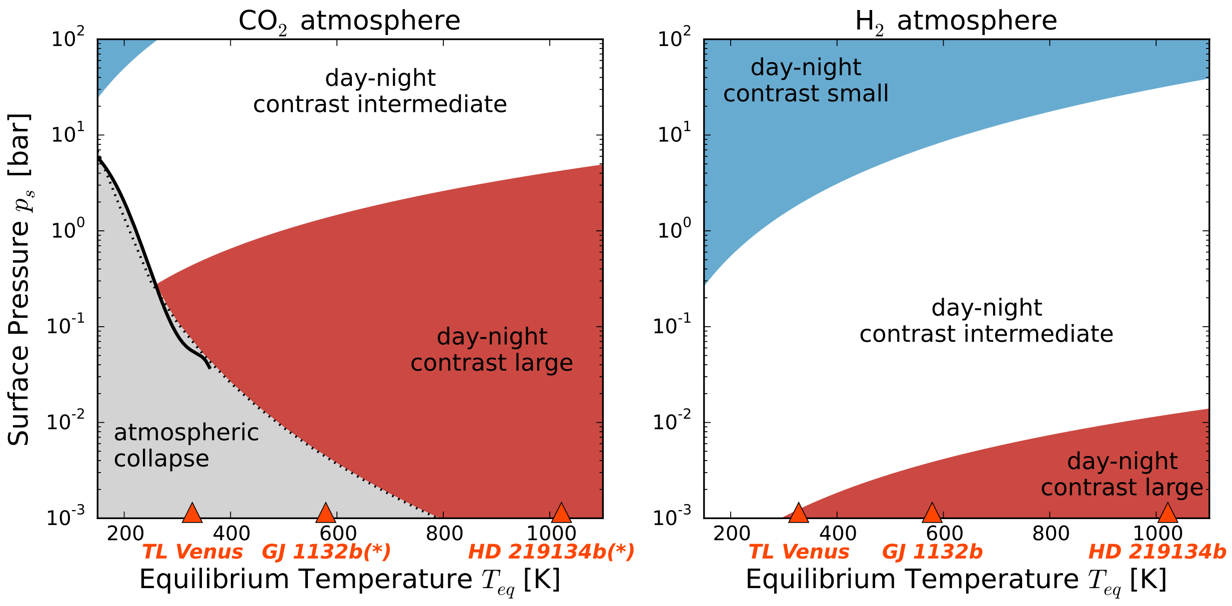

Figure 3.12: CO$_2$ atmospheres are more likely to develop large temperature gradients than H$_2$ atmospheres. Atmospheric day-night temperature gradients are negligible inside the blue region ($t_{wave}/t_{rad} \leqslant 10^{-4}$) and are large inside the red region (Eqn. 3.34 for $\tau_{LW} \geqslant 1$). CO$_2$ atmospheres collapse inside the grey region [solid line: empirical fit to GCM results from Wordsworth (2015); dotted line: calculated using our RCS model]. Bottom symbols show equilibrium temperatures of two nearby rocky planets and of a hypothetical tidally locked Venus; $(*)$ marks scenarios for which rotational effects would additionally be important ($a^2/L_{Ro}^2 \geqslant 1$). The shown thresholds assume a GJ1132b-sized planet ($a, g = 1.16a_{\oplus}, 11.7$ m s^{-2}).

parameter $t_{wave}/t_{rad} = a/(\sqrt{R/c_p} \times \sqrt{RT_{eq}}) \times g\sigma T_{eq}^3/(c_p p_s) \propto T_{eq}^{5/2}/p_s$. The planetary radius a and surface gravity g vary relatively little for plausible rocky planets, which means day-night temperature differences are to first order controlled by the equilibrium temperature T_{eq}, the surface pressure p_s, and whether or not the atmosphere is made of H$_2$ (via R and c_p). In Figure 3.12 we consider these parameters for a GJ 1132b-sized planet[9] with hypothetical CO$_2$ and H$_2$ atmospheres. The red region indicates when the atmosphere is hot/thin and develops large day-night atmospheric temperature gradients (Equation 3.34 for $\tau_{LW} \geqslant 1$). The blue region indicates when the atmosphere is cool/thick and day-night atmospheric temperature gradients become negligible ($t_{wave}/t_{rad} \leqslant 10^{-4}$ from Section 3.6). Part of the CO$_2$ phase space is unstable to atmospheric collapse, which occurs when the nightside

---

[9] We assume $a, g = 1.16a_{\oplus}, 11.7$ m s^{-2} (Berta-Thompson et al., 2015).

surface is cold enough for CO_2 to condense. We delineate atmospheric collapse using two approaches. First, the solid black line shows the empirical fit from Wordsworth (2015), who used a GCM with full radiative transfer to compute collapse thresholds up to $T_{eq} = 367$ K. Second, we use the RCS model to compute when nightside surface temperatures fall below the condensation temperature of CO_2. To specify the optical thickness we use Equation 3.6 and assume $\tau(1 \text{ bar}) = 1$ and $n = 1$. Although we do not include non-grey effects, the RCS model (dashed black line) closely fits the GCM results (solid black line) over the range of parameters explored by Wordsworth (2015). As such, we consider the RCS model appropriate for predicting atmospheric collapse (also see Section 3.9). We repeat a similar computation for H_2 atmospheres, and find that the entire phase space in Figure 3.12b is stable against collapse[10]. The symbols at the bottom of Figure 3.12 show equilibrium temperatures[11] of two recently-discovered rocky planets and of a hypothetical tidally locked planet at Venus' present-day orbit (Berta-Thompson et al., 2015; Motalebi et al., 2015). Finally, we found that temperature structure can be affected by rapid rotation. We mark all rapidly rotating planet scenarios with $a^2/L_{Ro} \geqslant 1$ using star symbols ($*$). For these cases we expect that strong rotational effects, such as large eastward hot spot offsets or cold nightside vortices, occur inside the red region (see Section 3.7).

Figure 3.12 allows us to make some tentative predictions. First, with a high MMW atmosphere like CO_2, GJ 1132b and HD 219134b would have non-negligible day-night temperature gradients. This conclusion holds even for surface pressures as high as that of Venus ($p_s = 92$ bar). Second, GJ 1132b and HD 219134b with CO_2 atmospheres both satisfy the criterion for rapid rotation ($a^2/L_{Ro}^2 \geqslant 1$). Should observations detect a large eastward hot spot offset, it would favor surface pressures less than $\mathcal{O}(1)$ bar (inside the red region). Third, Figure 3.12a shows that a CO_2 atmosphere with surface pressure comparable to that of Mars

---

[10] We use the Solar opacity value in Menou (2012a) and $n = 1$, and compute nightside surface temperatures with the RCS model. We find that nightside temperatures always exceed the critical point of H_2, 33.2 K.

[11] We assume a planetary albedo of zero.

($p_s = 6\times10^{-3}$ bar) would be close to collapse on GJ 1132b. We note that our collapse calculation does not account for rotational effects, and cold nightside vortices (Fig.3.11) would allow the atmosphere to collapse at even higher pressures. Fourth, if these planets managed to retain H_2-dominated atmospheres against atmospheric escape, they would be stable against collapse and exhibit much smaller day-night temperature differences than similar CO_2 atmospheres. The increased stability and smaller temperature gradient is due to a combination of H_2's large heat capacity c_p, which increases the radiative timescale t_{rad} (Menou, 2012a), its large gas constant R, which increases the speed of atmospheric waves c_{wave} and thus decreases the wave timescale t_{wave} (Heng & Kopparla, 2012), and its increased scale height, which decreases the effect of friction (Appendix E). Fifth, H_2-dominated atmospheres would be significantly less affected by rotation than CO_2 atmospheres. The smaller effect of rotation is also due to the reduced wave timescale t_{wave} in H_2 atmospheres. For example, assuming GJ 1132b's equilibrium temperature $T_{eq} = 579$K, the characteristic speed of gravity waves in a CO_2 atmosphere is $c_{wave} = \sqrt{R/c_p} \times \sqrt{RT_{eq}} = 158$m s^{-1}, whereas in a H_2 atmosphere $c_{wave} = 838$m s^{-1}. It follows that the nondimensional Rossby radius, $a^2/L_{Ro}^2 = 2\Omega a/c_{wave}$, is about five times smaller in a H_2 atmosphere. Our results also imply that rocky planets with H_2-dominated atmospheres are less likely to exhibit eastward hot spot offsets and cold nightside vortices. These predictions are qualitative because they do not consider the optical thickness τ_{LW}, which helps set the magnitude of the day-night temperature gradient (Fig. 3.10). Quantitatively interpreting an observed day-night temperature gradient also requires constraining τ_{LW}, for example via transit spectroscopy (see Koll & Abbot, 2015).

One way of distinguishing the scenarios in Figure 3.12 would thus be through combined transit spectroscopy and thermal phase curve observations with *JWST*. Previous feasibility studies have tended to emphasize the transit technique (e.g., Beichman et al., 2014; Batalha et al., 2015), here we compare the signal-to-noise ratio (SNR) that can be achieved by spending the same amount of *JWST* time on low spectral-resolution transit and broadband phase curve observations. We find that it would take about as much time to measure the broadband mid-IR phase curve of a short-period rocky exoplanet as it would to detect molecular signatures in its atmospheres through near-IR transit spectroscopy. The basic science goal for transit observations would be to detect a molecular species from its spectral imprint; a flat spectrum could alternately be a cloudy atmosphere or no atmosphere. The basic science goal for phase curve observations would be to detect the day-night flux difference of a bare rock. An observed flux difference lower than that of a bare rock would imply the presence of an atmosphere thick enough to modify the day-night temperature contrast (outside the red region in Fig. 3.12). Similarly, hot/cold spot offsets would imply the presence of an atmosphere that is hot or thin enough that its thermal structure is significantly affected by rotation (see above). We consider GJ 1132b with a CO_2-dominated atmosphere as a representative target. We assume GJ 1132b is tidally locked, which could be verified using optical phase curves with *TESS* (cf. Fujii et al., 2014). We compute transit signals following Cowan et al. (2015), but assume that spectral features in the near-IR cause an absorption difference of three scale heights and have a typical width of 0.1μm (see Table 2, Kaltenegger & Traub, 2009). We compute the phase curve signal of a bare rock following Koll & Abbot (2015). We estimate *JWST*'s precision in the near-IR ($1-4\mu$m in 0.1μm bins, $R\sim25$ on NIRSpec) using the photon noise limit (see Koll & Abbot, 2015). We similarly estimate the precision in the mid-IR ($16.5-19.5\mu$m broadband, F1800W on MIRI) assuming photon noise, but account for the imperfect instrument throughput of 1/3 (Glasse et al., 2010). We assume that both techniques bin photons over the length of one transit (45 minutes) and we multiply the noise by $\sqrt{2}$ to account for the fact that both techniques compare two snapshots in time. We assume that a single transit measurement consists of observing the primary eclipse and an equal out-of-transit baseline (cf. Kreidberg et al., 2014). We check our transit estimate by comparing our SNR with the detailed calculations in Batalha et al. (2015), and find that we can reproduce their results up to a factor of two (not shown). We also note that our estimate of GJ 1132b's thermal emission is slightly higher than the signal in Berta-Thompson et al. (2015), because the observer-projected dayside temperature of a

Transit vs. phase curve observations of GJ 1132b with *JWST*

Method	Observation Time	Signal (ppm)	Noise (ppm)	SNR
Single transit[a]	one transit[b] = 90 min	19.9	19.7	1
Stacked transits[a]	13 transits = 19.5 hours	19.9	5.5	4
Thermal phase curve[c]	one half-orbit = 19.5 hours	373	84	4

[a] $1-4\mu$m, NIRSpec, $R \sim 25$, CO_2-dominated atmosphere.

[b] We assume a measurement lasts 45 min in-transit, plus 45 min out-of-transit baseline.

[c] $16.5-19.5\mu$m, MIRI, broadband.

Table 3.2: Transit spectroscopy and thermal phase curve measurements of a planet like GJ 1132b will require similar amounts of *JWST* observation time. The shown signal-to-noise (SNR) ratios are estimates for the most basic observational goals: detecting molecular features in low-resolution near-IR transit spectra, and detecting the day-night thermal emission contrast of a bare rock in the mid-IR. We compute signals following Cowan et al. (2015) and Koll & Abbot (2015). We estimate noise assuming photon-limited precision, but include imperfect instrument throughput for MIRI (see Section 3.8).

bare rock is higher than its equilibrium temperature by $(8/3)^{1/4} \approx 1.28$ (Koll & Abbot, 2015).

Table 3.2 shows our results. Similar to previous estimates (e.g., Batalha et al., 2015; Cowan et al., 2015), we find that a single transit would not be sufficient to conclusively identify molecular absorption features (SNR $\sim$ 1). The low SNR arises largely because of the high MMW atmosphere; for comparison, a H_2 atmosphere on GJ 1132b should be detectable in a single transit with SNR $\sim$ 22. For a CO_2 atmosphere, 13 repeated transit observations would reduce the noise sufficiently to allow spectral features to be discerned with SNR $\sim$ 4. The time it takes to measure 13 repeated transits of GJ 1132b is also equal to the time it takes to measure one half-orbit phase curve (from transit to secondary eclipse). We find that the thermal emission of a bare rock would be detectable with a comparable SNR $\sim$ 4. We conclude that characterizing high MMW atmospheres of rocky exoplanets will require relatively large investments of *JWST* time. If such observations are pursued, however, then thermal phase curves are a feasible technique that would yield important complementary information about these planets (Koll & Abbot, 2015).

3.9 Discussion

The heat engine framework is well-established for Earth's atmosphere (e.g., Peixoto & Oort, 1984). Similarly Goodman (2009) pointed out that hot Jupiters can be viewed as heat engines, but did not develop his insight more quantitatively. Here we have demonstrated that the atmospheres of rocky exoplanets act as heat engines, which allowed us to develop a new constraint on their day-night circulations. We also found that surface wind speeds in most of our GCM simulations are about a factor of two smaller than the value predicted by the heat engine (Fig. 3.6). Because work scales with the cube of the surface wind speed, our simulations produce $\sim (1/2)^3 = 1/8$ as much work as an ideal heat engine. Interestingly, Earth's atmospheric heat engine also produces about an order of magnitude less work than its ideal limit and therefore has a similar inefficiency as our dry and tidally locked simulations (Peixoto & Oort, 1984). Our result seems to be at odds with the usual understanding that the inefficiency of Earth's atmospheric heat engine is caused by its hydrological cycle (Pauluis et al., 2000; Pauluis, 2010), and also raises the question whether our scaling can be generalized to planets that are not tidally locked. We hope to address these issues in future work. Our results also strongly suggest that hot Jupiters should obey similar constraints as rocky planets. For example, using the heat engine framework it might be possible to constrain the day-night overturning circulation, which controls the vertical mixing and chemical equilibrium of hot Jupiter atmospheres. However, modeling these atmospheres as heat engines will require a better understanding of the mechanisms through which they dissipate kinetic energy, which could include magneto-hydrodynamic drag, shocks, or shear instabilities (Li & Goodman, 2010; Menou, 2012b; Fromang et al., 2016).

Our results allow us to interpret previous GCM results that have not been fully explained yet. First, Merlis & Schneider (2010) explored Earth-like atmospheres at different rotation rates. They found that although the strength of superrotation is strongly dependent on rotation rate, day-night surface temperature gradients are mostly insensitive to rotation rate (their Fig. 15). Our results explain why: Merlis & Schneider varied rotation rates while keeping the stellar flux fixed at Earth's value. Their simulations were therefore in the rapidly rotating ($a^2/L_{Ro}^2 > 1$) but relatively cool/thick regime ($t_{wave}/t_{rad} < 10^{-2}$) in which temperature structure is not strongly sensitive to rotation (Fig. 3.11). Second, in Koll & Abbot (2015) we found that thermal phase curves are mainly sensitive to the nondimensional parameters t_{wave}/t_{rad} and τ_{LW}. Our result only broke down for hot/thin and rapidly rotating atmospheres, $t_{wave}/t_{rad} \gtrsim 10^{-2}$ and $a^2/L_{Ro}^2 \gtrsim 1$. Our results here explain both the wave-to-radiative timescale threshold of $t_{wave}/t_{rad} \sim 10^{-2}$ and why rotation is relatively unimportant (Figs. 3.10 and 3.11).

There are additional physical effects that might affect our conclusions. We assume broadband grey radiative transfer, but a wide range of plausible atmospheric compositions feature significant spectral window regions. As already noted by Leconte et al. (2013) and Wordsworth (2015), window regions allow the nightside surface to cool even more effectively, which would increase day-night surface temperature gradients compared to that predicted by our grey models. At the same time, large spectral window regions would increase the atmosphere's radiative cooling timescale and thus reduce atmospheric temperature gradients, similar to the optically thin cases we discussed in Section 3.6. We also did not consider shortwave absorption. Shortwave absorption will shift heating to lower pressures, which would decrease the heat intake temperature of the atmospheric heat engine and reduce the atmospheric circulation strength. We therefore expect our heat engine theory to be an upper bound on wind speeds.

Many planets might be able to retain a hydrologic cycle (e.g., H_2O inside the habitable zone, or CH_4 on Titan-like planets) against atmospheric escape and nightside collapse. Besides changing the atmosphere's radiative properties (e.g., H_2O effectively absorbs both in the shortwave and longwave), condensation would also modify the atmospheric dynamics. Moist GCM simulations indicate that the temperature and circulation structure sketched out in Figure 3.8 could still apply qualitatively (Merlis & Schneider, 2010; Yang et al., 2013), but with several modifications. First, latent heat transport would reduce the day-night temperature gradient compared to dry atmospheres (Leconte et al., 2013). Second, moist convection would lead to thick cloud cover on the dayside and could drastically change a planet's appearance to remote observers (Fortney, 2005; Yang et al., 2013). Third, dry atmospheres develop strongly turbulent daysides. The friction associated with this dry convection allows the nightside temperature structure to decouple from regions of convection (Fig. 3.1, Voigt et al., 2012). In contrast, moist atmospheres such as Earth's tropics maintain an adiabatic temperature profile through deep moist convection, while the dry turbulent boundary layer is relatively shallow. We therefore expect that moist atmospheres would be less dominated by friction, and would be even better captured by WTG models similar to our radiative-convective model (Section 3.3).

It is an open question how many rocky planets around M-stars will actually be tidally locked. Leconte et al. (2015) found that thermal tides in relatively thick atmospheres ($p_s \gtrsim 1$ bar) can prevent habitable-zone planets around early M-dwarfs from reaching a tidally locked state. Although thermal tides could limit the application of our results to planets on longer-period orbits, they are less likely to apply to planets around late M-dwarfs or hot exoplanets like GJ 1132b. Moreover, given that rocky exoplanets are extremely common, we also expect that future discoveries will find rocky exoplanets in a wide range of rotational states. Optical phase curves could constrain the rotation rates of these planets without relying on models (Fujii et al., 2014), while future theoretical work should consider the connection between the tidally locked limit we considered here and planets in higher-order spin-orbit resonances.

3.10 Conclusions

We have developed a series of theoretical models to understand the basic temperature structure and large-scale circulations of tidally locked planets with dry atmospheres. These models are able to capture and predict many fundamental aspects of much more complex GCM simulations, including the atmospheric temperature structure, dayside and nightside surface temperatures, as well as large-scale wind speeds. We draw the following conclusions from our work:

1. Our radiative-convective model describes tidally locked atmospheres with efficient day-night heat transport and applies in the limit of cool and thick atmospheres ($t_{wave}/t_{rad} \lesssim 10^{-4}$). It captures the basic temperature structure of tidally locked planets and extends the asymptotic theory for optically thick atmospheres ($\tau_{LW} \gg 1$, Pierrehumbert, 2011b) to arbitrary optical thickness.

2. Atmospheres of dry, tidally locked exoplanets act as global heat engines. Our heat engine scaling places strong constraints on the day-night circulation strength of tidally locked atmospheres.

3. Our radiative-convective-subsiding model describes tidally locked atmospheres with limited day-night heat transport. It extends both our radiative-convective model and the asymptotic theory for optically thin atmospheres ($\tau_{LW} \ll 1$, Wordsworth, 2015), and captures the dynamics of a wide range of complex GCM simulations. It breaks down in the limit of atmospheres that are both rapidly rotating ($a^2/L_{Ro}^2 \gtrsim 1$) and hot/thin ($t_{wave}/t_{rad} > \mathcal{O}(10^{-2})$).

4. Like hot Jupiters, day-night atmospheric temperature gradients of rocky exoplanets become large once parcels of air take longer to subside than to cool radiatively. Unlike hot Jupiters, the timescale for subsidence on rocky planets is severely increased by the limited heat engine efficiency and the areal asymmetry between convection and subsidence. Rocky planets develop large day-night atmospheric temperature gradients when

$$\frac{t_{wave}}{t_{rad}} \gtrsim \begin{cases} \chi^{3/2} \times \dfrac{c_p}{R} \left(\dfrac{t_{drag}}{t_{wave}}\right)^{1/2} & \text{if } \tau_{LW} \geqslant 1, \\ \dfrac{\chi^{3/2}}{\tau_{LW}} \times \dfrac{c_p}{R} \left(\dfrac{t_{drag}}{t_{wave}}\right)^{1/2} & \text{if } \tau_{LW} < 1. \end{cases} \tag{3.37}$$

Optically thin atmospheres cool inefficiently, which makes them less likely to develop large temperature gradients than optically thick atmospheres.

5. Rapid rotation ($a^2/L_{Ro}^2 \gtrsim 1$) only has a strong influence on temperature structure if the wave-to-radiative timescale exceeds the above ratio, $t_{wave}/t_{rad} \gtrsim \mathcal{O}(10^{-2})$. Once rotation is important its effects cannot be ignored for a detailed understanding of a planet's atmosphere, including its thermal phase curve signature and the potential for atmospheric collapse.

6. Short-period rocky exoplanets with high MMW atmospheres and surface pressures of $\lesssim 1$ bar will likely exhibit significant day-night temperature gradients. Thermal phase curve observations of such planets will require similar amounts of *JWST* time as transit observations.

CHAPTER 4

ENTROPY BUDGET CONSTRAINS GENERAL CIRCULATIONS OF DRY ATMOSPHERES

It is well-known that Earth's atmosphere resembles a heat engine but this insight has yet to be quantitatively extended to other planets. One obstacle in doing so arises from the many effects caused by moisture, which are important in the context of understanding present-day Earth and which are the subject of ongoing research. A wide range of atmospheres are essentially dry, however, such as Snowball Earth climates, Mars, and desiccated terrestrial exoplanets. Here we address the extent to which dry atmospheres can be understood as planetary heat engines. We diagnose the entropy budget of an idealized general circulation model (GCM) for tidally locked, slowly rotating, and rapidly rotating planets, and study how it varies with optical thickness. We find that dry atmospheres primarily produce entropy through convection, that is, through turbulent vertical transport of heat, whereas the entropy produced by horizontal motions is relatively small. We develop scaling relations to explain this behavior, and show that dry atmospheres can be understood as heat engines for which maintaining the vertical temperature structure lowers an atmosphere's ability to generate horizontal motions. Furthermore, because our scaling relations constrain the entropy production necessary to maintain the vertical temperature structure, we can predict the frictional dissipation of horizontal motions and thus mean surface winds. Our results demonstrate that the entropy budget allows quantitative insight into the circulations of diverse planetary atmospheres, such as colder climates of Earth and the climates of terrestrial exoplanets.

4.1 Introduction

Earth's atmosphere resembles a heat engine. Similar to the Carnot cycle the atmosphere absorbs heat near the surface, at a hot temperature, and emits heat to space in the upper troposphere, at a cold temperature; this process allows the atmosphere to perform work and thus generate the kinetic energy that drives winds and weather (Carnot, 1824). Unlike the Carnot cycle, which is reversible, the atmospheric circulation has to continuously balance irreversible processes such as friction, which would otherwise cause all motion to cease (Lorenz, 1955).

The balance between differential heating and irreversible processes is quantified through the atmosphere's entropy budget (Peixoto et al., 1991). In steady state the entropy emitted to space via radiative fluxes has to equal the entropy absorbed by the atmosphere via surface heat fluxes plus the entropy produced within the atmosphere via irreversible processes. For Earth's present-day climate, the balance between these processes has been explored using a wide range of methods, including observational estimates (Peixoto et al., 1991; Goody, 2000; Pauluis & Dias, 2012), theoretical calculations (Renno & Ingersoll, 1996; Emanuel & Bister, 1996), radiative-convective equilibrium (RCE) simulations (Pauluis et al., 2000; Pauluis & Held, 2002; Romps, 2008), and general circulation models (GCMs; Goody, 2000; Kleidon et al., 2003; Pascale et al., 2011; Laliberté et al., 2015).

One important result of these efforts is that Earth's hydrological cycle is also irreversible and produces entropy through friction acting on raindrops, irreversible phase changes (e.g., by evaporating liquid water into sub-saturated air), and diffusion of water vapor (Pauluis et al., 2000; Pauluis & Held, 2002). Although it is difficult to measure the effect of the hydrological cycle directly, estimates based on GCMs indicate that Earth's atmospheric heat engine is relatively inefficient and only produces two-thirds as much work as an equivalent dry atmosphere (Laliberté et al., 2015). Understanding how Earth's atmospheric heat engine will change in the near future due to anthropogenic warming therefore requires a detailed understanding of the irreversibilities associated with the hydrological cycle, and research into this topic is still ongoing (Pauluis & Held, 2002; Romps, 2008; Laliberté et al., 2015; Singh & O'Gorman, 2016).

There are, however, a wide range of atmospheres for which the effects of water vapor and condensation are negligible. Because the amount of water vapor generally decreases with global-mean temperature, the effect of water vapor tends to be less important in colder climates and would have been virtually absent in Earth's atmosphere during past Snowball Earth episodes (Pierrehumbert et al., 2011; Voigt et al., 2012; Voigt, 2013). Similarly, the entropy production associated with irreversible phase changes disappears once an atmosphere is fully saturated (Pauluis, 2010), which suggests that steam atmospheres of runaway greenhouse climates could also resemble dry heat engines. Finally, recent astronomical discoveries imply there is about one rocky extrasolar planet per star in the galaxy (Dressing & Charbonneau, 2015) and next-generation telescopes will be able to study the atmospheres of these planets within the next three years (Koll & Abbot, 2015; Kreidberg & Loeb, 2016). Many of these atmospheres could in turn be dry due to photodissociation and water loss to space, similar to how Venus is thought to have lost its water (Ingersoll, 1969; Wordsworth & Pierrehumbert, 2013; Barnes et al., 2016; Ribas et al., 2016). In the case of dry convection, the entropy budget constrains the overall strength of convection (Renno & Ingersoll, 1996; Emanuel & Bister, 1996; Pauluis & Held, 2002). By extension one would expect the entropy budget to provide insight into the circulations of dry atmospheres, but this has not yet been explicitly demonstrated.

As a first step towards a general understanding of planetary atmospheres as heat engines, we recently showed that the large-scale circulations of dry and tidally locked planets act very similar to ideal heat engines (Koll & Abbot, 2016). A tidally locked and dry atmosphere, we showed, is driven by the thermal contrast between the hot dayside and the cold radiative emission level, which allowed us to formulate an upper bound for how much work a tidally locked atmosphere can produce. Assuming that this work is entirely used to balance turbulent friction acting on the day-night circulation, we were able to successfully put an upper bound on the large-scale wind speeds of tidally locked planets, allowing us to further constrain their day-night mass fluxes and heat transports. Our previous work did not address why some atmospheres developed significantly lower wind speeds than ideal heat engines, however, and it also did not show how our theory could be extended to other types of circulations.

To address these questions we consider here the entropy budget of a wide range of atmospheric circulations in an idealized GCM, and how it changes in response to changes in optical thickness (Section 4.2). We find that dissipation of vertical turbulence and convective mixing of heat generally dominates the entropy budget of dry atmospheres whereas dissipation of large-scale horizontal motions is a comparatively minor term (Section 4.3). Nevertheless, the entropy production via vertical turbulence can be constrained. This allows us to place strong constraints on the entropy production via horizontal motions and therefore predict the strength of surface winds over a wide range of dry atmospheres (Section 4.3). To finish we discuss our results in the context of the climates of Snowball Earth and of Mars (Section 4.4).

4.2 Model and Simulations

We use the FMS GCM with grey radiative transfer. The model was previously described in Frierson et al. (2006) and O'Gorman & Schneider (2008); we modify it as follows. We specify a longwave optical thickness τ that is spatially uniform and increases quadratically in pressure,

$$\tau = \tau_{LW} \times \left(\frac{p}{p_s}\right)^2, \tag{4.1}$$

where τ_{LW} is the surface optical thickness, p is the pressure, and p_s is the surface pressure. This means we treat the longwave absorber as a generic pressure-broadened greenhouse gas. Similarly, we do not include atmospheric shortwave absorption, which, in Earth's current atmosphere, is in great part due to water vapor (Biagio et al., 2012). We set the gas constant and heat capacity of dry air equal to those of N_2. Without atmospheric solar absorption the surface albedo and the solar constant are degenerate. We set the albedo to zero and the solar constant equal to 952 W m^{-2}, which results in an Earth-like equilibrium temperature of $T_{eq} = 255$ K. As in Frierson et al. (2006), we make the GCM dry by reducing the saturation vapor pressure constant in the model's Clausius-Clapeyron relation from $e_0 = 610.70$ Pa to $e_0 = 610.70 \times 10^{-20}$ Pa.

We consider the entropy budget and how it responds to changes in optical thickness (τ_{LW}) for three different circulation geometries. First, we consider an Earth-like planet with Earth-like insolation and rotation period. In this case the atmosphere develops the familiar pattern of a low-latitude Hadley circulation and high-latitude baroclinic eddies. Second, we consider a slowly rotating planet with Earth-like insolation and a rotation period of 50 days. The slow rotation causes the Hadley cell to extend almost to the poles, analogous to the circulations of Venus and Titan (Del Genio & Suozzo, 1987; Mitchell et al., 2009) and the hypothesized Hadley circulation on Earth during the Eocene (Farrell, 1990). Third, we consider a tidally locked planet with a tidally locked insolation pattern and a rotation period of 50 days, which is characteristic of a rocky planet in the habitable zone of an early M-dwarf star (Kopparapu et al., 2016). The slow rotation combined with the zonally asymmetric forcing create a thermally direct circulation between dayside and nightside, analogous to a global Walker circulation (Joshi et al., 1997; Merlis & Schneider, 2010; Koll & Abbot, 2016).

The production of entropy in a dry atmosphere is ultimately always due to friction and diffusion acting on a molecular scale. On the spatial scales of an atmosphere, however, it is advantageous to separate between the entropy produced by friction and diffusion acting on small-scale vertical turbulent motions versus large-scale horizontal motions. We write the entropy budget for a dry atmosphere as (cf. Pauluis & Held, 2002; Kleidon et al., 2003; Romps, 2008; Fraedrich & Lunkeit, 2008; Pascale et al., 2011)

$$\dot{s}_{rad} \quad = \quad \dot{s}_{surf} + \dot{s}_{fric} + \dot{s}_{mix} + \dot{s}_{num}. \tag{4.2}$$

On the left hand side is the entropy sink by radiative cooling $\dot{s}_{rad}$. On the right hand side are the entropy sources via surface heat fluxes $\dot{s}_{surf}$, frictional dissipation of large-scale horizontal motions $\dot{s}_{fric}$, vertical turbulent mixing of heat $\dot{s}_{mix}$, and explicit numerical entropy sources $\dot{s}_{num}$. Turbulent mixing, $\dot{s}_{mix}$, is the result of motions which act to vertically redistribute heat but which are too small to be explicitly resolved. In the GCM these motions are parametrized using a quasi-equilibrium convection scheme (Frierson, 2007; O'Gorman & Schneider, 2008) as well as a boundary layer turbulence scheme (Frierson et al., 2006). We note that $\dot{s}_{mix}$ should be thought of as the combined effect of diffusion as well as friction acting on turbulent (unresolved) motions, whereas $\dot{s}_{fric}$ only includes friction acting on large-scale (explicitly resolved) motions (Pauluis & Held, 2002). The GCM has two potential sources of large-scale friction: boundary layer friction and numerical damping by the model's hyperviscosity. In practice we find that the entropy production due to numerical damping is negligible, so we only include the boundary layer friction in $\dot{s}_{fric}$. The term $\dot{s}_{num}$ accounts for explicit entropy changes in the model's numerics, which arise from the model's hyperdiffusion of temperature and a global temperature and humidity correction which makes up for model shortcomings in conserving energy and water vapor. Following Pauluis & Held (2002) we combine the external sources and sinks of heat into a net entropy sink $\dot{s}_{sink} = \dot{s}_{rad} - \dot{s}_{surf}$. The entropy budget then states that the entropy sink due to the atmosphere's differential heating has to be balanced by the atmosphere's internal entropy production via irreversible processes,

$$\dot{s}_{sink} \quad = \quad \dot{s}_{fric} + \dot{s}_{mix} + \dot{s}_{num}. \tag{4.3}$$

To diagnose the sources and sink in the GCM, we start with the change of entropy ds per unit mass of air, which can be written as $ds = c_p dT/T - dp/(\rho_d T)$ (cf. Emanuel, 1988), where c_p is the specific heat capacity, T is the temperature, ρ_d is the density, and p is the pressure. Next, we write $\dot{s} = ds/dt$, so

$$\dot{s} \;=\; c_p \frac{\dot{T}_i}{T} - \frac{1}{T}\frac{\dot{p}_i}{\rho_d}, \tag{4.4}$$

where $\dot{T}_i$, and $\dot{p}_i$ are temperature and pressure tendencies computed in the GCM. We compute the sources and sinks in the entropy budget (Equation 4.3) from the mass-weighted vertical and global average of $\dot{s}$ (Equation 4.4), which we denote using angular brackets. In the GCM radiative heating and cooling only affects temperature, so $\dot{s}_{rad} = \langle c_p \dot{T}_{rad}/T \rangle$. We similarly compute the entropy produced via frictional dissipation through the heating it induces, $\dot{s}_{fric} = \langle c_p \dot{T}_{fric}/T \rangle$. The entropy produced by turbulent mixing of heat, $\dot{s}_{mix}$, can be inferred by writing the first term in Equation 4.4 as the convergence of a convective heat flux, $c_p \dot{T}/T = -(\nabla \cdot F_{conv})/T$. We separate this term into surface and internal contributions,

$$\begin{aligned}
\left\langle \frac{\nabla \cdot F_{conv}}{T} \right\rangle &= \left\langle \nabla \cdot \left(\frac{F_{conv}}{T} \right) \right\rangle - \left\langle F_{conv} \cdot \nabla \left(\frac{1}{T} \right) \right\rangle, \\
\left\langle \frac{\nabla \cdot F_{conv}}{T} \right\rangle &= \left\langle \frac{F_{conv}}{T_s} \right\rangle_{surf} + \left\langle \frac{F_{conv} \cdot \nabla T}{T^2} \right\rangle, \\
\dot{s}_{conv} &= \dot{s}_{surf} + \dot{s}_{mix},
\end{aligned} \tag{4.5}$$

where we have used Gauss' theorem in the second step. We then infer the entropy produced via mixing as $\dot{s}_{mix} = \dot{s}_{conv} - \dot{s}_{surf} = \langle c_p \dot{T}_{conv}/T \rangle - \dot{s}_{surf}$, where $\dot{T}_{conv}$ is the temperature tendency produced by convective parametrizations. The second term in Equation 4.4 is the work performed by a parcel of air on its environment. In a hydrostatic atmosphere this term is proportional to a parcel's vertical motion. In the GCM diabatic forcings modify $\dot{T}$ but do not directly induce vertical motion, so in practice we do not include the second term.

4.3 Constraining the circulation strength

Our diagnostic accurately captures the entropy production in our simulations. Figure 4.1 shows the global-mean entropy budget in the three types of simulations as the atmosphere's

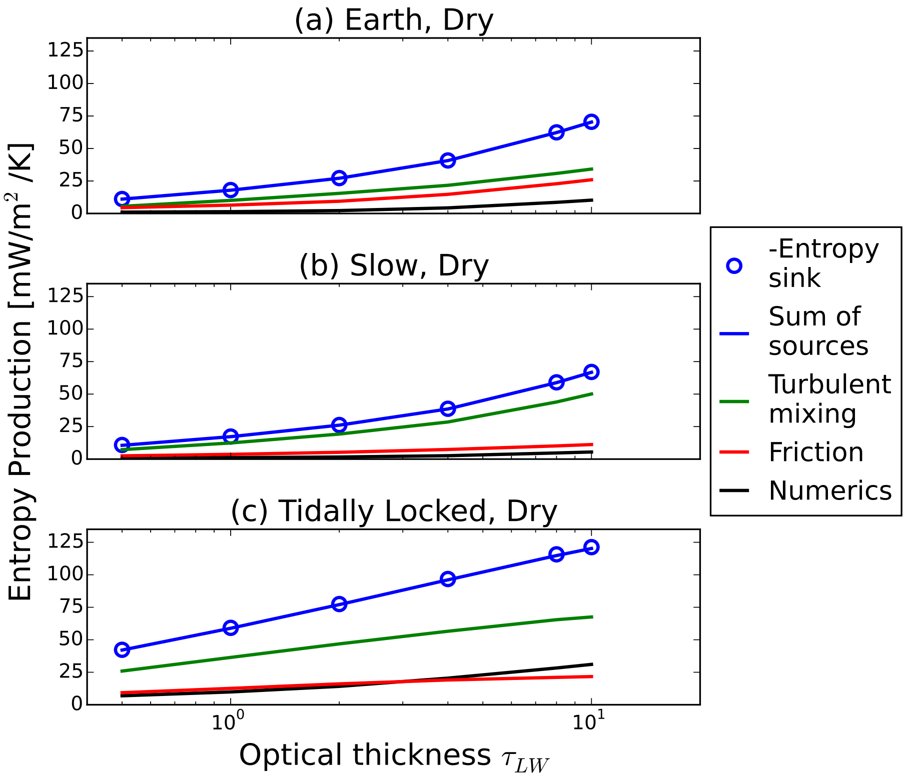

Figure 4.1: Entropy budget as optical thickness (τ_{LW}) is increased. (a) Simulations with Earth-like insolation and rotation rate. (b) Earth-like insolation and slow rotation (50 day rotation period). (c) Tidally locked insolation and slow rotation (50 day rotation period). Turbulent mixing of heat dominates the entropy budget whereas frictional dissipation of large-scale kinetic energy is a relatively minor term, particularly for slowly rotating atmospheres (b and c).

optical thickness (τ_{LW}) is increased. The imbalance between the net entropy sink $\dot{s}_{sink}$ (blue circles) and the sum of entropy sources (blue lines) is slightly less than 3% of $\dot{s}_{sink}$ in one simulation, and less than 1% in all other simulations. The entropy imbalance tends to be largest in optically thin simulations with $\tau_{LW} < 1$ and is most likely due to the GCM's imperfect energy conservation. For example, the slowly rotating simulation with $\tau_{LW} = 0.5$ has the largest relative entropy imbalance and emits ~ 0.06 W m^{-2} more energy to space than it absorbs. If this energy surplus did not drive any irreversible processes but was emitted at the equilibrium temperature (255 K) it would cause an artificial entropy sink of ~ 0.2mW m^{-2} K^{-1}, which compares well with the simulation's actual shortfall of 0.26 mW m^{-2} K^{-1}.

Turbulent mixing, $\dot{s}_{mix}$, dominates the entropy budget in all simulations (Figure 4.1), underscoring the fact that dry atmospheres produce entropy primarily through vertical, as opposed to horizontal, redistribution of heat (cf. Pascale et al., 2012). The ratio between $\dot{s}_{fric}$ and $\dot{s}_{mix}$ depends on circulation geometry and is largest for Earth-like atmospheres (Fig. 4.1a). This is because the vertical temperature structure in the extratropics of rapidly rotating planets is maintained by large-scale eddies (Schneider & O'Gorman, 2008; Jansen & Ferrari, 2013), which in turn are captured by $\dot{s}_{fric}$, whereas slowly rotating planets resemble Earth's tropics and maintain their vertical temperature structure through small-scale turbulence, that is, convection. Nevertheless, $\dot{s}_{mix}$ is the largest term in the entropy budget across all simulations. Understanding the entropy budget of the large-scale circulation therefore requires a theory for the entropy produced via turbulent mixing, which we develop below. Figure 4.1 also shows that the numerical entropy production $\dot{s}_{num}$ can be significant, particularly for tidally locked simulations in the optically thick limit. We find that $\dot{s}_{num}$ is dominated by the model's energy correction term whereas hyperdiffusion is negligible, which again points to imperfect energy conservation by the model's large-scale dynamics.

First we address the entropy sink $\dot{s}_{sink} = \dot{s}_{rad} - \dot{s}_{surf}$. We assume that horizontal temperature differences in the atmosphere are small compared to vertical temperature differences. Although present-day Earth does not quite satisfy this assumption (Peixoto & Oort, 1992), it is satisfied on slowly rotating planets as well as rapidly rotating planets with optically thick atmospheres, such as ancient Earth with higher CO_2 concentrations. Using this assumption we will relate the terms in the entropy budget back to suitably averaged mean quantities (see below). The entropy produced by surface heat fluxes is $\dot{s}_{surf} = F_{conv}(p_s)/T_s$, where $F_{conv}(p_s)$ is the surface heat flux, p_s is the surface pressure, and T_s is the surface temperature. The entropy removed by radiative cooling is $\dot{s}_{rad} = \int \nabla \cdot F_{rad}/T dp$, where F_{rad} is the net radiative flux, p is pressure, and T is temperature. Atmospheric energy balance requires that radiative cooling balances the surface heat flux, $\int \nabla \cdot F_{rad} dp = F_{conv}(p_s)$, so the entropy sink scales as (see Pauluis & Held, 2002; Singh & O'Gorman, 2016)

$$\dot{s}_{sink} \sim F_{conv}(p_s)\left(\frac{1}{T_{rad}} - \frac{1}{T_s}\right), \tag{4.6}$$

where T_{rad} is the average temperature at which radiative cooling takes place. As optical thickness increases and the surface can shed less energy via longwave radiation, the surface energy budget requires that $F_{conv}(p_s)$ has to increase; consequently, Equation 4.6 explains why the entropy sink increases with optical thickness (Fig. 4.1). Next, we specify T_{rad} by considering its behavior in the optically thick and thin limits. In the optically thick limit radiative cooling occurs mainly around the emission level (Pierrehumbert, 2011b), so $T_{rad} \sim T_{eq}$ where T_{eq} is the equilibrium temperature. In the optically thin limit radiative cooling takes place over the entire atmosphere, so $T_{rad} \sim \langle T \rangle$. We combine these two limits as $T_{rad} = min(T_{eq}, \langle T \rangle)$. Figure 4.2a compares Equation 4.6 with the entropy sink in the GCM. For simulations with Earth-like insolation we use the global average of T_s and $F_{conv}(p_s)$. On tidally locked planets $F_{conv}(p_s)$ coincides with the turbulent hot dayside, whereas inversions suppress turbulence on the nightside (Merlis & Schneider, 2010; Koll & Abbot, 2016), so we only use the dayside average of T_s. We find that, up to a constant, Equation 4.6 provides an excellent fit to the entropy sink in our dry simulations.

We address the entropy production by turbulent mixing next, again assuming that horizontal variations are much smaller than vertical variations. In this case convection produces entropy at a rate $\dot{s}_{mix} = \int F_{conv}(p)(dT/dp)/T^2 dp$ (Equation 4.5). If F_{conv} is constant up to some convective outflow pressure p_{top} and zero above, such that the entire convective heat flux is deposited at p_{top}, then $\dot{s}_{mix}$ scales as

$$\dot{s}_{mix} \sim F_{conv}(p_s)\int_{p_{top}}^{p_s} \frac{dT/dp}{T^2} dp. \tag{4.7}$$

Next, assuming convection is efficient at maintaining a dry adiabat, $T(p) = T_s(p/p_s)^{R/c_p}$,

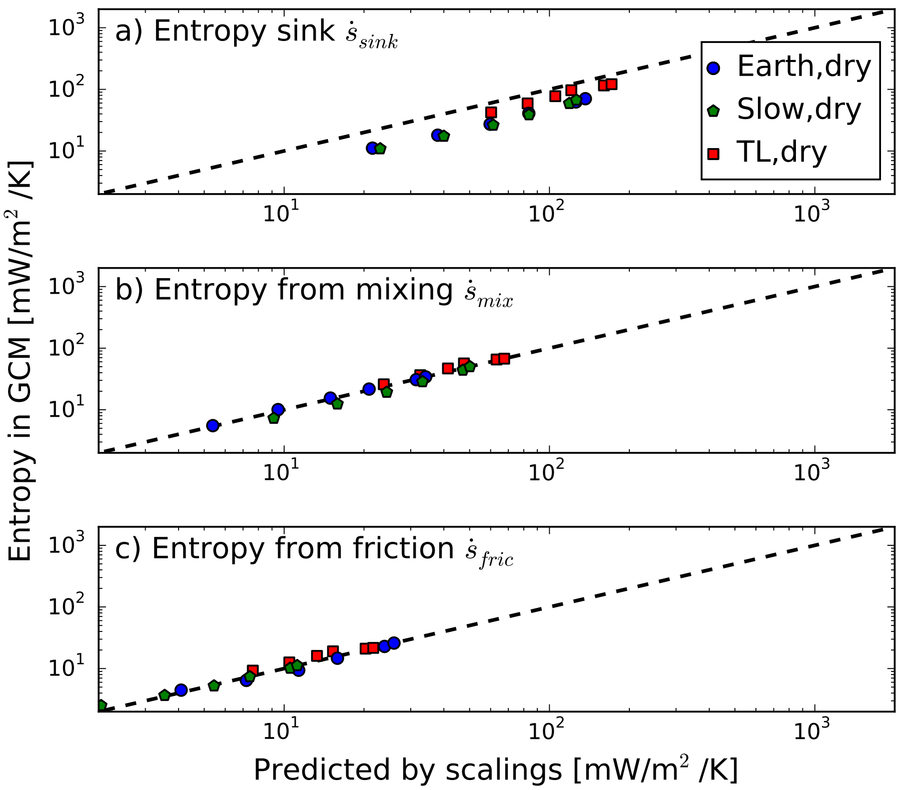

Figure 4.2: Our scalings capture the dominant terms in the entropy budget. Shown are results from the GCM (y-axes), compared with their predicted magnitudes (x-axes). Top: Entropy sink due to the atmosphere's differential heating. Middle: Entropy source due to turbulent mixing of heat. Bottom: Entropy source due to frictional dissipation of large-scale kinetic energy.

the lapse rate is given by $dT/dp = RT/(c_p p)$. We arrive at

$$\begin{aligned}
\dot{s}_{mix} \sim & \quad \frac{R}{c_p} F_{conv}(p_s) \int_{p_{top}}^{p_s} \frac{1}{T(p)p} dp, \\
= & \quad \frac{R}{c_p} \frac{F_{conv}(p_s)}{T_s} p_s^{R/c_p} \int_{p_{top}}^{p_s} p^{-(R/c_p+1)} dp, \\
= & \quad \frac{R}{c_p} \frac{F_{conv}(p_s)}{T_s} p_s^{R/c_p} \left[\frac{(-1)}{R/c_p} p^{-R/c_p} \right]_{p_{top}}^{p_s}, \\
\dot{s}_{mix} \sim & \quad \frac{F_{conv}(p_s)}{T_s} \left[\left(\frac{p_s}{p_{top}} \right)^{R/cp} - 1 \right]. \qquad (4.8)
\end{aligned}$$

	k_1	k_2
Earth	0.25	0.19
Slowly rotating	0.39	0.09
Tidally locked	0.39	0.12

Table 4.1: Fitting constants used in our scaling relations.

To close Equation 4.8 we have to specify p_{top}. The deepest extent of convection is from the surface up to the radiative emission level, that is, from the surface temperature T_s up to the radiative temperature T_{rad}. Because the temperature structure is assumed to be adiabatic, T_{rad} can be expressed as $T_{rad} = T_s(p_{top}/p_s)^{R/c_p}$. Equation 4.8 will give an overestimate of the entropy produced by mixing because in reality the convective heat flux F_{conv} is not constant in height and has to diminish to balance radiative and large-scale advective cooling. To account for this vertical structure we multiply Equation 4.7 by a fitting constant, which has to be less than one and which we choose to match $\dot{s}_{mix}$ in the optically thick limit for each set of simulations (we chose the simulations at $\tau_{LW} = 10$). We arrive at

$$\dot{s}_{mix} = k_1 F_{conv}(p_s)\left(\frac{1}{T_{rad}} - \frac{1}{T_s}\right), \tag{4.9}$$

which is the same scaling relation as for $\dot{s}_{sink}$ but multiplied by the fitting constant k_1. The constant varies between 0.25 and 0.39 in our dry simulations (Table 4.1). Figure 4.2b compares Equation 4.9 with the entropy from turbulent mixing in our dry GCM simulations. Given the simplicity of the scaling, the fit in Figure 4.2b is very good and shows that the entropy production by turbulence can be largely determined from first principles. This is important, because we did not make any assumptions about the nature of turbulent mixing nor how it is parametrized in the GCM. This implies that, as long as convection is efficient at keeping the atmospheric temperature profile close to an adiabat, variations in $\dot{s}_{mix}$ are largely constrained by energetics.

We now combine our scalings to constrain the entropy production by frictional dissipation,

$\dot{s}_{fric}$. From Equations 4.3, 4.6, and 4.9, we find

$$\begin{aligned} \dot{s}_{fric} &\sim (1 - k_1)\dot{s}_{sink}, \\ \dot{s}_{fric} &= k_2 F_{conv}(p_s) \left(\frac{1}{T_{rad}} - \frac{1}{T_s} \right), \end{aligned} \tag{4.10}$$

where k_2 is another fitting constant which accounts for the fact that our scaling for $\dot{s}_{sink}$ is an overestimate and for the numerical entropy source $\dot{s}_{num}$, which also scales with $\dot{s}_{sink}$ (Fig. 4.1). We compare Equation 4.10 with our dry GCM simulations in Figure 4.2c. Our scaling is able to match the GCM results. The frictional dissipation $\dot{s}_{fric}$ in the simulations varies by more than one order of magnitude, and our scaling correctly captures this variation. Our result is highly encouraging because we only assumed that horizontal temperature gradients are small compared with vertical temperature gradients, and made no explicit assumptions about the horizontal structure of the atmospheric circulation. This raises the question of how $\dot{s}_{fric}$ can be used to characterize a planet's atmosphere, which we address next.

The rate at which kinetic energy is dissipated by friction is equal to $\mathbf{F} \cdot \mathbf{v}$, where $\mathbf{F}$ is the drag force acting on a parcel of air and $\mathbf{v}$ is its velocity (Emanuel & Bister, 1996; Pauluis et al., 2000). On rocky planets friction is largely caused by turbulent dissipation in the boundary layer (cf. Chai et al., 2016), which we idealize as a thin layer directly above the surface. Using standard bulk exchange coefficients, the drag acting on a parcel of air is therefore $\mathbf{F} = \rho_s C_D U_s^2$ where ρ_s is the surface air density, C_D is the drag coefficient, and U_s is the wind speed at the surface. This means the net entropy production due to friction scales as $\dot{s}_{fric} \sim (\mathbf{F} \cdot \mathbf{v})/T_s \sim \rho_s C_D U_s^3/T_s$. To constrain the drag coefficient we assume a neutrally stable convective layer, $C_D = k_{vk}^2/log(z_0/z_*)$, where k_{vk} is the von Kármán constant, $z_0 = 10$ m, and z_* is the surface roughness length (our simulations use $z_* = 10^{-3}$m). Although this is a simplification because the drag coefficient varies locally depending on stratification, the dependence is not strong and neutral stratification is a reasonable first-order assumption.

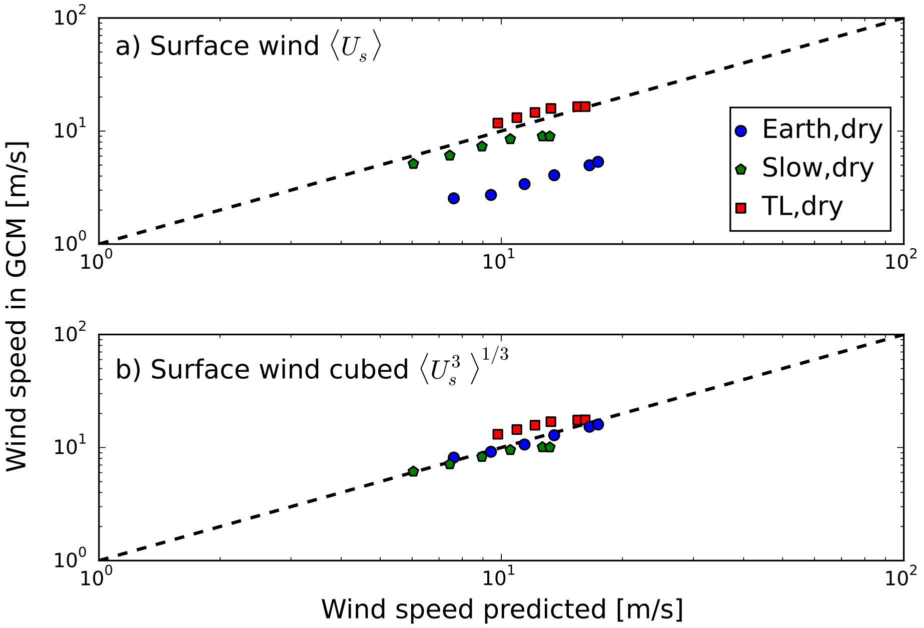

Figure 4.3: In dry atmospheres, average wind speeds in the GCM (y-axes) follow our scaling for frictional dissipation (x-axis). Top: mean surface wind speed $\langle U_s \rangle$. Bottom: cube-root of the surface wind speed cubed, $\langle U_s^3 \rangle^{1/3}$. In steady circulations, such as on slowly rotating planets (green symbols), $\langle U_s \rangle \approx \langle U_s^3 \rangle^{1/3}$, whereas eddy-driven variability on Earth-like planets (blue symbols) causes $\langle U_s \rangle < \langle U_s^3 \rangle^{1/3}$.

We can then use the entropy budget to constrain the surface wind speed scale,

$$U_s^3 = k_2 \frac{F_{conv}(p_s)}{\rho_s C_D} T_s \left(\frac{1}{T_{rad}} - \frac{1}{T_s} \right). \tag{4.11}$$

Figure 4.3a shows that average surface wind speeds in the GCM $\langle U_s \rangle$ indeed follow our predicted scaling. Similar to above, for planets with Earth-like insolation we use the global average of T_s whereas for tidally locked planets we only use a dayside average. For slowly rotating and tidally locked planets our scaling captures the average surface wind speed well, whereas for Earth-like planets our scaling overestimates wind speeds by about a factor of four. The overestimate for rapidly rotating planets is due to atmospheric variability. Slowly rotating planets are characterized by steady circulations whereas Earth-like planets possess extratropical storm tracks. Within the storm tracks, eddies create time-varying wind speeds so that the average of the surface wind is smaller than the normalized average of the surface wind cubed, $\langle U_s \rangle < \langle U_s^3 \rangle^{1/3}$. If we compare our scaling with the normalized average of the surface wind cubed instead, $\langle U_s^3 \rangle^{1/3}$, we find a good fit for all GCM simulations (Fig. 4.3b). To the extent that changes in dissipation on Earth-like planets also occur largely within the storm tracks, this means that the entropy budget could also be used to constrain how mid-latitude weather systems respond to changes in radiative forcing.

Finally, Equation 4.11 can be interpreted analogous to the Carnot cycle but with a reduced efficiency due to the vertical redistribution of heat by turbulence. The work done to balance friction is $W_{fric} = \rho_s C_D U_s^3$, so

$$\begin{aligned} W_{fric} &= F_{conv}(p_s) \times k_2 T_s \left(\frac{1}{T_{rad}} - \frac{1}{T_s} \right), \\ &= F_{conv}(p_s) \times k_2 \left(\frac{T_s - T_{rad}}{T_{rad}} \right), \\ &= F_{conv}(p_s) \times \eta, \end{aligned} \tag{4.12}$$

where $\eta = k_2(T_s - T_{rad})/T_{rad}$ is the efficiency of the general circulation. In comparison, the work done by an equivalent Carnot cycle is $W = F_{conv}(p_s) \times \eta_{Carnot} = F_{conv}(p_s) \times (T_s - T_{rad})/T_s$, which differs from Equation 4.12 only through its intake temperature. Unlike the Carnot cycle's intake temperature, T_s, vertical turbulence and heat redistribution lowers the intake temperature of the general circulation to T_{rad}/k_2. For Earth-like planets k_2 is approximately equal to k_1 (Table 4.1), so the intake temperature is set by the vertical structure of the convective heat flux. For tidally locked and slowly rotating planets k_2 is smaller than k_1 because k_2 also accounts for the numerical entropy production, which is larger on slowly rotating than on Earth-like planets (Fig. 4.1). This means numerical adjustments act to further reduce the production of work by the general circulation. Carnot's theorem requires that $\eta \leqslant \eta_{carnot}$, or $k_2/T_{rad} \leqslant 1/T_s$, which we find is satisfied in all our simulations.

4.4 Discussion

In previous work we showed that dry and tidally locked atmospheres tend to resemble heat engines which balance friction and drive large-scale horizontal motions, but we also found that some atmospheres develop significantly weaker wind speeds than expected (Koll & Abbot, 2016). Our results here explain why: instead of performing work purely to balance friction acting on horizontal motions, atmospheres also need to vertically transport and mix heat to maintain their vertical temperature structure. Although this process has to be parametrized in GCMs as a vertical diffusion of heat or a relaxation back towards an adiabatic temperature profile (the GCM we use includes both processes), it closely captures the general behavior of dry convection (Emanuel et al., 1994) so we expect our result to be robust.

We also find that frictional dissipation of large-scale kinetic energy mainly scales with the surface heat flux $F_{conv}(p_s)$ (Eqn. 4.12). Increasing an atmosphere's optical thickness reduces the surface's ability to shed longwave radiation and therefore increases $F_{conv}(p_s)$. This would affect past Snowball episodes, which deglaciated due to a massive buildup of volcanic CO_2 (Hoffman et al., 1998). Because more CO_2 implies a higher optical thickness, our results imply that Snowball surface winds should have been strongest right before deglaciation. This means the wind stress acting on sea ice and the aeolian transport of dust would also have been strongest right before deglaciation, which in turn could affect the duration and timing of Snowball episodes (Abbot & Pierrehumbert, 2010; Abbot & Halevy, 2010; Voigt & Abbot, 2012).

Similarly, our scalings suggest that ancient Mars would have had more frequent dust storms than today. Present-day Mars only supports an optically thin atmosphere whereas ancient Mars must have had at least a transiently thicker atmosphere to explain the geologic features of present-day Mars (Wordsworth, 2016). We estimate an optical thickness of $\tau_{LW} \sim 0.2$ for Mars's current solar constant of about $L_* = 585$ W m^{-2}, whereas τ_{LW} would have exceeded unity on ancient Mars when the solar constant was about 80% as high. Assuming that $F_{conv}(p_s)$ in optically thin atmospheres scales as $\sim \tau_{LW} L_*$ entails that the global-mean frictional dissipation $\dot{s}_{fric}$ on ancient Mars would have been higher by about a factor of four. Given that this would have increased the average atmospheric drag exerted on the surface by the same amount, we expect that thicker atmospheres on Mars would have initiated dust storms more frequently.

Our conclusions could be influenced by physical processes other than the ones considered here. In particular, we do not include atmospheric absorption of solar radiation but this could occur through dust or photochemical hazes, which could have developed in the anoxic atmosphere of early Earth (Pavlov et al., 2001). Following Equation 4.6, solar absorption would reduce the atmospheric entropy production because it reduces the magnitude of the entropy sink by decreasing the surface heat flux $F_{conv}(p_s)$ and increasing the effective temperature of radiative cooling T_{rad}.

4.5 Conclusions

Our main conclusions are:

- The entropy budget of dry atmospheres is dominated by convection, that is, small-scale turbulence which acts to vertically mix heat. Relatively less entropy is produced by dissipation of kinetic energy in large-scale horizontal motions.

- The entropy production by turbulent mixing depends on the magnitude of surface heat fluxes and the depth over which convection redistributes them. Convection approximately extends from the surface up to the radiative emission layer, which allows us to constrain the entropy production necessary for maintaining an atmosphere's vertical temperature structure.

- Once the entropy production necessary for maintaining the atmosphere's vertical temperature is known, the residual term in the entropy budget is the entropy production by large-scale horizontal motions. Our scalings constrain this term and capture the variability of surface winds across a wide range of dry atmospheres.

CHAPTER 5

SUMMARY AND OUTLOOK

In this thesis we have developed a series of theoretical models for understanding the atmospheric dynamics of dry and rocky exoplanets, and have connected the dynamics of extrasolar atmospheres back to atmospheres in the Solar system. Although the appendices are auxiliary to this thesis they include a systematic nondimensionalization of the atmospheric equations of motion and a derivation of a coordinate system appropriate for tidally locked atmospheres, which can be used in further studies.

To summarize our takeaway points for planetary atmospheres:

- The large-scale dynamics of planetary atmospheres can be captured by a tractably small number of non-dimensional parameters.
- Dry and tidally locked atmospheres develop deep turbulent boundary layers. Weak-temperature-gradient theories apply on the nightside of tidally locked planets, but break down on their daysides. Understanding the dayside is critical for understanding the day-night circulation of these atmospheres.
- The atmospheres of tidally locked planets resemble planetary heat engines. These atmospheres absorb heat on the dayside and emit it to space at the radiating level, which allows them to balance frictional dissipation on the dayside.
- Small-scale vertical turbulence in the form of convection reduces the production of large-scale kinetic energy. In contrast to hot Jupiters, whose upper atmospheres are radiatively dominated and generally stable against convection, we expect that many rocky planets have convecting atmospheres. This means rocky exoplanets should posses atmospheric dynamics that are distinct from the already-observed dynamics of hot Jupiters; future observations will allow us to compare the two.

Finally, the coming years will see a new generation of space telescopes launched to explore the atmospheres of rocky exoplanets. Looking towards the discoveries that will be made by these instruments, in particular by the *James Webb Space Telescope* (*JWST*), some of our takeaway points for observations are:

- The observable thermal phase curve signatures of rapidly rotating and slowly rotating rocky planets are distinct. For planets on long-period orbits (which includes the habitable zone of early M-dwarfs), the main phase curve signature is the peak-to-trough amplitude.

- Rocky planets that are rapidly rotating also need to be sufficiently hot or have sufficiently thin atmospheres to exhibit the strong equatorial superrotation and large eastward hotspot offsets known from hot Jupiters. For moderately hot planets like GJ 1132b with high mean-molecular-weight atmospheres (that is, not hydrogen), the surface pressure threshold is $\mathcal{O}(1)$ bar.

- Planets with hydrogen atmospheres exhibit significantly smaller temperature gradients than planets with high mean-molecular-weight atmospheres. These atmospheres would exhibit large spectral features in transit, while their thermal phase curves would be relatively flat.

- Thermal phase curves by themselves are ambiguous to interpret, but combined with transit spectra they constrain a planet's surface pressure. If a planet's transit spectrum is well-characterized, a single broadband thermal phase curve with *JWST* could be sufficient to constrain the atmospheric thickness of a nearby rocky exoplanet.

- Unless the atmospheres of rocky exoplanets are made of hydrogen, constraining their atmospheric composition with *JWST* will require similar amounts of telescope time as measuring their thermal phase curves. Future observation campaigns will ideally budget time to do both.

- In contrast to gas giants, rocky exoplanets can exhibit significant day-night temperature gradients and phase curve amplitudes even inside the habitable zone of their host star.

APPENDIX A

BASIC EQUATIONS

The primitive equations expressed in standard latitude-longitude-pressure coordinates (θ, λ, p) are

$$\begin{aligned}
\frac{D\mathbf{u}}{Dt} &= -2\Omega\sin\theta\mathbf{k}\times\mathbf{u} - \nabla\phi - g\frac{\partial\mathbf{F}_m}{\partial p}, && \text{(A.1a)}\\
\frac{\partial\phi}{\partial p} &= -\frac{RT}{p}, && \text{(A.1b)}\\
\nabla\cdot\mathbf{u} &+ \frac{\partial\omega}{\partial p} = 0, && \text{(A.1c)}\\
\frac{DT}{Dt} &= \frac{RT\omega}{c_p p} + \frac{g}{c_p}\frac{\partial F}{\partial p} + \frac{g}{c_p}\frac{\partial\mathcal{D}}{\partial p}. && \text{(A.1d)}
\end{aligned}$$

Here $\mathbf{u} = (u, v)$ is the horizontal wind velocity, $\frac{D}{Dt} = \frac{\partial}{\partial t} + \mathbf{u}\cdot\nabla + \omega\frac{\partial}{\partial p}$ is the material derivative, $\mathbf{k}$ is a unit vector pointing along the axis of planetary rotation, ϕ is the geopotential, T is temperature, $\omega \equiv \frac{\mathrm{D}p}{\mathrm{D}t}$ is the vertical velocity (expressed as a change in pressure), and dimensional parameters are defined in Section 2.2. From the top, these equations express conservation of momentum, the hydrostatic approximation, conservation of mass, and conservation of energy. Although the mass conservation equation looks like it assumes incompressibility, it does not. The primitive equations are compressible, but mass conservation can be written in the above simple form using p coordinates and the hydrostatic equation

(Vallis, 2006, p.79). The forcing terms are

$$
\begin{aligned}
F &= F_{LW}^{\uparrow} - F_{LW}^{\downarrow} - F_{SW}^{\downarrow}, \\
\frac{\partial F_{LW}^{\uparrow}}{\partial p} &= \frac{2\kappa_{lw}}{g}(F_{LW}^{\uparrow} - \sigma_{SB}T^4), \\
\frac{\partial F_{LW}^{\downarrow}}{\partial p} &= -\frac{2\kappa_{lw}}{g}(F_{LW}^{\downarrow} - \sigma_{SB}T^4), \\
\frac{\partial F_{SW}^{\downarrow}}{\partial p} &= -\frac{2\kappa_{sw}}{g}F_{SW}^{\downarrow}, \\
F_{SW}^{\downarrow}|_{p=0} &= \begin{cases} (1-\alpha)L_* \cos\theta\cos\lambda & \text{if } 270^\circ \leqslant \lambda \leqslant 90^\circ \\ 0 & \text{elsewhere,} \end{cases} \\
\mathbf{F}_m|_{p_s} &= \rho_s C_D |\mathbf{u}_s|\mathbf{u}_s, \\
\mathcal{D}|_{p_s} &= \rho_s c_p C_D |\mathbf{u}_s|(T_s - T|_{p_s}).
\end{aligned}
$$

Here $\mathbf{u}_s$ is the surface wind velocity, T_s is the surface temperature, $T|_{p_s}$ is the near-surface air temperature, and ρ_s is the atmospheric density at the surface ($\rho_s = p_s R^{-1} T|_{p_s}$, using the ideal gas law). In addition, convection instantaneously adjusts an unstable lapse rate toward the dry adiabat while conserving dry enthalpy

$$\frac{\mathrm{d}}{\mathrm{d}t}\int_0^{p_s} c_p T \frac{dp}{g} = 0.$$

We neglect scattering in the radiative equations. We assume the hemi-isotropic closure, which is why the radiative equations contain a factor of two (Section 6.4 in Heng et al., 2014). We also assume that opacities increase with p due to pressure broadening and/or collision-induced absorption, so $\kappa_{sw} = \kappa_{SW}(p/p_0)$ and $\kappa_{lw} = \kappa_{LW}(p/p_0)$. We define nondimensional shortwave and longwave optical depths as $d\hat{\tau}_{sw}/dp = 2\kappa_{sw}(p)/g$ and $d\hat{\tau}_{lw}/dp = 2\kappa_{lw}(p)/g$. We integrate to find the total optical depths, $\tau_{SW} \equiv \hat{\tau}_{sw}(p_s) = \kappa_{SW} p_0/g \times (p_s/p_0)^2$ and $\tau_{LW} \equiv \hat{\tau}_{lw}(p_s) = \kappa_{LW} p_0/g \times (p_s/p_0)^2$. The surface temperature, T_s, is determined by energy balance

$$\mathcal{C}\frac{\mathrm{d}T_s}{\mathrm{d}t} = F_{SW}^{\downarrow}|_{p_s} - (\sigma_{SB}T_s^4 - F_{LW}^{\downarrow}|_{p_s}) - \mathcal{D}|_{p_s}.$$

Here $\mathcal{C}$ is the surface thermal inertia. For a tidally locked planet the stellar forcing does not depend on time. As a first approximation we ignore internal atmospheric variability and assume that T_s is time-independent. This means that $\mathcal{C}$ does not enter the list of dimensional quantities (see below for a discussion of when this assumption is valid).

We form the following nondimensional quantities, marked with the hat symbol: $\frac{D}{Dt} = \frac{1}{t_{wave}}\left(\frac{D}{D\hat{t}}\right)$, $\nabla = \hat{\nabla}/a$, $p = p_s\hat{p}$, $\mathbf{u} = c_{wave}\hat{\mathbf{u}}$, $\omega = c_{wave}p_s/a \times \hat{\omega}$, $\phi = gH\hat{\phi}$, $T = T_{eq}\hat{T}$, $F = \sigma_{SB}T_{eq}^4\hat{F}$, $\mathbf{F}_m = p_sC_Dc_{wave}^2/(RT_{eq}) \times \hat{\mathbf{F}}_m$, $\mathcal{D} = p_sc_pC_Dc_{wave}/R \times \hat{\mathcal{D}}$.

The primitive and radiative equations in nondimensional form are

$$\begin{aligned}
\left(\frac{D\hat{\mathbf{u}}}{D\hat{t}}\right) &= -\frac{a^2}{L_{Ro}^2}(\sin\theta\mathbf{k}\times\hat{\mathbf{u}}) - \frac{c_p}{R}\left(\hat{\nabla}\hat{\phi}\right) - \frac{C_Da}{H}\left(\frac{\partial\hat{\mathbf{F}}_m}{\partial\hat{p}}\right),\\
\left(\frac{\partial\hat{\phi}}{\partial\hat{p}}\right) &= -\left(\frac{\hat{T}}{\hat{p}}\right),\\
\left(\hat{\nabla}\cdot\hat{\mathbf{u}}\right) &+ \left(\frac{\partial\hat{\omega}}{\partial\hat{p}}\right) = 0,\\
\left(\frac{D\hat{T}}{D\hat{t}}\right) &= \frac{R}{c_p}\left(\frac{\hat{T}\hat{\omega}}{\hat{p}}\right) + \frac{t_{wave}}{t_{rad}}\left(\frac{\partial\hat{F}}{\partial\hat{p}}\right) + \frac{C_Da}{H}\left(\frac{\partial\hat{\mathcal{D}}}{\partial\hat{p}}\right),\\
\left(\frac{\partial\hat{F}_{LW}^{\uparrow}}{\partial\hat{\tau}_{lw}}\right) &= \hat{F}_{LW}^{\uparrow} - \hat{T}^4 \qquad (0 \leqslant \hat{\tau}_{lw} \leqslant \tau_{LW}),\\
\left(\frac{\partial\hat{F}_{LW}^{\downarrow}}{\partial\hat{\tau}_{lw}}\right) &= -(\hat{F}_{LW}^{\downarrow} - \hat{T}^4) \qquad (0 \leqslant \hat{\tau}_{lw} \leqslant \tau_{LW}),\\
\left(\frac{\partial\hat{F}_{SW}^{\downarrow}}{\partial\tau_{sw}}\right) &= -\hat{F}_{SW}^{\downarrow} \qquad (0 \leqslant \hat{\tau}_{sw} \leqslant \gamma\tau_{LW}).
\end{aligned}$$

The surface energy budget in nondimensional form is

$$\frac{t_{rad,s}}{t_{rad}}\left(\frac{\mathrm{d}\hat{T}_s}{\mathrm{d}\hat{t}}\right) = \hat{F}_{SW}^{\downarrow}|_{p_s} - (\hat{T}_s^4 - \hat{F}_{LW}^{\downarrow}|_{p_s}) - \frac{t_{rad}}{t_{wave}}\frac{C_Da}{H}\hat{\mathcal{D}}|_{p_s},$$

where $t_{rad,s} = \mathcal{C}/\sigma_{SB}T_{eq}^3$ is the surface radiative timescale. Our assumption that T_s is time-independent, and $t_{rad,s}$ can be ignored, therefore breaks down when $t_{rad,s} \gtrsim t_{rad}$. In our reference simulations we assume a heat capacity equivalent to that of a well-mixed water layer with depth 3 m. This means the surface thermal inertia, $\mathcal{C}$, is actually large enough that $t_{rad,s} \sim t_{rad}$. To check if this affects our results we recomputed the reference simulations in Figure 2.4 with $\mathcal{C}$ reduced by a factor of 300, such that $t_{rad,s} \ll t_{rad}$. We note that this heat capacity is far less than realistic values for $\mathcal{C}$. At individual grid points, the time-averaged surface temperature changes up to 2.5% in the cool Earth-size scenario and up to 6% for the hot super-Earth. However, reducing $\mathcal{C}$ affects the phase curve amplitude of both runs by less than 0.5%. This confirms that our choice of six nondimensional parameters captures the dominant dynamics in the GCM simulations (Fig. 2.2).

APPENDIX B

TIDALLY LOCKED COORDINATE SYSTEM

A standard geographic coordinate system is defined via the radial distance from a planet's center, r, the latitude, θ, which is the angle away from the equator, and the longitude, λ, which is the angle about the planet's north pole. Atmospheres of fast rotating planets are approximately symmetric around the axis of rotation due to conservation of angular momentum, so their time-averaged properties are often displayed as averages over λ. Here we make use of the approximate symmetry of slowly rotating tidally locked planets about the axis connecting the substellar and antistellar points (Fig. 2.1). We define the tidally locked latitude, θ_{TL}, as the angle away from the terminator, and the tidally locked longitude, λ_{TL}, as the angle about the substellar point. We choose $(\theta, \lambda) = (0, 0)$ to coincide with the substellar point, and $(\theta_{TL}, \lambda_{TL}) = (0, 0)$ to coincide with the north pole (see top row in Fig. 2.1). For example, in tidally locked coordinates $\lambda_{TL} = 0$ and $90^\circ \geqslant \theta_{TL} \geqslant -90^\circ$ defines the arc that connects substellar and antistellar points via the north pole.

To translate between standard and tidally locked coordinates we first transform both spherical coordinate systems into Cartesian coordinates, so that the north pole lies at $(x, y, z) = (0, 0, r)$ and the substellar point lies at $(x, y, z) = (r, 0, 0)$

$$\begin{aligned} x &= r\cos\theta\cos\lambda, \\ y &= r\cos\theta\sin\lambda, \\ z &= r\sin\theta, \end{aligned} \tag{B.1}$$

and

$$\begin{aligned} x &= r\sin\theta_{TL}, \\ y &= r\cos\theta_{TL}\sin\lambda_{TL}, \\ z &= r\cos\theta_{TL}\cos\lambda_{TL}. \end{aligned} \tag{B.2}$$

By combining equations B.1 and B.2 we can express θ_{TL} and λ_{TL} in terms of θ and λ:

$$\begin{aligned} \theta_{TL} &= \sin^{-1}(\cos\theta\cos\lambda), \\ \lambda_{TL} &= \tan^{-1}\left(\frac{\sin\lambda}{\tan\theta}\right). \end{aligned} \tag{B.3}$$

To plot GCM output in tidally locked coordinates we first express the GCM output in terms of θ_{TL} and λ_{TL}, and then linearly interpolate the output onto an evenly-spaced $(\theta_{TL}, \lambda_{TL})$ grid.

Transforming GCM wind velocities into tidally locked coordinates is slightly more complicated. Horizontal winds are defined as $(u, v) \equiv \left(r\cos\theta\frac{\mathrm{D}\lambda}{\mathrm{D}t}, r\frac{\mathrm{D}\theta}{\mathrm{D}t}\right)$. We analogously define wind velocities in a tidally locked coordinate system as

$$\begin{aligned} u_{TL} &\equiv r\cos\theta_{TL}\frac{\mathrm{D}\lambda_{TL}}{\mathrm{D}t} \\ &= r\cos\theta_{TL}\left(\frac{\partial\lambda_{TL}}{\partial\lambda}\frac{\mathrm{D}\lambda}{\mathrm{D}t} + \frac{\partial\lambda_{TL}}{\partial\theta}\frac{\mathrm{D}\theta}{\mathrm{D}t}\right) \\ &= \cos\theta_{TL}\left(\frac{\partial\lambda_{TL}}{\partial\lambda}\frac{u}{\cos\theta} + \frac{\partial\lambda_{TL}}{\partial\theta}v\right), \end{aligned}$$

and

$$\begin{aligned} v_{TL} &\equiv r\frac{\mathrm{D}\theta_{TL}}{\mathrm{D}t} \\ &= r\left(\frac{\partial\theta_{TL}}{\partial\lambda}\frac{\mathrm{D}\lambda}{\mathrm{D}t} + \frac{\partial\theta_{TL}}{\partial\theta}\frac{\mathrm{D}\theta}{\mathrm{D}t}\right) \\ &= \frac{\partial\theta_{TL}}{\partial\lambda}\frac{u}{\cos\theta} + \frac{\partial\theta_{TL}}{\partial\theta}v. \end{aligned}$$

We evaluate the partial derivatives $(\partial\lambda_{TL}/\partial\lambda, \partial\lambda_{TL}/\partial\theta, \partial\theta_{TL}/\partial\lambda, \partial\theta_{TL}/\partial\theta)$ using equations B.3. The resulting expressions are long and lead to little insight, so we omit them here.

APPENDIX C

COMPUTING PHASE CURVES

The area-averaged and observer-projected flux from a planet as seen by a distant observer is

$$F(\xi) = \frac{\int_{-\pi/2}^{\pi/2} \int_{-\xi-\pi/2}^{-\xi+\pi/2} F_{LW}^{\uparrow}|_{p=0} \cos(\lambda+\xi)\cos^2(\theta) d\lambda d\theta}{\int_{-\pi/2}^{\pi/2} \int_{-\xi-\pi/2}^{-\xi+\pi/2} \cos(\lambda+\xi)\cos^2(\theta) d\lambda d\theta},$$

where ξ is the phase angle, i.e., the angle between the observer's line-of-sight and the substellar point ($\xi = 0$ at secondary eclipse, $\xi = \pi$ at transit), and $F_{LW}^{\uparrow}|_{p=0}$ is the outgoing thermal flux at the top-of-atmosphere. This equation is expressed in standard latitude-longitude coordinates, and assumes that the orbit is viewed edge-on (Cowan & Agol, 2008). The planet's total flux as seen by a distant observer is $\pi a^2 \times F(\xi)$.

The maximum thermal flux emitted by a planet corresponds to the flux emitted by the dayside of a bare rock, which we call F_{rock}. We compute F_{rock} by setting the outgoing thermal flux equal to the incoming stellar flux at every point, $F_{LW}^{\uparrow}|_{p=0} = L_*(1-\alpha)\cos(\theta)\cos(\lambda)$, so $F_{rock} = 2/3 \times L_*(1-\alpha)$. We define the dayside-averaged observer-projected temperature of a bare rock as $\sigma_{SB} T_{rock}^4 = F_{rock}$. This temperature is related to the equilibrium temperature of a planet with effective heat transport via $T_{rock} = (8/3)^{1/4} T_{eq}$.

APPENDIX D

FINDING ALL DIMENSIONAL TRANSFORMATIONS THAT ONLY AFFECT ONE NONDIMENSIONAL PARAMETER

We illustrate how to find the set of all transformations on the dimensional parameters that only vary one nondimensional parameter. Our approach is similar to the commonly-used technique in dimensional analysis of finding a complete set of nondimensional parameters via matrix methods (Price, 2003). The method is general, but we illustrate it assuming (a, Ω, T_{eq}) are fixed to directly explain our parameter choices in Table 2.1b. To transform the remaining dimensional parameters, we consider multiplying each of them by a different constant,

$$\begin{aligned}(R', c_p', g', p_s', \kappa_{SW}', \kappa_{LW}', C_D') = \\ (C^{v_1}R, C^{v_2}c_p, C^{v_3}g, C^{v_4}p_s, C^{v_5}\kappa_{SW}, C^{v_6}\kappa_{LW}, C^{v_7}C_D),\end{aligned}$$

where a prime denotes a transformed parameter, C is a constant, and $(v_1, v_2, ...)$ are different exponents. At the same time we want to keep all nondimensional parameters except one fixed. As an example we consider all transformations that multiply R/c_p by a factor of C. This means

$$\begin{aligned}
\left(\frac{R}{c_p}\right)' = C \times \left(\frac{R}{c_p}\right) \quad &\Rightarrow \quad C^{v_1}C^{-v_2}\left(\frac{R}{c_p}\right) = C\left(\frac{R}{c_p}\right) \\
&\Rightarrow \quad C^{v_1-v_2} = C^1 \\
\left(\frac{a^2}{L_{Ro}^2}\right)' = C \times \left(\frac{a^2}{L_{Ro}^2}\right) \quad &\Rightarrow \quad C^{-v_1+v_2/2}\left(\frac{a^2}{L_{Ro}^2}\right) = C^0\left(\frac{a^2}{L_{Ro}^2}\right) \\
&\Rightarrow \quad C^{-v_1+v_2/2} = C^0 \\
\left(\frac{t_{wave}}{t_{rad}}\right)' = C \times \left(\frac{t_{wave}}{t_{rad}}\right) \quad &\Rightarrow \quad C^{-v_1-v_2/2+v_3-v_4}\left(\frac{t_{wave}}{t_{rad}}\right) = C^0\left(\frac{t_{wave}}{t_{rad}}\right) \\
&\Rightarrow \quad C^{-v_1-v_2/2+v_3-v_4} = C^0 \\
&\quad\vdots
\end{aligned}$$

We consider the exponents of C in the resulting equations. They form a linear system of equations and can be written in matrix form $A\mathbf{v} = (1, 0, 0, ...)$ as

$$\begin{pmatrix} 1 & -1 & 0 & 0 & 0 & 0 & 0 \\ -1 & 1/2 & 0 & 0 & 0 & 0 & 0 \\ -1 & -1/2 & 1 & -1 & 0 & 0 & 0 \\ 0 & 0 & 0 & 0 & 1 & -1 & 0 \\ 0 & 0 & -1 & 2 & 0 & 1 & 0 \\ -1 & 0 & 1 & 0 & 0 & 0 & 1 \end{pmatrix} \begin{pmatrix} v_1 \\ v_2 \\ v_3 \\ v_4 \\ v_5 \\ v_6 \\ v_7 \end{pmatrix} = \begin{pmatrix} 1 \\ 0 \\ 0 \\ 0 \\ 0 \\ 0 \end{pmatrix}$$

The matrix columns correspond to the exponents of $(R, c_p, g, p_s, \kappa_{SW}, \kappa_{LW}, C_D)$, and the matrix rows correspond to each nondimensional parameter. For example, the first row of the matrix corresponds to R/c_p, and has only two non-zero entries (corresponding to the exponents with which R and c_p appear in R/c_p).

This system of equations is underdetermined, that is, it has infinitely many solutions (there are 6 rows/6 equations, but 7 columns/7 unknowns). All solutions can be expressed as a particular solution $\mathbf{v}$ to the equation $A\mathbf{v} = (1, 0, 0, ...)$, plus any vector that lies in the kernel (nullspace) of A: $\{\mathbf{v} + \mathbf{x},\ \text{where } \mathbf{x} \text{ satisfies } A\mathbf{x} = \mathbf{0}\}$. We express the set of all solutions as

$$\{\mathbf{v} + k \cdot \mathbf{x}\} \quad = \quad (-1, -2, -1-k, 1-k, -3+k, -3+k, k)\,,$$

where k is an arbitrary number, and each entry of this vector corresponds to the power to which C is being raised for each dimensional parameter. For example, to increase R/c_p by C, the first dimensional parameter, R, is multiplied by C^{-1}, the second dimensional parameter, c_p, is multiplied by C^{-2} etc.

To vary R/c_p over the largest possible range compatible with the dimensional constraints in Table 2.2 amounts to finding the largest and smallest values of C that are still consistent with Table 2.2, while k is allowed to take on any value. We first solve this problem by inspection, and then compare our parameter choices to the values we get from numerical optimization. For our reference case of a cool, Earth-sized planet we find $k = 0$ and $1/\sqrt{1.5} \lesssim C \leqslant 1$ (Table 2.1b).

We note that one can use this method similarly to find the set of all transformations that leave all nondimensional parameters invariant (see Table 2.1a, Fig. 2.2). This set of transformations is simply given by the kernel of A.

APPENDIX E

DRAG TIMESCALE

We start with the nondimensional parameters that we derived in Koll & Abbot (2015):

$$\left(\frac{R}{c_p}, \frac{a^2}{L_{Ro}^2}, \frac{t_{wave}}{t_{rad}}, \tau_{SW}, \tau_{LW}, \frac{C_D a}{H}\right). \tag{E.1}$$

Theoretical work on the atmospheric dynamics of hot Jupiters uses similar wave and radiative timescales (e.g., Perez-Becker & Showman, 2013), but additionally introduces a drag timescale. This is because the drag mechanisms on hot Jupiters are still not well-constrained, and friction is often parametrized as Rayleigh friction with a unknown damping timescale. To facilitate comparison of our work with the hot Jupiter literature and to examine the importance of drag in the atmospheres of rocky planets, we rewrite the last of our six nondimensional parameters as a ratio of wave over drag timescales.

Models of terrestrial atmospheres (including FMS) often parametrize boundary layer friction as vertical momentum diffusion with a source term that is quadratic in wind speed. The horizontal momentum equation takes the form

$$\frac{\mathrm{D}\mathbf{u}}{\mathrm{D}t} = \cdots + g\frac{\partial \mathcal{D}_m}{\partial p}, \tag{E.2}$$

where $\mathbf{u}$ is the horizontal wind speed, $\mathcal{D}_m$ is the diffusive momentum flux due to surface drag, and the source term is $\mathcal{D}_m\left(p_s\right) = C_D \rho_s |\mathbf{u}_s| \mathbf{u}_s$. We take a vertical average across the boundary layer to find the average acceleration due to drag:

$$\begin{aligned}
\frac{1}{p_s - p_{BL}} \int_{p_{BL}}^{p_s} \frac{\mathrm{D}\mathbf{u}}{\mathrm{D}t} dp &= \cdots + \frac{g}{p_s - p_{BL}} \int_{p_{BL}}^{p_s} \frac{\partial \mathcal{D}_m}{\partial p} dp \\
\overline{\frac{\mathrm{D}\mathbf{u}}{\mathrm{D}t}} &= \cdots + \frac{g}{p_s - p_{BL}} \times \left[\mathcal{D}_m\left(p_s\right) - \mathcal{D}_m\left(p_{BL}\right)\right] \\
\overline{\frac{\mathrm{D}\mathbf{u}}{\mathrm{D}t}} &= \cdots + \frac{g\mathcal{D}_m\left(p_s\right)}{p_s - p_{BL}} \\
\overline{\frac{\mathrm{D}\mathbf{u}}{\mathrm{D}t}} &= \cdots + \frac{gC_D\rho_s|\mathbf{u}_s|\mathbf{u}_s}{p_s - p_{BL}} \qquad \text{(E.3)}
\end{aligned}$$

Here p_{BL} denotes the top pressure level of the boundary layer and we used the fact that drag has to disappear at the upper edge of the boundary layer, $\mathcal{D}_m\left(p_{BL}\right) = 0$. We then scale this equation for fast atmospheric motions $\mathbf{u} \sim c_{wave}$,

$$\begin{aligned}
\frac{c_{wave}}{t_{drag}} &\sim \frac{gC_D\rho_s c_{wave}^2}{p_s} \\
\frac{c_{wave}}{t_{drag}} &\sim \frac{aC_D g}{RT_s}\frac{c_{wave}}{a} c_{wave} \\
\frac{c_{wave}}{t_{drag}} &\sim \frac{C_D a}{H}\frac{1}{t_{wave}} c_{wave}, \qquad \text{(E.4)}
\end{aligned}$$

where we have assumed that the boundary layer is thick, $p_{BL} \ll p_s$ (see Fig. 3.1), used the ideal gas law in the second step, $\rho_s = p_s R^{-1} T_s^{-1}$, and used the wave timescale $t_{wave} = a/c_{wave}$ in the last step. This lets us derive a drag timescale

$$t_{drag} \sim \frac{H}{C_D a} t_{wave}. \qquad \text{(E.5)}$$

Note, in contrast to Rayleigh drag schemes where the drag timescale is independent of **u**, here the drag timescale scales with **u** and thus with the dynamical timescale t_{wave}. Using this drag timescale we can rewrite the last nondimensional parameter as $C_D a/H \sim t_{wave}/t_{drag}$

and find an alternative set of six governing parameters:

$$\left(\frac{R}{c_p}, \frac{a^2}{L_{Ro}^2}, \frac{t_{wave}}{t_{rad}}, \tau_{SW}, \tau_{LW}, \frac{t_{wave}}{t_{drag}}\right). \tag{E.6}$$

In most cases $C_D a/H$ is of order unity so the drag timescale is generally comparable to the dynamical timescale. For example, assuming a planet of Earth's size, $(a, g) = (a_\oplus, g_\oplus)$, a high MMW atmosphere, $R = R_{N_2}$, a relatively cool temperature, $T_{eq} = 300K$, and a standard value for the drag coefficient, $C_D = 10^{-3}$, we find $t_{drag} = 1.4 t_{wave}$. Variations in the planetary radius a or in the drag coefficient C_D do not affect this result much. For example, for a neutrally buoyant boundary layer $C_D = [k_{vk}/\log(z/z_0)]^2$, where k_{kv} is the von Karman constant, z is the height above the surface and z_0 is the surface roughness length. Because C_D only depends logarithmically on z_0, the drag timescale is not very sensitive to the surface properties. This means we expect friction to generally be an important process inside the boundary layer of rocky planets.

The most important exception is a hot H_2 atmosphere, through its effect on the scale height H. For example, repeating the above calculation with a hot H_2-dominated atmosphere, $R = R_{H_2}$ and $T_{eq} = 600$ K, we find $t_{drag} = 40 t_{wave}$. This means surface friction is far less effective in H_2 atmospheres than in high MMW atmospheres.

APPENDIX F

WIND SPEED SCALING FROM WORDSWORTH (2015)

To compare the results of Wordsworth (2015) with our GCM simulations we write Wordsworth's Equation 33 as

$$U_0 = 4\sigma T_{eq}^4 \frac{\tau_{LW}}{2\zeta p_s C_D} \frac{R}{c_p}, \tag{F.1}$$

where $\zeta \equiv 1/3$. The above equation reduces to Wordsworth's Equation 33 by plugging in his Equation 12, i.e., by assuming a specific form for τ. We leave the equation in this general form. We identify Wordsworth's absorbed stellar flux $(1-A)F$ as $4\sigma T_{eq}^4$.

The nondimensional equations in Wordsworth (2015) are not affected. To find the surface wind speed we solve his Equations 44 and 45 numerically to find $\tilde{T}$ and $\tilde{U}$. We then convert the nondimensional $\tilde{U}$ into a dimensional quantity using the above scale U_0, i.e., $|\mathbf{u}| = U_0\tilde{U}$.

APPENDIX G

NUMERICAL SOLUTION FOR THE RCS MODEL

The boundary conditions of the radiative-convective-subsiding (RCS) model are specified at two different points, the tropopause and the surface. Instead of matching both boundaries simultaneously we first guess a value of the nightside OLR, $F(\tau_0)$. Given a value of $F(\tau_0)$, we can solve for all variables (T_d, τ_0, $T(\tau)$, and $F(\tau)$). Our guess will in general not satisfy the nightside surface energy budget (Equation 3.21c), so we iterate until $F(\tau_{LW}) = 0$ is satisfied. To iterate we use a bisection method, where the nightside OLR is bounded by $0 \leqslant F(\tau_0) \leqslant \sigma T_{eq}^4$ (the limits correspond to a planet with zero and perfect day-night heat redistribution).

We proceed as follows. Given a value of $F(\tau_0)$, Equations 3.25 and 3.22 can be rewritten as an implicit equation for τ_0,

$$2 + \frac{\tau_0}{2} = \left(\frac{1+\tau_0}{2}\right)\left(\frac{\tau_{LW}}{\tau_0}\right)^{4\beta}\left[e^{-(\tau_{LW}-\tau_0)} + \int_{\tau_0}^{\tau_{LW}}\left(\frac{\tau'}{\tau_{LW}}\right)^{4\beta} e^{-(\tau'-\tau_0)} d\tau'\right] + \frac{F(\tau_0)}{\sigma T_{eq}^4} \tag{G.1}$$

We solve for τ_0 using, again, a bisection method, where we note that $0 < \tau_0 < \tau_{LW}$. We then use Equations 3.20 and 3.22 to find $T(\tau_0)$ and T_d:

$$T(\tau_0) = T_{eq}\left(\frac{1+\tau_0}{2}\right)^{1/4} \tag{G.2}$$

$$T_d = T_{eq}\left(\frac{1+\tau_0}{2}\right)^{1/4}\left(\frac{\tau_{LW}}{\tau_0}\right)^{\beta}. \tag{G.3}$$

Once we know T_d we can find $\bar{\omega}$ (Equations 3.12 and 3.26). We then have three boundary conditions that are specified at the upper boundary, the guessed $F(\tau_0)$, $dF(\tau_0)/d\tau = 0$, and $T(\tau_0)$. We use SciPy's VODE solver to integrate the WTG and Schwarzschild equations (Equations 3.19) down to the nightside surface, which gives us the net surface flux $F(\tau_{LW})$. We iterate until we satisfy the nightside surface budget, $F(\tau_{LW}) = 0$. After having solved for $T(\tau)$ we find the nightside surface temperature T_n using the nightside surface energy budget (cf. Robinson & Catling, 2012),

$$
\begin{aligned}
\sigma T_n^4 &= F^-(\tau_{LW}) \\
&= \sigma T_{eq}^4 \frac{\tau_0}{2} e^{-(\tau_{LW}-\tau_0)} + \int_{\tau_0}^{\tau_{LW}} \sigma T(\tau')^4 e^{-(\tau'-\tau_0)} d\tau'. \qquad \text{(G.4)}
\end{aligned}
$$

REFERENCES

Abbot, D. S., & Halevy, I. 2010, Journal of Climate, 23, 4121

Abbot, D. S., & Pierrehumbert, R. T. 2010, Journal of Geophysical Research, 115, doi:10.1029/2009JD012007

Abe, Y., Abe-Ouchi, A., Sleep, N. H., & Zahnle, K. J. 2011, Astrobiology, 11, 443

Barnes, R., Deitrick, R., Luger, R., et al. 2016, arXiv:1608.06919 [astro-ph], arXiv:1608.06919

Batalha, N., Kalirai, J., Lunine, J., Clampin, M., & Lindler, D. 2015, arXiv:1507.02655 [astro-ph], arXiv:1507.02655

Beichman, C., Benneke, B., Knutson, H., et al. 2014, Publications of the Astronomical Society of the Pacific, 126, 1134

Belu, A. R., Selsis, F., Morales, J.-C., et al. 2011, Astronomy & Astrophysics, 525, A83

Benneke, B., & Seager, S. 2012, The Astrophysical Journal, 753, 100

Berta-Thompson, Z. K., Irwin, J., Charbonneau, D., et al. 2015, Nature, 527, 204

Bétrémieux, Y., & Kaltenegger, L. 2014, The Astrophysical Journal, 791, 7

Biagio, C. D., di Sarra, A., Eriksen, P., et al. 2012, Climate Dynamics, 39, 953

Bister, M., & Emanuel, K. A. 1998, Meteorology and Atmospheric Physics, 65, 233

Buckingham, E. 1914, Physical Review, 4, 345

Burke, C. J., Christiansen, J. L., Mullally, F., et al. 2015, arXiv:1506.04175 [astro-ph], arXiv:1506.04175

Burrows, A., Rauscher, E., Spiegel, D. S., & Menou, K. 2010, The Astrophysical Journal, 719, 341

Burrows, A. S. 2014, Proceedings of the National Academy of Sciences, 111, 12601

Caballero, R. 2014, Physics of the Atmosphere (Bristol: IOP Publishing)

Carnot, S. 1824, Réflexions Sur La Puissance Motrice Du Feu et Sur Les Machines Propres À Développer Cette Puissance (Paris: Bachelier), (1890 English translation by Robert Thurston)

Chai, J., Jansen, M., & Vallis, G. K. 2016, Journal of the Atmospheric Sciences, 73, 3249

Charnay, B., Meadows, V., Misra, A., Leconte, J., & Arney, G. 2015, The Astrophysical Journal Letters, 813, L1

Cowan, N. B., & Agol, E. 2008, The Astrophysical Journal, 678, L129

—. 2011, The Astrophysical Journal, 726, 82

Cowan, N. B., Machalek, P., Croll, B., et al. 2012, The Astrophysical Journal, 747, 82

Cowan, N. B., Greene, T., Angerhausen, D., et al. 2015, Publications of the Astronomical Society of the Pacific, 127, 311

Cunha, D., Correia, A. C., & Laskar, J. 2014, International Journal of Astrobiology, FirstView, 1

Dalcanton, J., Seager, S., Aigrain, S., et al. 2015, arXiv:1507.04779 [astro-ph], arXiv:1507.04779

de Wit, J., & Seager, S. 2013, Science, 342, 1473

Del Genio, A. D. 2013, in Comparative Climatology of Terrestrial Planets, ed. S. J. Mackwell, A. A. Simon-Miller, J. W. Harder, & M. A. Bullock, Space Science Series (University of Arizona Press), 3–18

Del Genio, A. D., & Suozzo, R. J. 1987, Journal of the Atmospheric Sciences, 44, 973

Deming, D., & Seager, S. 2009, Nature, 462, 301

Deming, D., Seager, S., Winn, J., et al. 2009, Publications of the Astronomical Society of the Pacific, 121, 952

Dressing, C. D., & Charbonneau, D. 2013, The Astrophysical Journal, 767, 95

—. 2015, The Astrophysical Journal, 807, 45

Emanuel, K. A. 1986, Journal of the Atmospheric Sciences, 43, 585

—. 1988, Journal of the Atmospheric Sciences, 45, 1143

Emanuel, K. A., & Bister, M. 1996, Journal of the Atmospheric Sciences, 53, 3276

Emanuel, K. A., David Neelin, J., & Bretherton, C. S. 1994, Quarterly Journal of the Royal Meteorological Society, 120, 1111

Emanuel, K. A., & Rotunno, R. 1989, Tellus A, 41, doi:10.3402/tellusa.v41i1.11817

Farrell, B. F. 1990, Journal of the Atmospheric Sciences, 47, 2986

Fortney, J. J. 2005, Monthly Notices of the Royal Astronomical Society, 364, 649

Fraedrich, K., & Lunkeit, F. 2008, Tellus A, 60, 921

Frierson, D. 2005, Ph.d. thesis, Princeton University

Frierson, D. M. W. 2007, Journal of the Atmospheric Sciences, 64, 1959

Frierson, D. M. W., Held, I. M., & Zurita-Gotor, P. 2006, Journal of the Atmospheric Sciences, 63, 2548

Fromang, S., Leconte, J., & Heng, K. 2016, Astronomy & Astrophysics, doi:10.1051/0004-6361/201527600

Fujii, Y., Kimura, J., Dohm, J., & Ohtake, M. 2014, Astrobiology, 14, 753

Glasse, A. C. H., Bauwens, E., Bouwman, J., et al. 2010, in Proc. SPIE 7731, ed. J. M. Oschmann, Jr., M. C. Clampin, & H. A. MacEwen, 77310K

Golitsyn, G. 1970, Icarus, 13, 1

Goodman, J. 2009, The Astrophysical Journal, 693, 1645

Goody, R. 2000, Quarterly Journal of the Royal Meteorological Society, 126, 1953, wOS:000088571500019

Griffith, C. A. 2014, Philosophical Transactions of the Royal Society A: Mathematical, Physical and Engineering Sciences, 372, 20130086

Guillot, T. 2010, Astronomy and Astrophysics, 520, A27

Hansen, C. J., Schwartz, J. C., & Cowan, N. B. 2014, Monthly Notices of the Royal Astronomical Society, 444, 3632

Harrington, J., Hansen, B. M., Luszcz, S. H., et al. 2006, Science, 314, 623

Held, I. M., & Hou, A. Y. 1980, Journal of the Atmospheric Sciences, 37, 515

Held, I. M., & Suarez, M. J. 1994, Bulletin of the American Meteorological Society, 75, 1825

Heng, K., Frierson, D. M. W., & Phillipps, P. J. 2011a, Monthly Notices of the Royal Astronomical Society, 418, 2669

Heng, K., & Kopparla, P. 2012, The Astrophysical Journal, 754, 60

Heng, K., Mendonça, J. M., & Lee, J.-M. 2014, The Astrophysical Journal Supplement Series, 215, 4

Heng, K., Menou, K., & Phillipps, P. J. 2011b, Monthly Notices of the Royal Astronomical Society, 413, 2380

Hoffman, P. F., Kaufman, A. J., Halverson, G. P., & Schrag, D. P. 1998, Science, 281, 1342

Hu, R., Kass, D. M., Ehlmann, B. L., & Yung, Y. L. 2015, Nature Communications, 6, 10003

Ingersoll, A. P. 1969, Journal of the Atmospheric Sciences, 26, 1191

Jansen, M., & Ferrari, R. 2013, Journal of the Atmospheric Sciences, 70, 2948

Joshi, M., Haberle, R., & Reynolds, R. 1997, Icarus, 129, 450

Kaltenegger, L., & Traub, W. A. 2009, The Astrophysical Journal, 698, 519

Kaspi, Y., & Showman, A. P. 2015, The Astrophysical Journal, 804, 60

Kasting, J. F. 1988, Icarus, 74, 472

Kasting, J. F., Whitmire, D. P., & Reynolds, R. T. 1993, Icarus, 101, 108

Kataria, T., Showman, A. P., Fortney, J. J., Marley, M. S., & Freedman, R. S. 2014, The Astrophysical Journal, 785, 92

Kataria, T., Showman, A. P., Lewis, N. K., et al. 2013, The Astrophysical Journal, 767, 76

Kleidon, A., Fraedrich, K., Kunz, T., & Lunkeit, F. 2003, Geophysical Research Letters, 30, doi:10.1029/2003GL018363, wOS:000187489700004

Knutson, H. A., Benneke, B., Deming, D., & Homeier, D. 2014, Nature, 505, 66

Knutson, H. A., Charbonneau, D., Allen, L. E., et al. 2007, Nature, 447, 183

Knutson, H. A., Lewis, N., Fortney, J. J., et al. 2012, The Astrophysical Journal, 754, 22

Koll, D. D. B., & Abbot, D. S. 2015, The Astrophysical Journal, 802, 21

—. 2016, The Astrophysical Journal, 825, 99

Komacek, T. D., & Showman, A. P. 2016, The Astrophysical Journal, 821, 16

Kopparapu, R. K., Wolf, E. T., Haqq-Misra, J., et al. 2016, The Astrophysical Journal, 819, 84

Kreidberg, L., & Loeb, A. 2016, arXiv:1608.07345 [astro-ph], arXiv:1608.07345

Kreidberg, L., Bean, J. L., Désert, J.-M., et al. 2014, Nature, 505, 69

Kreidberg, L., Line, M. R., Bean, J. L., et al. 2015, arXiv:1504.05586 [astro-ph], arXiv:1504.05586

Laliberté, F., Zika, J., Mudryk, L., et al. 2015, Science, 347, 540

Lecavelier des Etangs, A., Pont, F., Vidal-Madjar, A., & Sing, D. 2008, Astronomy and Astrophysics, 481, L83

Leconte, J., Forget, F., Charnay, B., Wordsworth, R., & Pottier, A. 2013, Nature, 504, 268

Leconte, J., Wu, H., Menou, K., & Murray, N. 2015, Science, 347, 632

Lee, J.-M., Fletcher, L. N., & Irwin, P. G. J. 2012, Monthly Notices of the Royal Astronomical Society, 420, 170

Li, J., & Goodman, J. 2010, The Astrophysical Journal, 725, 1146

Line, M. R., & Parmentier, V. 2016, The Astrophysical Journal, 820, 78

Line, M. R., Zhang, X., Vasisht, G., et al. 2012, The Astrophysical Journal, 749, 93

Liu, J., & Schneider, T. 2011, Journal of the Atmospheric Sciences, 68, 2742

Lorenz, E. N. 1955, Tellus, 7, 157

Madhusudhan, N., & Seager, S. 2009, The Astrophysical Journal, 707, 24

Makarov, V. V., Berghea, C., & Efroimsky, M. 2012, The Astrophysical Journal, 761, 83

Manabe, S., Smagorinsky, J., & Strickler, R. F. 1965, Monthly Weather Review, 93, 769

Matsuno, T. 1966, Journal of the Meteorological Society of Japan. Ser. II, 44, 25

Menou, K. 2012a, The Astrophysical Journal Letters, 744, L16

—. 2012b, The Astrophysical Journal, 745, 138

—. 2013, The Astrophysical Journal, 774, 51

Merlis, T. M., & Schneider, T. 2010, Journal of Advances in Modeling Earth Systems, 2, doi:10.3894/JAMES.2010.2.13

Mills, S. M., & Abbot, D. S. 2013, The Astrophysical Journal Letters, 774, L17

Misra, A., Meadows, V., & Crisp, D. 2014, The Astrophysical Journal, 792, 61

Misra, A. K., & Meadows, V. S. 2014, The Astrophysical Journal Letters, 795, L14

Mitchell, J. L., Pierrehumbert, R. T., Frierson, D. M., & Caballero, R. 2009, Icarus, 203, 250

Mitchell, J. L., & Vallis, G. K. 2010, Journal of Geophysical Research, 115, E12008

Mitchell, J. L., Vallis, G. K., & Potter, S. F. 2014, The Astrophysical Journal, 787, 23

Morbidelli, A., Chambers, J., Lunine, J. I., et al. 2000, Meteoritics & Planetary Science, 35, 1309

Morton, T. D., & Swift, J. 2014, The Astrophysical Journal, 791, 10

Motalebi, F., Udry, S., Gillon, M., et al. 2015, Astronomy & Astrophysics, 584, A72

O'Gorman, P. A. 2010, Journal of the Atmospheric Sciences, 68, 75

O'Gorman, P. A., & Schneider, T. 2008, Journal of Climate, 21, 3815

Owen, J. E., & Mohanty, S. 2016, Monthly Notices of the Royal Astronomical Society, stw959

Parmentier, V., Showman, A. P., & Lian, Y. 2013, Astronomy & Astrophysics, 558, A91

Pascale, S., Gregory, J. M., Ambaum, M., & Tailleux, R. 2011, Climate Dynamics, 36, 1189

Pascale, S., Gregory, J. M., Ambaum, M. H. P., Tailleux, R., & Lucarini, V. 2012, Earth Syst. Dynam., 3, 19

Pauluis, O. 2010, Journal of the Atmospheric Sciences, 68, 91

Pauluis, O., Balaji, V., & Held, I. M. 2000, Journal of the Atmospheric Sciences, 57, 989

Pauluis, O., & Dias, J. 2012, Science, 335, 953

Pauluis, O., & Held, I. M. 2002, Journal of the Atmospheric Sciences, 59, 125

Pavlov, A. A., Brown, L. L., & Kasting, J. F. 2001, Journal of Geophysical Research: Planets, 106, 23267

Peixoto, J. P., & Oort, A. H. 1984, Reviews of Modern Physics, 56, 365

—. 1992, Physics of Climate, 1992nd edn. (New York: American Institute of Physics)

Peixoto, J. P., Oort, A. H., De Almeida, M., & Tomé, A. 1991, Journal of Geophysical Research: Atmospheres, 96, 10981

Perez-Becker, D., & Showman, A. P. 2013, The Astrophysical Journal, 776, 134

Pierrehumbert, R., Abbot, D., Voigt, A., & Koll, D. 2011, Annual Review of Earth and Planetary Sciences, 39, 417

Pierrehumbert, R. T. 2011a, The Astrophysical Journal, 726, L8

—. 2011b, Principles of Planetary Climate (Cambridge University Press)

Potter, S. F., Vallis, G. K., & Mitchell, J. L. 2013, Journal of the Atmospheric Sciences, 71, 596

Price, J. F. 2003, American Journal of Physics, 71, 437

Rauscher, E., & Menou, K. 2012, The Astrophysical Journal, 750, 96

Raymond, S. N., Quinn, T., & Lunine, J. I. 2004, Icarus, 168, 1

Read, P. 2011, Planetary and Space Science, 59, 900

Renno, N. O., & Ingersoll, A. P. 1996, Journal of the Atmospheric Sciences, 53, 572

Ribas, I., Bolmont, E., Selsis, F., et al. 2016, arXiv:1608.06813 [astro-ph], arXiv:1608.06813

Robinson, T. D., & Catling, D. C. 2012, The Astrophysical Journal, 757, 104

—. 2014, Nature Geoscience, 7, 12

Romps, D. M. 2008, Journal of the Atmospheric Sciences, 65, 3779

Schneider, T., & O'Gorman, P. A. 2008, Journal of the Atmospheric Sciences, 65, 3571

Schneider, T., Smith, K. L., O'Gorman, P. A., & Walker, C. C. 2006, Journal of Climate, 19, 5918

Schneider, T., & Walker, C. C. 2006, Journal of the Atmospheric Sciences, 63, 1569

Seager, S., & Deming, D. 2009, The Astrophysical Journal, 703, 1884

Seager, S., Kuchner, M., Hier-Majumder, C. A., & Militzer, B. 2007, The Astrophysical Journal, 669, 1279

Selsis, F., Wordsworth, R. D., & Forget, F. 2011, Astronomy and Astrophysics, 532, 1

Showman, A. P., Cho, J. Y.-K., & Menou, K. 2010, in Exoplanets, ed. S. Seager (University of Arizona Press), 471–516

Showman, A. P., & Guillot, T. 2002, Astronomy and Astrophysics, 385, 166

Showman, A. P., Lewis, N. K., & Fortney, J. J. 2015, The Astrophysical Journal, 801, 95

Showman, A. P., & Polvani, L. M. 2011, Astrophysical Journal, 738, doi:10.1088/0004-637X/738/1/71

Showman, A. P., Wordsworth, R. D., Merlis, T. M., & Kaspi, Y. 2013, in Comparative Climatology of Terrestrial Planets, ed. S. J. Mackwell, A. A. Simon-Miller, J. W. Harder, & M. A. Bullock, Space Science Series (University of Arizona Press), 277–326

Singh, M. S., & O'Gorman, P. A. 2016, Journal of Advances in Modeling Earth Systems, n/a

Snellen, I. A. G., de Kok, R. J., de Mooij, E. J. W., & Albrecht, S. 2010, Nature, 465, 1049

Sobel, A. H., Nilsson, J., & Polvani, L. M. 2001, Journal of the Atmospheric Sciences, 58, 3650

Stevenson, K. B., Désert, J.-M., Line, M. R., et al. 2014, Science, 346, 838

Tinetti, G., Beaulieu, J. P., Henning, T., et al. 2012, Experimental Astronomy, 34, 311

Vallis, G. K. 2006, Atmospheric and Oceanic Fluid Dynamics (Cambridge, U.K.: Cambridge University Press)

Voigt, A. 2013, Earth Syst. Dynam., 4, 425

Voigt, A., & Abbot, D. S. 2012, Clim. Past, 8, 2079

Voigt, A., Held, I. M., & Marotzke, J. 2012, Journal of the Atmospheric Sciences, 69, 116

von Paris, P., Hedelt, P., Selsis, F., Schreier, F., & Trautmann, T. 2013, Astronomy & Astrophysics, 551, A120

Wordsworth, R. 2015, The Astrophysical Journal, 806, 180

Wordsworth, R. D. 2016, Earth and Planetary Science Letters, 447, 103

Wordsworth, R. D., & Pierrehumbert, R. T. 2013, The Astrophysical Journal, 778, 154

Yang, J., & Abbot, D. S. 2014, The Astrophysical Journal, 784, 155

Yang, J., Boué, G., Fabrycky, D. C., & Abbot, D. S. 2014, The Astrophysical Journal Letters, 787, L2

Yang, J., Cowan, N. B., & Abbot, D. S. 2013, The Astrophysical Journal Letters, 771, L45

Zalucha, A. M., Michaels, T. I., & Madhusudhan, N. 2013, Icarus, 226, 1743